LASER INTERFEROMETER GRAVITATIONAL WAVE OBSERVATORY
- LIGO -
CALIFORNIA INSTITUTE OF TECHNOLOGY
MASSACHUSETTS INSTITUTE OF TECHNOLOGY

Subsystem Design LIGO-T970122-00- D 7/18/97

Length Sensing and Control Subsystem Preliminary Design

P. Fritschel, G. Gonzalez, A. Marin, N. Mavalavala,
D. Ouimette, L. Sievers, D. Sigg, M. Zucker

Distribution of this draft:

LSC Preliminary Design review board

This is an internal working note
of the LIGO Project.

California Institute of Technology
LIGO Project - MS 51-33
Pasadena CA 91125
Phone (818) 395-2129
Fax (818) 304-9834
E-mail: info@ligo.caltech.edu

Massachusetts Institute of Technology
LIGO Project - MS 20B-145
Cambridge, MA 01239
Phone (617) 253-4824
Fax (617) 253-7014
E-mail: info@ligo.mit.edu

WWW: http://www.ligo.caltech.edu/

1. INTRODUCTION

The LIGO Detector Length Sensing and Control (LSC) subsystem is responsible for maintaining optical resonance in the interferometer such that a linear signal, proportional to metric strain, is available at the readout. To accomplish this, LSC must determine and control four independent length degrees of freedom and the laser wavelength, as shown in Figure 1. Each of these lengths must be held to an integral number of half-wavelengths of the laser light ($\lambda = 1.06\ \mu\mathrm{m}$) with high accuracy, ranging from nm to less than .1 pm, to achieve the required precision in the strain readout. The readout is derived from control and error signals proportional to L_-, the difference in the Fabry-Perot arm cavity lengths. In addition, LSC will provide the means for calibrating this readout, and will support diagnostic testing of LSC itself and of the detector as a whole.

This document describes the preliminary design for the LIGO LSC subsystem. For orientation and context, we note some design highlights and departures from the Conceptual Design (LIGO-T960027-00-D, reviewed in April 1996) below.

1.1. Preliminary design highlights

Major advances in the design, design methodology, or its underlying experimental and theoretical basis can be found in several sections. Some highlights include:

- **Digital controls** (Section 7. and LSC CDS Conceptual Design, LIGO-T970139): Overwhelming advantages of performing LSC control compensation functions digitally, and significant obstacles in finding all-analog solutions for several key problems (e.g., control signal transmission to the end- and mod-stations; see LIGO-T960057, *ISC Inter-Station Signal Transmission*) lead us to strongly prefer digital implementation of loop controllers. This choice is reflected most in the Diagnostics design, which could not be developed to the current level without making a decision on this issue. However, detection and acquisition control designs (at this preliminary level) are generally compatible with either analog or mixed-signal implementation, with the possible exception of the guided lock acquisition controller.
- **Interferometer configuration** (Section 2. and Appendix A.): A sensing configuration was developed which is significantly more tolerant to changes in internal optical losses than previous designs.
- **Modulation system** (Section 3.1.): A prototype RF oscillator system designed to meet the stringent amplitude and phase noise requirements imposed by LIGO sensitivity goals has been built and tested.
- **Photodetectors** (Section 3.2. and Appendix B.): InGaAs photodiodes have been extensively tested, and a commercial device meeting our stringent power handling, quantum efficiency and signal-to-noise requirements was qualified. A compact baseline design meeting all technical requirements has been based on this selection.
- **Detection mode controls** (Section 4.): A new seismic excitation model was developed based on detailed Louisiana and Hanford site vibration measurements. It also employs detailed isolation stack and pendulum suspension models (developed in cooperation with SEI and SUS design teams), and takes into account local seismic correlation effects. Additional feedback paths were modeled (including split-frequency feedback to the prestabilized laser and to the common-mode length, which entails a critical performance balance) and new control compensators were developed meeting all RMS deviation, gain and residual noise requirements.

Error and feedback signals have also been simulated to verify that peak dynamic reserve and noise requirements are consistent with SUS and other subsystem constraints.

- **Lock Acquisition** (Section 5. and Appendix C.): A baseline lock acquisition sequence with stable intermediate states and well-defined transitions has been identified and validated with computer simulations (using the SMAC simulation code). Preliminary simulations have also been run to explore the nonlinear optical power transients on accidental loss of lock.
- **Calibration** (Section 6.): An analysis of errors in calibration indicates that the 5% / 50 μsec accuracy requirement can be met by post-recording reconstruction of the complete interferometer transfer function from continuous test probes at three discrete frequencies. We also propose a physically independent secondary calibration means, based on photon momentum recoil, to augment the ‘traditional’ suspension coil current/force primary calibration.
- **Diagnostics** (Section 7.): General requirements, system architecture and explicit tests have been developed for performing diagnostics both within LSC and on the full interferometer. Signal lists, monitors and test points needed to accomplish these tests have been defined.
- **Prototype/first article tests** (Section 8.): In addition to the 40-meter Recycling, Phase Noise Interferometer, and high-power photodetector testing programs, the CDS group has begun a digital control and signal processing bench test program focussed on LSC control issues.

1.2. Significant departures from the conceptual design

In the process of creating this Preliminary Design, new discoveries within the LSC system context and new conditions imposed or adopted by other subsystems have led us to revisit and modify some aspects of the design. For the convenience of those familiar with the Conceptual Design and other prior documentation, we list the most significant changes:

- **Non-resonant sideband**: We will provide an additional phase modulation signal, at a frequency which does not resonate in the recycling cavity (but which passes through the mode cleaner), for use by the ASC Wavefront Sensing system (see LIGO-T970060-00-D, *Alignment Sensing/Control Preliminary Design*).
- **Interferometer optical parameters**: Measurements on the first Core Optics Pathfinder mirrors, and finalization of the Core Optics Components specifications have led to significant changes in the interferometer mirror transmission and loss specifications, their expected ranges of variation, and coupling and loss expectations due to figure errors. This is reflected in a substantially different optical plant matrix than that assumed for the Conceptual Design.
- **Michelson differential mode sensor**: Previously, this error signal was derived from the light reflected by the recycling mirror. For nominal parameters this signal had a better signal-to-shot noise ratio than the alternate sensing point, the internal recycling cavity field pickoff. However, the reflected field sensor’s signal strength is highly sensitive to variation in optical parameters. For robustness, we will now use the internal field pickoff signal; the SNR penalty has been mitigated by a more sophisticated control loop design.
- **Feedback topology**: As shown in Figure 3, the baseline control topology will now be “balanced” to actuate on all test masses in the correct linear combinations. In addition, high frequency/low frequency crossovers are instituted in the Michelson common- and differential-mode loops (to apportion feedback between the test masses and the recycling mirror or beamsplitter, respectively) and in the arm common-mode loop (to apportion between average arm length and laser frequency correction). This reflects the choice of the recycling mirror and

beamsplitter as the "anchors," which are to be tied to the laboratory frame by their local suspension controls at low frequencies, .

- **Frequency stabilization**: The common-mode loop design is based on the adopted Detector global frequency-stabilization hierarchy (LIGO-T970088-00-D, *Frequency Stabilization: Servo Configuration and Subsystem Interface Specification*) which apportions bandwidth and defines interfaces with IO and PSL actuation systems.
- **Lock acquisition sign switching**: Analysis of the lock acquisition sequence shows that successive intermediate resonant states of the interferometer have opposite signs for certain optical plant matrix elements. These signs change at well-defined instants when cavity internal fields build to balance and then exceed incident fields. These events will now trigger state changes in the loop controller, altering feedback signs to maintain negative feedback and continue convergence toward stable operation.
- **Lock acquisition common-mode sensing point swap**: In intermediate resonant states encountered during lock acquisition, the reflected field sensor is unable to correctly determine the common-mode length error. It is therefore necessary to use the internal recycling cavity field pickoff for common-mode (laser) feedback during acquisition. Since the signal-to-shot noise ratio at this sensor is inadequate for detection mode operation at the design sensitivity, the sensors must be swapped back after successful acquisition and settling.
- **Secondary calibration**: An independent calibrator based on light momentum recoil is proposed to reduce reliance on component stability and linearity and to provide increased calibration confidence and reliability.

2. LSC FUNCTIONAL DESCRIPTION

Figure 1 shows the functional block diagram of the LSC subsystem. The components are defined and described later in this document. The principal signal and control interfaces with other detector subsystems are also shown. Some of these interfaces have special characteristics which are described in Section 2.3. below.

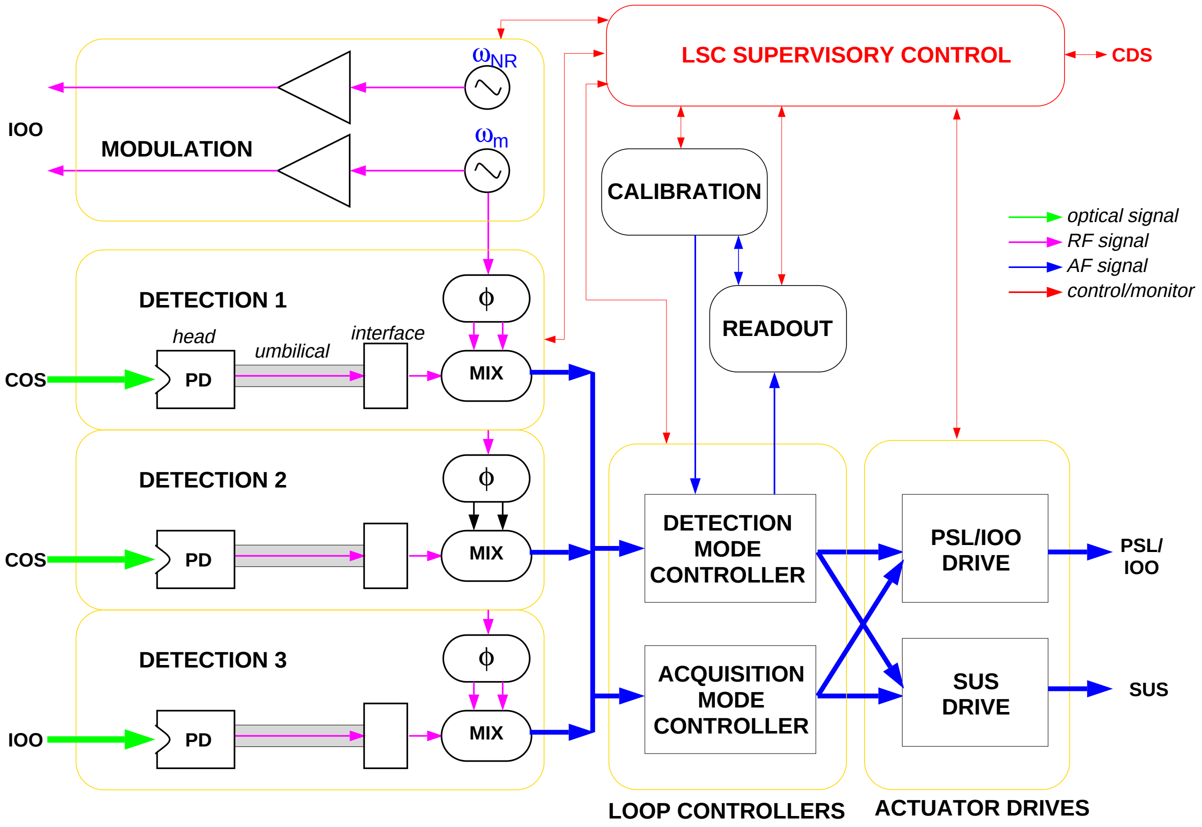

Figure 1: LSC subsystem functional block diagram, showing principal signal interfaces.

2.1. LIGO interferometer configuration

2.1.1. Degrees of freedom

The four independent lengths in the interferometer are defined as shown in Figure 2; for reference, the Michelson asymmetry and the interferometer output ports are also defined. ‘ITM’ stands for input test mass, ‘ETM’ for end test mass, ‘BS’ for beamsplitter, and ‘RM’ for recycling mirror. The frequency, wavelength and propagation constant of the laser light is denoted by ν_l, λ_l, and k_l respectively. The ‘δ’ symbol is prepended to a length symbol to indicate a deviation of that length from the nominal operating point. Error signals for the four longitudinal degrees of freedom are sensed at the interferometer output ports.

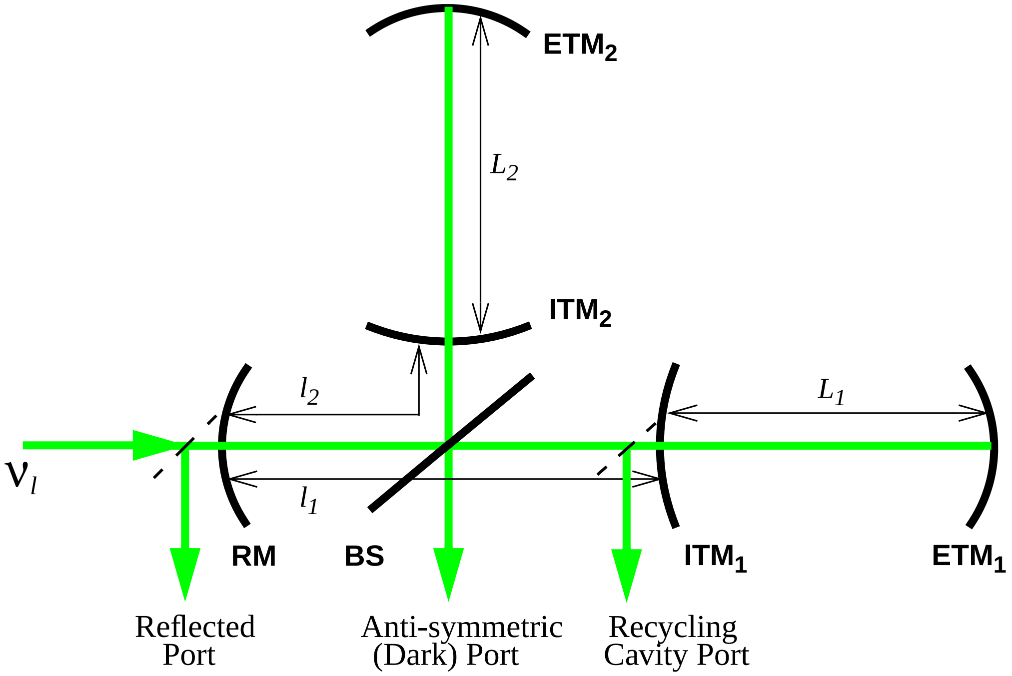

Name	*Symbol*	*Definition*	*Deviation Symbol*
Differential Arm Length	L_-	$L_1 - L_2$	δL_-
Common Arm Length	L_+	$L_1 + L_2$	δL_+
Michelson Length	l_-	$l_1 - l_2$	δl_-
Recycling Cavity Length	l_+	$l_1 + l_2$	δl_+
Michelson Asymmetry	Δl	$(l_1 - l_2)/2$	N.A.

Figure 2 Definitions of length degrees-of-freedom and output ports. 'ITM' stands for input test mass, 'ETM' for end test mass, 'BS' for beamsplitter, and 'RM' for recycling mirror. The frequency, wavelength and propagation constant of the laser light is denoted by ν_l, λ_l, and k_l respectively.

2.1.2. Modes of operation

The various operating conditions of the interferometer make it useful to define two modes of operation for the LSC. These modes and the functions that the LSC provides in each are described below.

2.1.2.1 Acquisition Mode

Acquisition Mode refers to the state in which the interferometer lengths are brought into resonance from their initial uncontrolled values. The PSL and IOO subsystems are assumed to be fully operational in this mode. The primary function of the LSC in this mode is to lock the interferometer. After lock, a settling period is required. Wire and mirror resonances are permitted to settle down (or are actively damped), filters allowed to equilibrate, control ranges are adjusted, and self-tests are completed to verify that residual excitations do not exceed Detection mode limits.

2.1.2.2 Detection Mode

In this mode the interferometer lengths are maintained at a level of stability which allows detection of strain signals within the LIGO sensitivity specifications. The functions in this mode are:

- sense and control the four interferometer lengths and the input light frequency
- provide a measure of the residual deviations of the four lengths and the light frequency
- provide a calibrated readout of the interferometer strain

2.1.2.3 Diagnostic/Calibration Mode

This is a mode (in fact a set of modes) that may be accessed from the preceding modes. The functions of this mode are:

- provide diagnostic capability to determine the performance of the LSC
- enable implementation of calibration procedures within the LSC (e.g., determination of the sensor sensitivities)
- support diagnosis of other subsystems

2.1.3. Sensing and control topology

The output beam at each of the three ports shown in Figure 2 will be sensed with a LSC photodetector. These signals give error signals for the lengths in the interferometer and are used to control the lengths and to make the final corrections of the input laser frequency. The response of the resonant interferometer to changes in these parameters is detailed in **LIGO-T970084-00-D,** *Frequency Response of the LIGO Interferometer.*

There are several options for the sensing and control configuration. Our choices for these options are discussed below:

- **Michelson differential sensing point.** An error signal for the Michelson differential length (l_-) is available from the *Q*-phase demodulation of both the reflected and recycling cavity port signals. The LSC Conceptual Design showed this error signal coming from the reflected signal, which does have better shot-noise sensitivity for the nominal interferometer parameters. However this signal is directly proportional to the amplitude of carrier light reflected from the interferometer; since the carrier will be close to critically matched, this signal is quite sensitive to losses in the interferometer and could actually become zero (or at least have a very poor sensitivity) if the losses turn out to be different than predicted or change from their initial values. For this reason we choose instead to use the *Q*-phase demodulated signal from the recycling cavity port for the Michelson control. We will continue to have the *Q*-phase signal from the reflected port available, so that it can be used for control if the other signal turns out to be a poor choice.

- **Common mode sensors.** The *I*-phase signals from the reflected and recycling ports are both mainly sensitive to the common arm length (L_+), with a smaller sensitivity to the recycling cavity length (l_+); when one of these signals is controlled to zero (by actuating on the common arm length and laser frequency), the other signal is then sensitive only to the recycling cavity length. We choose to condition the plant by enforcing such a gain hierarchy (rather than by diagonalizing the sensor signals), but we have the choice of which signal to send to the common arm length/laser frequency, and which to send to the recycling cavity length. The reflected signal has a better shot-noise sensitivity for frequency detection, and in Detection Mode we need this sensitivity to meet the residual frequency noise requirement. In Acquisition Mode, however, we use the recycling cavity signal to feed back to the arm length/laser frequency (see Section 5.). So for acquisition, the recycling cavity signal is fed to the arm length/laser frequency and the reflected signal is fed to the recycling cavity length; in Detection Mode, these sensor signals are swapped.
- **Control configuration.** In the Conceptual Design it was stated that the four error signals would all be fed back to the test masses (only at low frequencies for the arm common signal); this was the result of wanting to avoid leaving any of the test masses (or some linear combination of the test masses) under local suspension control. However, for simplicity the control design used actuation of the recycling mirror and beamsplitter for RC and Michelson length control loops; this simplification neglects cross-couplings in the controls from these degrees-of-freedom to the gravitational wave (gw) channel. Such cross-couplings, which will arise from errors in actuating all four test masses with the same amplitude, are estimated to occur at a level of ~5%; this allows the sensing noise of the RC and Michelson loops to feed into the gw channel and puts restrictions on the bandwidths of these loop paths. In the current design we maintain the philosophy that led to actuating on all the test masses, but with the following modification that deals with the cross-coupling problem. The RC and Michelson signals are fed back to the four test masses at low frequencies to provide damping of the pendula, and at higher frequencies they control the recycling mirror and beamsplitter, respectively; the cross-over frequency between the two paths will be 1-2 Hz, and the test mass path will be rolled off quickly above ~10 Hz in order to filter out the sensing noise before it can leak into the gw channel. This still leaves a roughly 1% cross-coupling of the Michelson signal into the gw channel, simply because the anti-symmetric output is sensitive to $(L_- + \pi l_- / 2F)$. This coupling can be reduced by multiplying the Michelson control signal by ($\pi/2F$) and adding it with the appropriate sign to the differential arm control signal that actuates the end test masses (this can probably be done to ~5%, giving a reduction in the cross-coupling by a factor of ~20). We are retaining this possibility as an option in the design.

The sensing and control configuration is shown schematically in Figure 3.

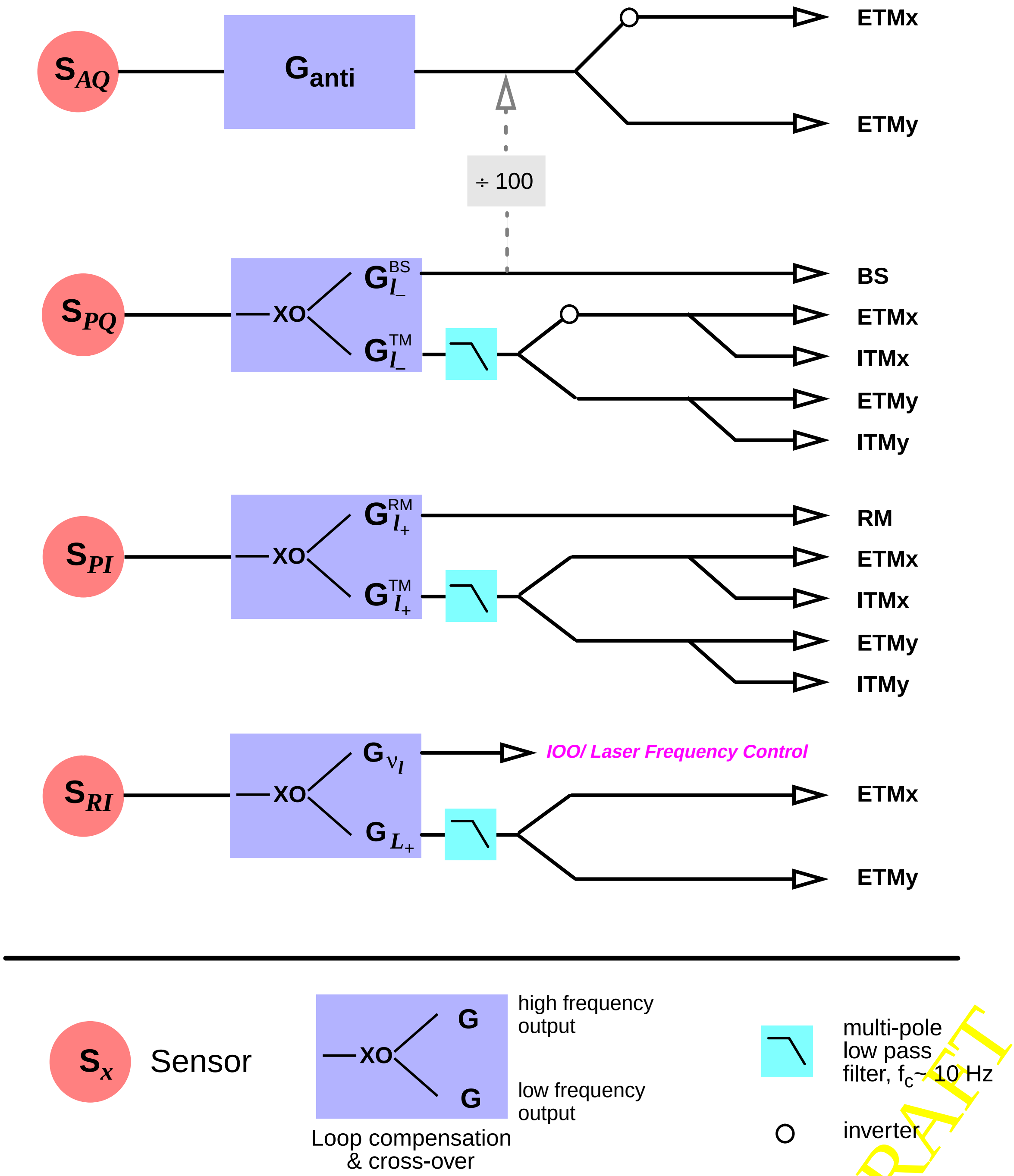

Figure 3: Sensing & control configuration diagram. For all loops other than the gravity wave channel (top), the sensor signals are fed to the test masses at low frequencies (to damp the pendula), and are crossed over to the beamsplitter, recycling mirror and laser frequency actuator at higher frequencies; the cross-over frequency will be 1-2 Hz. The test mass path is low-pass filtered at ~10× the cross-over frequency in order to eliminate the sensor noise from the gravity wave channel. Also shown is an optional control path that adds approximately 1/100 of the Michelson control signal to the L_- control signal in order to further reduce the contribution of the Michelson sensing noise in the gravity wave channel.

2.2. Baseline interferometer optical parameters & design ranges

The baseline optical parameters for the interferometer are given in **LIGO-T970098-00-D,** *Proposed Interferometer Parameters.* A revised requirement on loss of under 50 ppm per mirror surface and recent specification of the reflectivities of the AR coated surfaces has led ISC to adopt the parameters outlined in **LIGO-T970098-00-D**. The parameters for the 4km interferometers are summarized in Table 1 ; some parameters have been significantly modified compared to those used in the LSC Conceptual Design.

Parameter	*Value (units)*
Mirror coatings	
Loss per surface	50 ppm
ETM HR transmission	15 ppm
ITM HR transmission	0.02995
ITM AR reflectivity	600 ppm
BS reflectivity = transmission	0.499975
BS AR reflectivity	200 ppm
RM reflectivity	0.0244
Mirror radii of curvature	
ETM	7400 m
ITM	14571 m
RM	9998.65 m
Interferometer lengths	
Arm cavity	3999.01 m
Recycling cavity	9.38 m
Michelson asymmetry	0.215 m[a]
RF modulation	
Resonant sideband frequency	23.9706 MHz
Resonant sideband modulation index	0.45
Input power	6.0 W
Carrier wavelength	1.064 µm

Table 1: Parameters used in LSC servo modeling and noise studies; 4 km interferometer.

[a] Deliberately inflated to simulate 1% additional loss for the resonant sidebands in the degenerate recycling cavity, as given by FFT runs. Optimum asymmetry is 0.16 m.

The LSC design must take into consideration the uncertainty in the expected mirror losses (30 ± 20 ppm), which leads to the modified sensing topology proposed in Section 2.1.3. The LSC servo modeling and noise studies are based on a point design using the worst-case loss of 50 ppm per mirror surface, but design choices emphasize robustness against small changes in interferometer configuration, especially increased losses due to mirror degradation/contamination. FFT simulations with λ/400 mirror surfaces and 50 ppm loss show a 1-2% loss for the resonant sidebands in the degenerate recycling cavity, so the sidebands are necessarily undercoupled. In this case, the signs of the longitudinal error signals are entirely independent of the carrier coupling if the l_- signal is sensed at the recycling cavity port (Q-phase demodulation) rather than at the reflection port. The recycling cavity signal has a worse (larger by a factor of ~5) shot noise limited sensitivity than the reflection port signal, but since the latter is a strong function of the carrier losses, the two signals would have equal sensitivity if there were an additional 40 ppm of loss in the arm cavities. The degraded sensitivity does indeed impose a more stringent constraint on the detection mode controller gain, but the servo design shown in Section 4.4. nonetheless meets the performance requirements.

2.3. Related subsystems and principal interfaces

2.3.1. Input optics and prestabilized laser

The LSC makes the final corrections to the laser frequency through frequency actuators in the IOO subsystem. Specifically, there are two inputs to the IOO for frequency actuation: one for control of the mode cleaner length, and a second that is a summing input to the IOO frequency stabilization loop after the mode cleaner demodulator (i.e., the additive offset). Both inputs will be used, the former at low frequencies and the latter at high frequencies. Separate inputs to the IOO are retained so that the LSC has control over the cross-over between them. This configuration and the interface are detailed in **LIGO-T970088-00-D,** *Frequency Stabilization: Servo Configuration & Subsystem Interface Specification.* The interface specification from this document is shown here in Table 2 .

Parameter	*Specification*
MC Additive Offset input	
Signal Type (analog/digital)	TBD (baseline: analog)
Signal Coupling (if analog)	DC
Signal Range (if analog)	± 15 V
Sensitivity	TBD (Hz/V)
Frequency response:	
Magnitude	Flat within 2 dB up to 20 kHz; f > 20 kHz: magnitude < (f /20kHz) × (avg. resp. below 20 kHz)
Phase	Phase lag at 20 kHz, $\phi < 20°$
Control range	± 2 kHz
MC Length correction input	
Signal Coupling	DC
Signal Range	± 15 V
DC Sensitivity	TBD (m/V)
Frequency response	response of a damped 1 Hz pendulum
Control Range	± 1 µm

Table 2: Interface specification for the IOO (MC) external frequency/length control

On very long (tidal) time scales, the laser frequency is required to track the average arm length changes (the SEI actuators not having sufficient range). To implement this, the LSC L_+ sensor is fed back directly to the PSL to change its frequency on tidal time scales. This interface is also detailed in **LIGO-T970088-00-D,** and the specifications are shown in Table 3 .

Parameter	*Specification*
Tidal correction input	
Signal Type	Analog
Signal Coupling	DC
Signal Range	± 15 V
Sensitivity	TBD (Hz/V)
Frequency response	Step response time constant < 1 hour
Control Range	± 30 MHz

Table 3: Interface specifications for the PSL tidal correction input

Finally, the LSC produces the phase modulation waveforms needed for interferometer length and alignment sensing, and supplies them to the IOO. The details of this interface will depend on the design of the phase modulators used in the IOO (undefined at this point). The interface parameters that will need to be specified are: modulation coefficient (radians/volt); input impedance; connector type; maximum RF power.

2.3.2. Alignment Sensing and Control

The ASC uses samples of the same interferometer output beams used for LSC, and the optical tables near the chamber beam ports will be shared between LSC and ASC. The optical tables are carried under the ASC scope of work. A preliminary layout of such a shared table is shown in the Photodetector section of this document.

The LSC provides the modulation waveform for producing the ‘non-resonant sidebands’, which are needed by the ASC to detect some alignment degrees-of-freedom of the interferometer. A sufficient range of modulation depth control will be provided for operation and diagnostics of the ASC.

2.3.3. Data Acquisition

A draft list of the LSC channels that will be acquired by the DAQ system is found in Table 4 . As the electronics design advances, there will undoubtedly be changes to this list. The detailed interface between the LSC channels and the DAQ is not yet defined.

Name	*Description*	*No.*	*Rate (samples/sec)*
Sensor signals			
S_{AQ}	dark port signal	1	16384
S_{RI}	reflection signal	1	16384
S^x_{PQ}	pick-off x differential signal	1	16384
S^x_{PI}	pick-off x common signal	1	16384
S^y_{PQ}	pick-off y differential signal	1	16384
S^y_{PI}	pick-off y common signal	1	16384
S_{AI}	dark port orthogonal signal	1	16384
S_{RQ}	reflection orthogonal signal	1	16384
S_{DC}	photodiode DC signals, sum for each sensor	4	16384
V_b	photodiode bias voltages	4×4	2
T_d	photodiode temperature	4×4	2
Controller signals			
G_A	differential arm cavity length	1	16384
G_{l_-}	Michelson length	1	2048
G_{l_+}	recycling cavity length	1	2048
G_{ν_l}	laser frequency	1	16384
G_{L_+}	common arm length	1	2048
I_{coil}	SUS coil driver read-back, ETMs	2×4	16384
	SUS coil driver read-back, ITMs, BS, RM	4×4	2048
Status signals			
	length servo status	64	2
RF Modulation signals			
	forward power to modulator	2	2
	reverse power from modulator	2	2
	LO drive level	2	2
Calibration signals			
S_{stim}	stimulus signal	1	16384
PD_{pa}	photon actuator photodetector signal	1	16384

Table 4: LSC DAQ channel count

3. SENSING

3.1. RF modulation and demodulation

LSC, ASC and IO interferometric sensing systems rely on radiofrequency phase modulation of the laser beam and homodyne demodulation of detected photocurrents for their sensing functions. The baseline requires at least two and possibly three distinct modulation frequencies;

- the Resonant Sideband frequency f_R. Upper and lower sidebands generated by phase modulation at this frequency are transmitted by the IO mode cleaner (along with the carrier) and are also resonant in the recycling cavity (when the arm cavities are resonant with the carrier). This modulation signal is used for all LSC length sensing functions, as well as some ASC Wavefront Sensing functions. It has stringent noise and spectral purity requirements.
- the Nonresonant Sideband frequency f_{NR}. Sidebands at this frequency are transmitted by the IO mode cleaner along with the carrier, but are rejected by the recycling cavity. This modulation is provided purely for ASC wavefront sensing purposes. Requirements on this waveform are less stringent.
- the Mode Cleaner length sensing frequency f_{MC}. This frequency (if used-- TBD by IO) is chosen to be rejected by the mode cleaner, and is used purely for sensing and controlling the resonant length of that cavity with respect to the laser frequency. Requirements on this modulation waveform's spectral purity are also expected to be less stringent (TBD by IO).

The frequency f_R is constrained by joint optical path length and RF wavelength conditions, and was selected on the basis of facility geometric constraints and other figures of merit as outlined in LIGO-T960122, *Proposed Initial Detector MC and RC Baseline Lengths* and LIGO-T970068-00-D, *Recycling Cavity and Mode Cleaner Cavity Baseline Dimensions*. The current baseline modulation frequencies are as follows:

Table 5: Baseline frequencies for the resonant sideband

IFO	FSR_{MC} (MHz)	f_R (MHz)
WA, LA 4 km	12.231	24.463
WA 2 km	9.816	29.449

Frequencies for the nonresonant sidebands f_{NR} must be approximately an integer multiple of the mode cleaner free spectral range FSR_{MC}, but not resonant in the recycling cavity; these frequencies (and their tolerances with respect to the constrained parameters) are TBD. At present the third frequency f_{MC} is also TBD; if used, it will be chosen to avoid integer multiples of FSR_{MC} and the other frequencies used.

IO will provide electrooptic modulators, placed at the input to the IO Mode Cleaner, to apply these phase modulations to the main laser beam. LSC will provide sinusoidal RF signals at power levels and matching impedances appropriate to achieve the required modulation indices (approximately $\Gamma = 0.5$ for f_R and $\Gamma = 0.05$ for f_{NR}), given the RF impedance and electrooptic coefficient of the devices selected[1].

LSC must also implement the demodulation of detected RF photocurrents to provide the baseband length and laser frequency error signals described in Section 2.1. Although only four of the six possible signals shown are planned for control use, we will demodulate all three detector signals in both I and Q phases (6 independent signals total, plus two additional for a “spare” detector TBD) to provide additional diagnostic information and a means of fine-tuning the effective demodulation phase.

3.1.1. Modulation requirements summary

We discuss some of the more stringent requirements from the LSC DRD (LIGO-T960058-00-I) applicable to the resonant sideband modulation at f_R. Oscillator amplitude noise corrupts the strain signal via modulation of the residual rms deviation in the differential length, in essentially the same way as laser intensity noise. If the L_- length deviation requirement of 10^{-13} $\mathrm{m_{rms}}$ is just met, a fractional stability $\delta\Gamma(f)/\Gamma \le 4.5 \times 10^{-8}/\sqrt{\mathrm{Hz}}$ is needed at fluctuation frequencies greater than 200 Hz. Oscillator phase noise may be converted into amplitude noise through deviations from exact resonance in the mode cleaner, which can then introduce noise through the same mechanism. For plausible conditions of mode cleaner detuning, this consideration leads to a requirement of $\delta\phi \le 4 \times 10^{-5}$ rad/$\sqrt{\mathrm{Hz}}$ at 200 Hz falling off as $1/f$ at higher frequencies. Oscillator amplitude and phase noise do not couple to first order to in-phase — and, therefore, common-mode — signals.

Other requirements are motivated by the system context and diagnostic capabilities. To analyze the effect of residual phase and amplitude fluctuations, it will be necessary to modulate the amplitude and phase of the final waveform with a user-specified modulation function. It is also necessary to change the modulation index (i.e., RF voltage to the modulator) over approximately 1.5 decades to perform various diagnostic tests (e.g., modematching, gain compression, cross-modulation products, intensity noise, and so on). Fine frequency tuning (of order 10 Hz range) may be required to actively follow tidal dilation of the interferometer without deviation from the exact co-resonance conditions discussed above. Finally, certain second-order noise mechanisms may require the rate of change of relative phase between the two or three oscillators in a given interferometer to be tightly controlled, as through a frequency-offset lock or direct digital synthesis. Since the stringent phase noise requirement placed on the f_R waveform is likely to be incompatible with PLL or DDS generation, the f_R source may be used as the “master” clock and the other frequency(ies) derived from it. Detailed requirements on this aspect of oscillator performance remain TBD.

---

[1] The modulation index is given by $\Gamma = \pi V/V_\pi$. For a commercially available resonant MgO:LiNbO$_3$ electro-optic modulation cell (New Focus model 4001, for example), $V_\pi \sim 20$ V into a matched impedance of 50 Ω, thus requiring 6.4 $V_{0\text{-pk}}$ or 0.4 W of RF power to achieve a modulation index of 1.

3.1.2. Modulation source prototype design & performance

The challenging f_R oscillator noise requirements were confronted with a prototype system, built by LIGO CDS and Vectronics Microwave Corp. for testing in the 40m interferometer as part of the Recycling Demonstration program. Design specifications for this prototype are described in LIGO-T960071-00-D, *40 m Reference Source System Specification.* Two units have been fabricated and have undergone preliminary testing (one of these is now permanently installed in the 40m interferometer). Their maximum RF output power is 4.2 W at 32.7 MHz. The phase noise was shown to meet the specification at all relevant offset frequencies. The amplitude noise has been shown to be no more than 10 dB above the specification, but these measurements were limited at this level by the noise floor of the measuring instruments; as a result we can only say that performance is consistent with meeting the specification. Improved AM testing methods are under development.

3.2. RF photodetectors

3.2.1. Introduction and physical locations

LSC will provide RF Photodetector (PD) assemblies to detect the modulated output beam intensities corresponding to length and frequency changes in the interferometer. These photodetector assemblies are integrated with ASC Wavefront Sensing equipment on external ISC platforms located in the LVEA. Figure 4 shows sample locations of these detectors for one interferometer (the Louisiana 4km). The three locations corresponds to the reflected port (R), anti-symmetric or dark port (A) and recycling cavity pickoff port (P). Additional locations (TBD) will be used for another detector monitoring the recycling cavity pickoff on the opposite arm (P’).

Figure 5 (which is adapted from the ASC PDD, LIGO-T970060-00-D) shows schematically one ISC table configuration including a Photodetector Assembly. Also shown is an electromechanical shutter which is used to block ASC and LSC detectors for safety and diagnostics; this is also provided as part of the LSC package for integration on the ISC platform.

3.2.2. Requirements summary and basic design features

FFT model studies of LIGO interferometers with realistic mirror deformations indicate that with a nominal input power of 6 W incident on the recycling mirror, and other parameters optimized for minimum shot noise, the antisymmetric port will emit up to 600 mW of power in normal steady-state operation (*W. Kells, private communication*). This steady-state power level essentially demands division of the beam among multiple discrete photodiode devices. The number of devices required to accept this power level, combined with the additional minimum requirement of 80% quantum efficiency[1] at 1064 nm wavelength, essentially rules out use of silicon photodiodes. Our research program and preliminary design is thus based on InGaAs PIN photodiodes.

---

[1] This quantum efficiency is defined as the “external” QE, and is calculated to include all losses between the vacuum viewport providing the ISC sensing beam and the detected RF photocurrent. The viewport and all in-vacuo optics are provided COS; their transmission efficiency is governed by a separate requirement (COS DRD, LIGO-T970071-01-D).

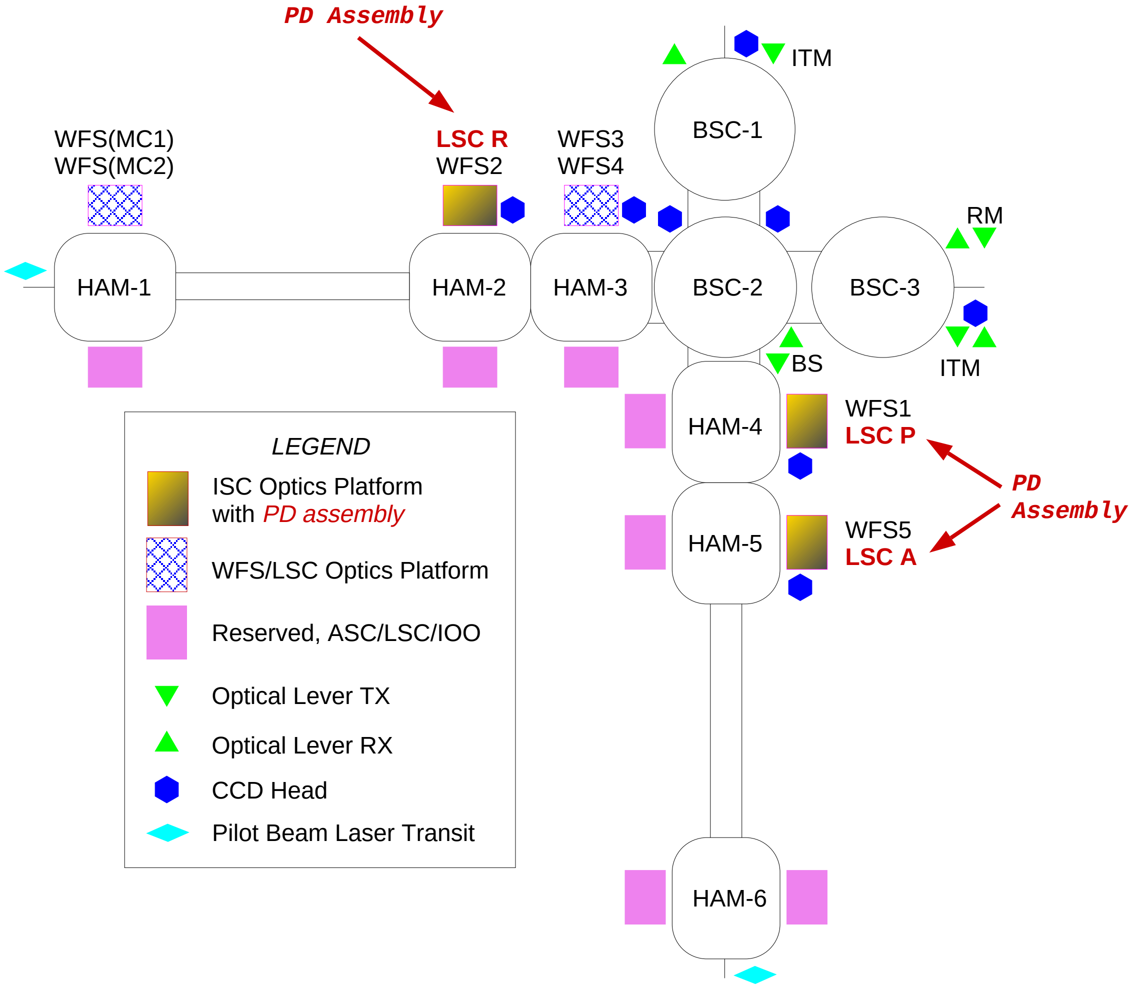

Figure 4: ISC Tables with PD Assembly Location

Photodetector assemblies also need to handle transients at much higher powers. Preliminary modeling (Appendix C) indicates that on sudden loss of lock, the entire stored circulating energy in the interferometer, of order 2 J, is dumped out the antisymmetric port. The peak power reached depends on the rate of mirror motion associated with unlocking, which has not been reliably estimated (although two cases, which can be regarded as extreme and very extreme, are modeled in Appendix C). Also, when the interferometer has unlocked or is waiting to acquire lock, the entire incident power of 6 W returns from the reflected port onto the common-mode detector.

Additional detector requirements derive from the requirement to limit phase noise contamination due to backscatter from the detector surface. These requirements are discussed in the LSC DRD (LIGO-T960058-02-D) and the COS DRD (LIGO-T970071-01-D).

The need to detect the photocurrent without contamination from electronic or thermal noise in the detection electronics presents one of the most challenging requirements. As shown in Appendix B.1., the high capacitance and relative dissipation of InGaAs photodiodes at RF frequencies (especially for large-area devices) severely limits the achievable SNR.

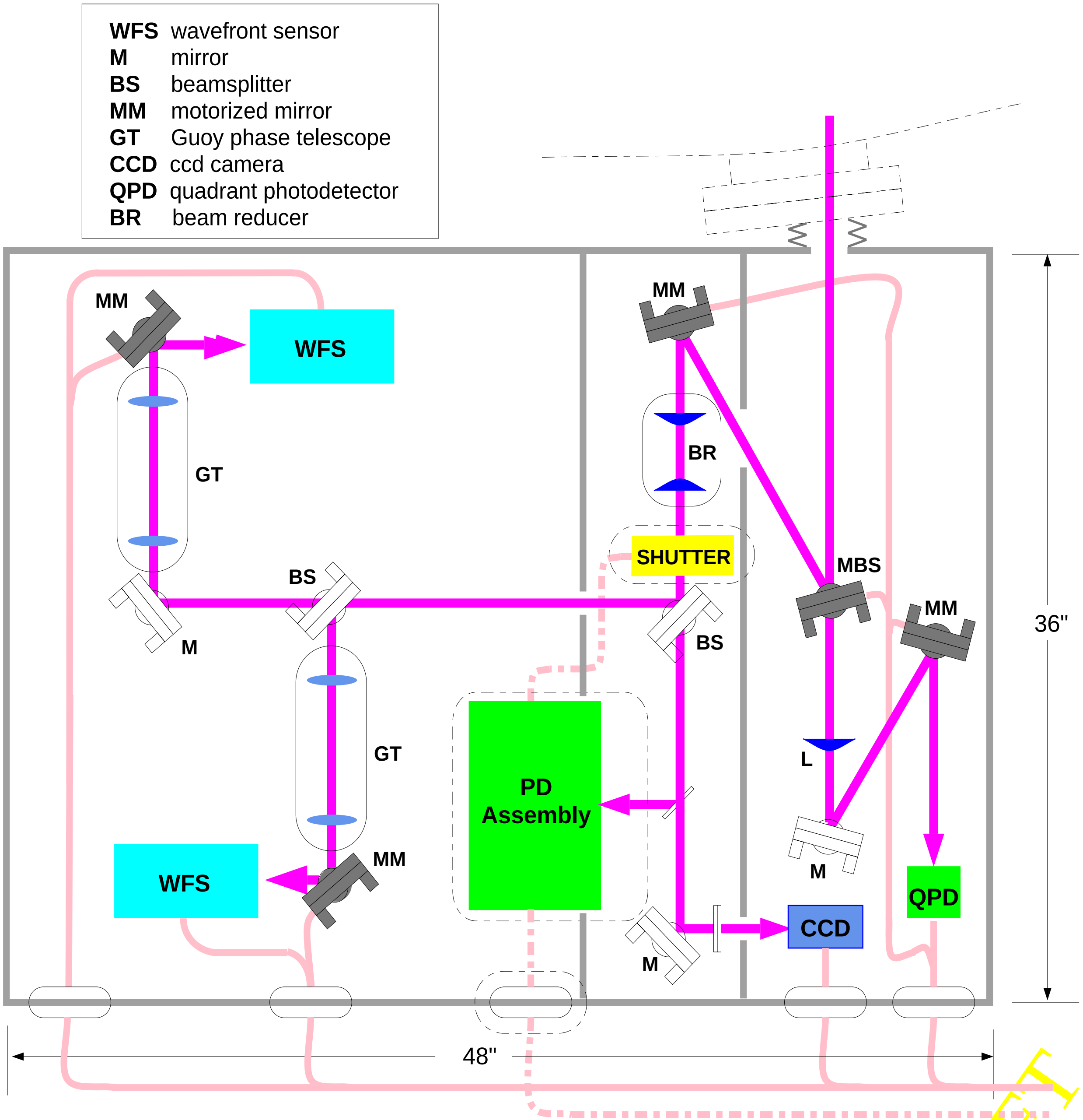

Figure 5: Preliminary ISC table layout with PD Assembly

3.2.3. Photodiode device selection

The VIRGO project has done extensive research to characterize candidate photodetector devices and select both a device and an assembly design which is capable of satisfying these (or similar) requirements (see *Diodes selection, the first approach*, VIRGO internal report PJT94-014, by A. Dominjon and M. Yvert, 5/94). Building on the VIRGO work, we have extended the testing of the selected devices (Hamamatsu InGaAs diodes in 1 mm, 2 mm and 3 mm diameter) and focussed on particular LIGO requirements. The objectives, methods and preliminary results of this testing program are discussed in Appendix B.2. We briefly summarize the more salient results as follows:

- Intensity dependence: Using probe beams as small as 0.02 mm^2, we found that there are no significant density limitations at intensities corresponding to over 5 W/mm^2. This admits solutions involving relatively small detector areas and focussed beams; linearity limits appear more related to total power than power per unit area.
- Spatial uniformity: Uniformity in both the RF and DC response appears to be adequate for immunity from scattered light phase noise.
- RF impedance: The high capacitance per unit area of InGaAs detectors tested proved a formidable problem due to SNR concerns (see below). Fortunately, the 2 mm candidate devices selected are acceptable (see below).
- Quantum efficiency: With windows removed, the bare diode devices are able to achieve 82% internal quantum efficiency at the design wavelength. The diode face reflectance is approximately 0.7% near normal incidence. To meet the 80% overall QE target, the beam forming and dividing optics are thus allocated a maximum total loss (reflection and absorption) of 1.3% or less. This is a very tight requirement, but appears feasible for the baseline design if we use high-quality custom coatings.
- Thermal properties: The thermal impedance of the device packages, combined with the measured variation in impedance and optical properties with junction temperature, is consistent with continuous operation within specifications at LIGO power levels.
- Overload transient power handling: No irreversible change in properties was observed up to incident power of 400 mW on a single device. Although an increase in dark current was observed after exposure to higher power (approximately 700 mW), the duration of this exposure and junction temperature during the test were not logged, and the full bias voltage was maintained; as a result it is not possible to extrapolate this measurement to a limit in actual practice. Further tests are planned.
- Stability under operating conditions: At this writing a 2 mm diode has undergone over 400 hours of continuous exposure to approximately 200 mW incident power, nearly twice the nominal design power per device, with no perceptible change in its properties (at a test sensitivity of a few percent).

One way to summarize the various considerations in diode selection is to evaluate the photocurrent per device needed to provide an adequate SNR with respect to preamplifier thermal noise. The results of this evaluation for three Hamamatsu parts tested by LIGO, and a variant tested by VIRGO, are shown in Table 5. The 2 mm Hamamatsu G5832-2 affords the best compromise

Table 6: Optimized RF transimpedance and minimum DC current per device to fulfill LIGO SNR requirements (Section B.1.**)**

Description	*Z [ohm] at 25MHz, 10 V bias*	I_{PD}^{min} *[mA]*	*# PDs req'd*	*Power per PD [mW]*	*Central Intensity*[a] *[mW/mm^2]*	*DC Current per PD [mA]*
G5832-1 (1mm)	682	6	8	75	765	53
G5832-2 (2mm)	81	95	4	150	382	105
G5832-3 (3mm)	18	1100	< 1[b]	N/A	N/A	N/A
G5114-3[c] (3mm)	31	454	1	600	678	420

a. Assuming $1/e^2$ beam diameter is chosen to be half the physical diameter of the diode; this is conservative from the standpoint of collection efficiency, but may be necessary to reduce backscattering from the device edges.

b. The RF impedance of the stock 3 mm diode is too low to realize LIGO SNR constraints (with room-temperature electronics).

c. VIRGO custom diode, modified for low capacitance (RF impedance parameters communicated by R. Flaminio).

between complexity (number of discrete devices), power density and SNR margin. An arrangement using four such devices in parallel is the basis of our preliminary design. It is worth noting that, with some relaxation of SNR requirements, the VIRGO custom 3 mm diode might be acceptable[1], and that a solution using 8 (or more) 1 mm diodes would afford some advantages in SNR at the cost of higher complexity and higher peak intensity. The 8-diode design will be carried as a backup option at least through qualification of the first article.

3.2.4. Baseline Photodetector Assembly Design and Projected Performance

Based on the Hamamatsu G5832-2 photodiode's measured properties, we can define the following basic optical parameters for the photodiode assembly:

- The beam diameter ($1/e^2$ intensity) at each detector surface will be 1.0 mm (TBR).
- All diodes will be placed at equal optical path distances from the interferometer (tolerance TBD)
- The diodes will be canted at a 10 degree angle (nominally upward) to divert the specularly reflected beam (approximately 0.7% of incident power) out of the Rayleigh cone. A beam dump will be integrated into the case cover to trap and dissipate this beam without added backscatter.
- A means will be provided to introduce incoherent light to each diode (as from an incandescent lamp), at a level sufficient to introduce shot noise equal to the dark noise of the RF readout.

---

1. Several factors permit VIRGO to tolerate the higher capacitance of this diode while LIGO cannot; the most important difference is the choice of a lower modulation frequency in VIRGO.

The following basic electronic design parameters are also proposed:

- Each diode will be back-biased at 10V
- Heatsinking will be designed to maintain a case temperature below 45^oC under operating conditions (the expected operating junction temperature is approximately 80^oC).
- The nominal operating photocurrent will be 105 mA per diode.
- For the expected RF transimpedance of 81Ω, a pre-mixer RF voltage gain of 20 dB will be used in the preamplifier in Detection mode.
- With this gain, preamplifier noise of 1.2 nV/Hz$^{1/2}$ referred to input will be adequate to guarantee that electronic noise from this and subsequent RF and baseband stages remains below the SNR specification, and at the same time retains adequate dynamic reserve at the mixer.
- To protect against excessive internal power dissipation, the bias voltage across each diode will be cut off under overload conditions. This will reduce the internal device dissipation by a factor of 7.7. The triggering threshold, reset criteria and response time interval necessary to protect the diode are TBD, pending further testing on damage thresholds and modeling of interferometer-generated power transients.
- In addition, LSC will provide a shutter for dark tests and potentially also for overload protection of LSC and ASC components. Requirements related to this second application remain TBD pending further analysis of expected overload damage thresholds and timescales.
- In some cases (e.g., lock acquisition of the common-mode control, where the photodetector will be exposed to the full 6 W laser input power until lock is acquired) a linear signal is still required during overload conditions. Either the photodetector assembly will maintain some well-defined nonzero sensitivity in its “overload protected” state, or a separate low-sensitivity detector (perhaps receiving a small light sample, of order 1%) will be provided to augment the dynamic range.

Figure 6 presents the PD assembly schematically. The design is proposed to be modular, to accommodate as many as 8 diodes and their optics and electronics. To maintain equal pathlengths and equal power levels on all devices a system of 50:50 beamsplitters will be used in the 4-diode configuration, and a system of 50:50, 67:33 and 75:25 splitters will be used in an 8-diode configuration.

The diodes will be mounted on a plate which will play the role of a common heat sink. Air cooling will be adequate to maintain this plate below the required 45 degrees C under operating conditions (approximately 5W is dissipated by all the photodiodes in normal operation). Electronics will be housed in the area on the lower right of the diagram, behind the heat sink plate; RF tank circuits and front ends will be mounted close to the diode terminals to minimize stray inductance and capacitance. Thermocouples mounted near one or more diode cases may be used to monitor heat sink temperature during operation. Within the optics housing (upper left), a system for introducing incoherent light onto each diode for testing purposes will also be integrated. This requirement has proven difficult to realize in practice; incandescent lamps which produce the required photocurrent (of order 10 mA) are too large and introduce too much heat. A system using fiberoptic light guides and a remote lamp is under consideration. The optics housing also acts as an RFI shield, and will be gasketed for shielding purposes. The light entry (upper left) is designed as a waveguide with the modulation frequency below cutoff for further RFI rejection. The lid of the optics housing will also house low-backscatter light traps to absorb the specular reflections.

If all coating losses Λ_R (scatter + absorption) are assumed to be comparable for beamsplitting surfaces, and substrate losses Λ_A (bulk absorption + back surface AR coating reflection) are also assumed to be similar, it can be shown that the total optical transmission loss for this configuration, including lenses required for beam focusing, is $(1-2\Lambda_R-\Lambda_A)^4$. If $\Lambda_R = 100\,ppm$ and $\Lambda_A = 500\,ppm$, the total loss in optical components is thus about 0.3%, which is tolerable. However, these are state-of-the-art “supermirror” coating losses and it may be difficult to realize this level. Backscattering concerns may also argue for ultralow surface microroughness; this will be investigated during the final design phase.

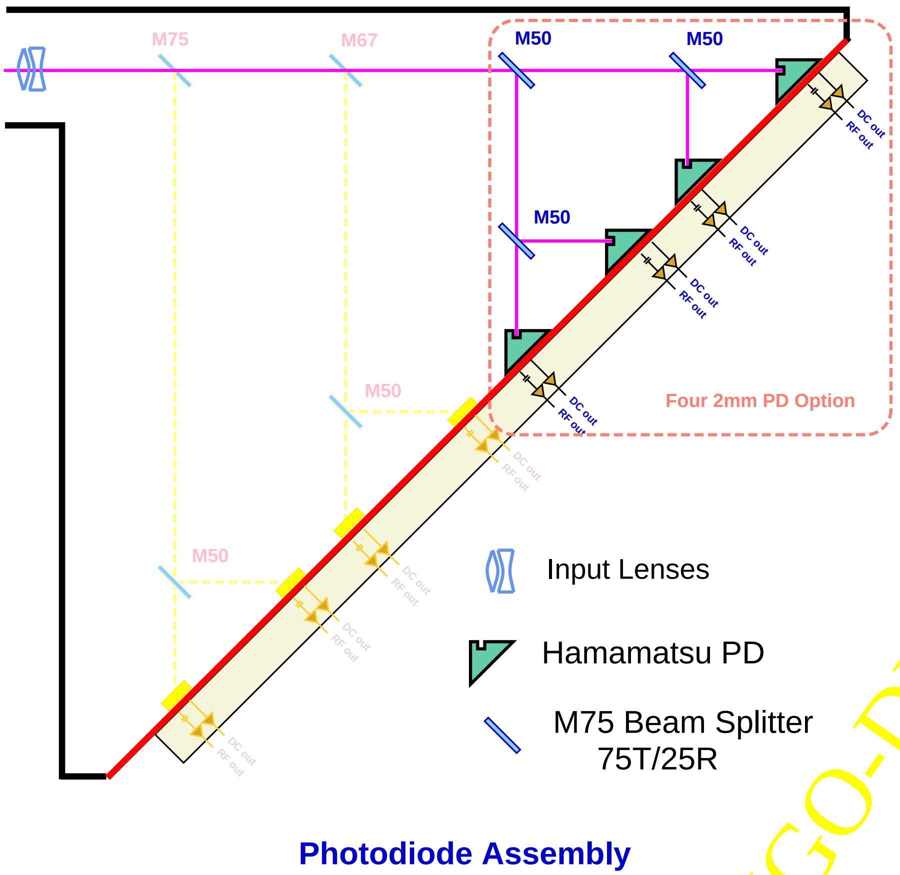

Figure 6: Photodiode Assembly Layout with full implementation (8 photodiodes). The 4-diode option is shown in the dashed box.

4. DETECTION MODE CONTROLS

The feedback topology planned for Detection Mode was outlined in section 2.1. The frequency response, added noise and dynamic reserve of the signal paths which implement this topology must satisfy the requirements of suppressing seismically-induced motion and other technical noise, linearizing the strain output, and maintaining robust stability margins in the face of unknown or fluctuating optical, mechanical and environmental conditions. These requirements are cast in terms of the control system performance measures below; a preliminary design meeting these criteria is then presented. The projected performance and some options for further improvement, both to the design itself and to the analysis methodology, are also highlighted to preview our final design phase.

4.1. Requirements summary

The residual deviations in the controlled degrees-of-freedom must be below the levels given in the LSC DRD, T960058-03-I. These are summarized as follows:

- The requirement on the anti-symmetric port degree-of-freedom is stated in meters as $(\delta L_- + (\pi/(2F))\delta l_-) \le 1\times10^{-13}\ \mathrm{m}$. We interpret this to mean the signal δS_{AQ} at the dark port, converted into equivalent δL_- meters through the interferometer optical plant transfer function dS_{AQ}/dL_-, must satisfy $\delta S_{AQ}/(dS_{AQ}/dL_-) \le 1\times10^{-13}\ \mathrm{m}$.
- The requirement on the pick-off d.o.f. is stated as $(\delta l_- + (\pi/(2F))\delta L_-) \le 1\times10^{-9}\ \mathrm{m}$, and similarly, we interpret this as $\delta S_{PQ}/(dS_{PQ}/dl_-) \le 1\times10^{-9}\ \mathrm{m}$.
- The requirement on the arm common mode d.o.f. is $\delta(k_l \cdot L_+) \le 9\times10^{-6}\ \mathrm{rad}$.
- The requirement on the recycling cavity length is stated as $\delta l_+ \le 1.25\times10^{-10}\ \mathrm{m}$, which we will interpret as $\delta(k_l \cdot l_+) \le 7\times10^{-4}\ \mathrm{radian}$.

- The requirement on the laser frequency noise is also given in the LSC DRD. We will calculate this coupling as

$$\left(\frac{dS_{DP}/d\nu_l}{dS_{DP}/dL_-}\right)\frac{\delta\nu_l}{4\mathrm{km}} \le \mathrm{SRD}/10$$

where $\delta\nu_l$ is the residual frequency noise after being stabilized by the common mode loop and SRD is the top-level strain sensitivity requirement given in LIGO-E950018-00-E, *LIGO Science Requirements Document.*

- The noise due to the auxiliary (non- gravity wave) loops should not contribute more than 0.1 the SRD level to the gw signal.

These are the top level requirements as given in the LSC DRD. Clearly the servo design must also yield stable performance, i.e. the loops must not oscillate. A practical limit to the servo bandwidths is imposed by the internal mechanical resonances of the actuators (the suspended optics). In designing the servo loops, we thus impose an additional requirement on the loop gains to ensure that these resonances can not produce an instability. We assume the following very conservative requirement:

- At the mirrors' internal mode frequencies, the gains must be no more than 1/10 of the Q of the mode (approximately 10^6). Thus:
  - For loops actuating on the test masses and the recycling mirror, the gains should be lower than $Q/10 \sim 10^{-7}$ at 9.4 kHz, the first axisymmetric mode (the first mode occurs at 6.8 kHz, but is non-axisymmetric, with diametric, parity, and order numbers of 2,1,1).
  - For the loop actuating on the beamsplitter, the gain must be less than 10^{-7} at 5.25 kHz, the first axisymmetric mode (the first mode occurs at 3.6 kHz, but is non-axisymmetric, with diametric, parity, and order numbers of 2,1,1).

During the final design we will investigate the detailed constraints that the internal modes of the optics place on the loop gains.

4.2. Length disturbance source model

We modeled the interferometer as being composed of four "pendulums", each representing one of the lengths L_+, L_-, l_+ and l_-. Each of these "pendulums" is excited by the motion at its suspension point by disturbances L_{sp+}, L_{sp-}, l_{sp+} and l_{sp-}, where the subscript *sp* stands for "suspension point", since these are the motion at the pendulums' suspension points. Each of these inputs is the ground noise L_{g+}, L_{g-}, l_{g+} and l_{g-} propagated through the seismic isolation stacks, where the subscript *g* stands for "ground". The lengths L_{g+}, L_{g-}, l_{g+} and l_{g-} are calculated from the ground motion at each mirror position defined in the same way as in Figure 1 in Chapter 2. Figure 7 shows the notation used to propagate the seismic noise for the L_- degree of freedom.

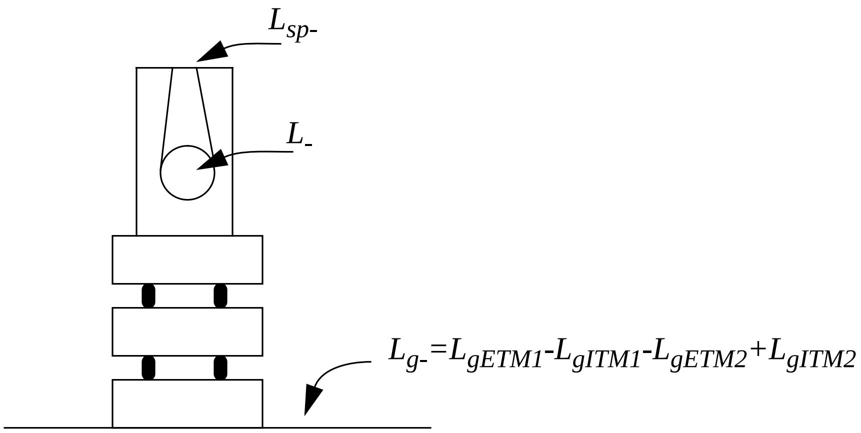

Figure 7: Notation used for seismic noise propagation.

We assume that the ground noise at different points is perfectly correlated. If $Z_g(x, t)$ is the horizontal motion at point x and time t, $Z_g(y, t)$ is the horizontal motion at point y and time t, $Z_g(y, f)$ is the Fourier transform of the $Z_g(y, t)$, and $Z_g(x, f)$ is the Fourier transform of $Z_g(x, t)$, then the spectral correlation function between points x and y is given by

$$S_{xy}(f) = \frac{Z_g(x,f)Z^{\dagger}{}_g(y,f) + Z^{\dagger}{}_g(x,f)Z_g(y,f)}{|Z_g(x,f)Z_g(y,f)|}.$$

If we know $Z_g(x, t)$ (say, for the ground motion at the recylcing mirror position), and we assume a given correlation function $S_{xy}(f)$ and also that $|Z_g(x, f)| = |Z_g(y, f)|$ (assuming the power spectrum at every point is the same), we can then obtain $Z_g(y, t)$ (say, for the ground motion at the beamsplitter position). We first make a Fourier transform of the finite time record $Z_g(x, t)$, obtaining $Z_g(x, f)$, we solve for $Z_g(y, f)$ using the correlation function, and then we Fourier transform back to $Z_g(y, t)$. Notice that the time records will have perfect coherence when correlated in this way.

Measurements at SLAC (reported in LIGO-L960019-00-F) were done to study the correlation between seismometers placed at distances ranging from several meters to 2 km. We borrowed their results, and assumed that $S_{xy}(f) = J_0(2\pi f|x-y|/v(f))$ where $v(f)$ is the ground velocity of the seismic wave at frequency *f*. We also assumed $v(f) = (450 + 1900e^{-f/2\mathrm{Hz}})\mathrm{m/s}$, taken from the same reference. This data is valid from the microseismic peak frequency up to 12 Hz. The seismic measurements at the sites are good up to 30-40 Hz, so using these assumptions for all the frequencies considered does not seem unreasonable.

We have simultaneous ground noise measurements made at a distance of 4 km at the sites. The time traces we have looked at are *not* coherent at most frequencies, unlike what we are assuming here. However, where the coherence is larger than 0.5, the correlation function agrees with our model. Moreover, our assumption used for $|x-y| = 4\mathrm{km}$ results in a slightly larger spectral amplitude for $L_{\mathrm{g-}}$ than the measured one, so our design should also work with the measured $L_{\mathrm{g-}}$ amplitude. We decided to use this correlation model because even though we have good measurements of $L_{\mathrm{g-}}$ and $L_{\mathrm{g+}}$, we don't have the same quality of measurements at the sites for $l_{\mathrm{g+}}$ and $l_{\mathrm{g-}}$, where we expect some degree of common mode rejection which we need to take into account in the loop design.

The specific way in which we generate the 4 "pendulum" seismic excitations is as follows. We first use time traces in both horizontal directions taken at the Louisiana site for a "noisy 0.2 Hz stretch" (as provided by A. Rohay) and propagated them through stack transfer functions, added stack drifts, and acoustic noise coupled through vacuum loading, much in the same way it was done for the ASC (LIGO-T960103-00-D). We used a Simulink model for this, with the block diagram shown in Figure 8. We should mention that the stacks used are the “old” model for leaf spring stacks, with Qs of 30 at their first two resonances, at 1.4 and 3 Hz. (A new model for the stacks transfer functions has been made available by Hytec in July, too late to be considered here. However, the transfer functions used are very similar, with stacks resonances at slightly different frequencies.).

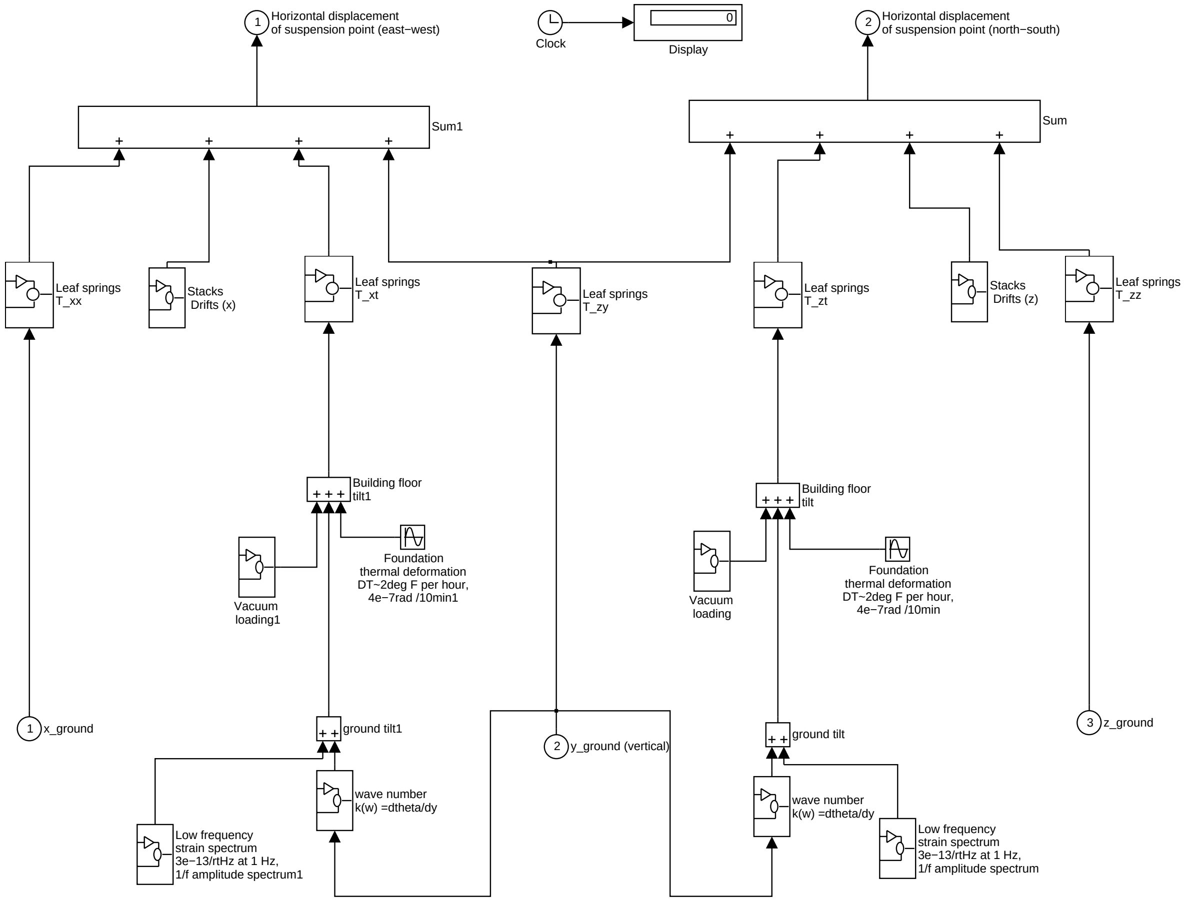

Figure 8: Simulink diagram for the propagation of seismic noise from ground to the pendulum suspension point.

We then assume that the trace obtained represents the excitation of the suspension point of the recycling mirror. Using the mentioned model for the correlations, we obtain the motion in the relevant directions of the beamsplitter, input test masses and end test masses, and then define the disturbances L_{sp+}, L_{sp-}, l_{sp+} and l_{sp-} in the obvious way. The resulting spectra are shown in Figure 9 and Figure 10, where the microseismic peak and the stack resonances are the most prominent features. The rms and peak to peak excursions in each of the five traces obtained, compared with the original ground time trace, are presented in Table 7 .

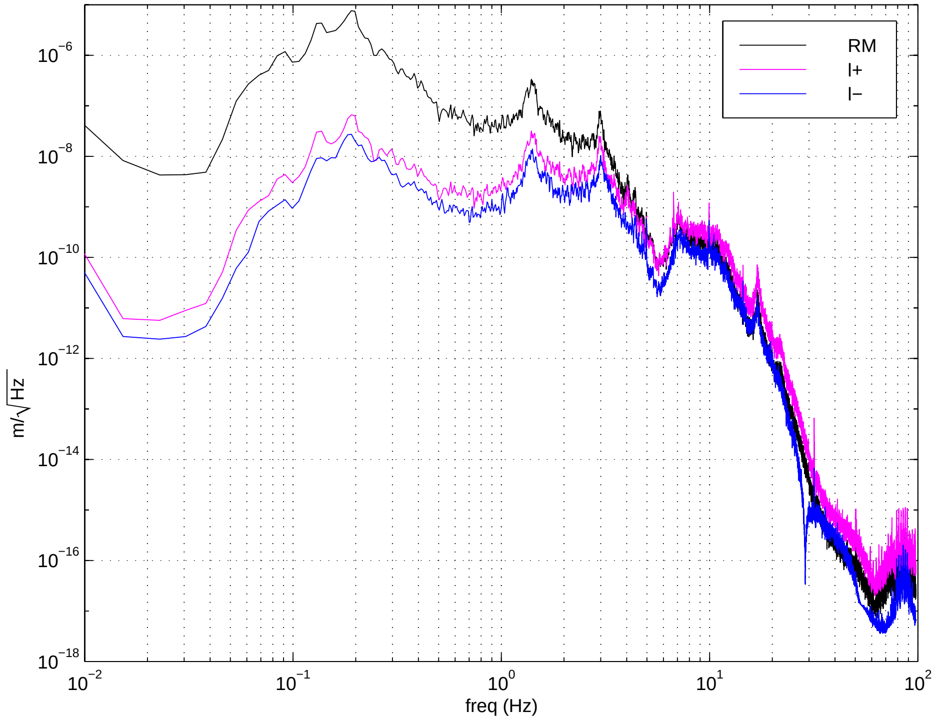

Figure 10: Spectral densities for the pendulum seismic excitations for the recycling mirror, the "l+" and the "l-" pendulums.

	rms	*pk-pk*
Horizontal (E/W) ground trace	1.9 µm	12.4 µm
At RM pendulum suspension point	2.0 µm	12.8 µm
At "L+" pendulum suspension point	3.3 µm	19.7 µm
At "L-" pendulum suspension point	2.9 µm	18.7 µm
At "l+" pendulum suspension point	24 nm	4.3 µm
At "l-" pendulum suspension point	12 nm	0.8 µm

Table 7: The rms and peak-peak excursions in the models used for suspensions point excitation.

4.3. Optical plant model

We use the explicit expressions for the optical plant transfer functions in "Frequency response of the LIGO Interferometer" LIGO-T970084-00-D. We created in Matlab a program that creates a

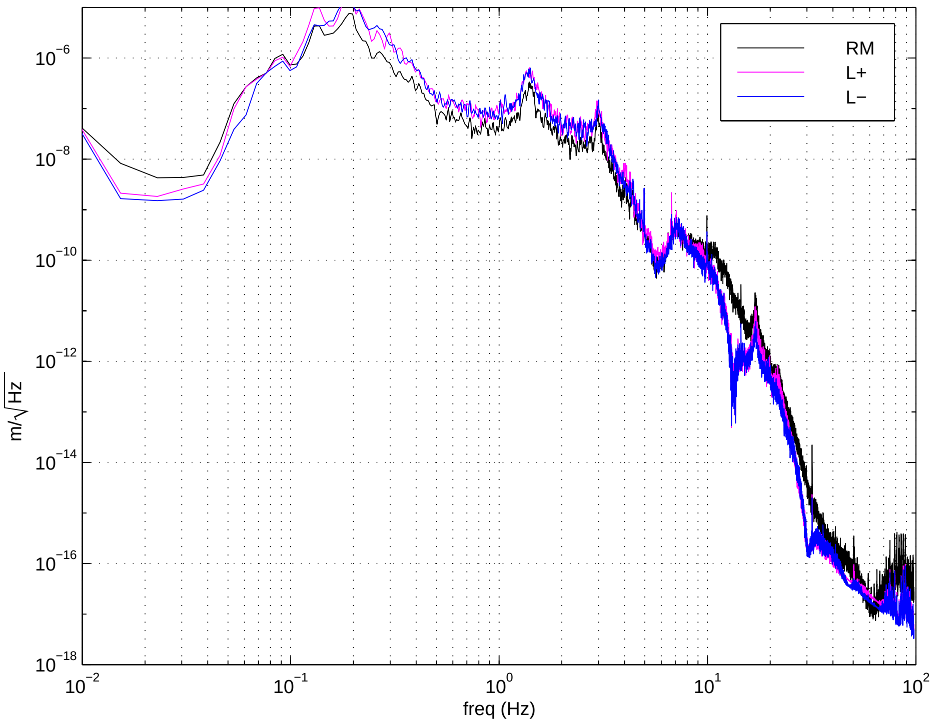

Figure 9: Spectral densities of pendulum seismic excitation for the recycling mirror, and for the "L+" and "L-" pendulums.

MIMO plant with 5 inputs: δL_-, δl_-, δL_+, δl_+, in meters, and laser frequency noise $\delta\nu_l$ in Hz. The plant has four outputs, which are the mixer signals S_{AQ}, S_{PQ}, S_{PI}, S_{RI} in Volts. From LIGO-T970084-00-D, we have the plant outputs in Watts/m or Watts/Hz; we then use a photodiode sensitivity of 0.70 Amp/Watts, a photodiode transimpedance of 81 Ohms (consistent with the 2mm Hamamatsu parameters presented in section 3) and a mixer gain of 0.5, to obtain the plant in Volts/m or Volts/Hz. The optical parameters, interferometer lengths and RF modulation parameters used are those in Table 1 (Section 2.2). The resulting matrix is presented in Table 8 . The poles and zeros appearing in the table are $\omega_c = 2\pi \times 91\,\mathrm{Hz}$ (arm cavity pole), $\omega_{cc} = 2\pi \times 0.77\,\mathrm{Hz}$ (double cavity pole), $\omega_r = 2\pi \times 2.90\,\mathrm{Hz}$ and $\omega_p = 2\pi \times 0.86\,\mathrm{Hz}$.

4.4. Control design & projected performance: differential mode loops

We used a combination of Matlab and Simulink in the loop design, driven by convenience and what seemed to be numerical precision problems in Simulink with time domain simulations. All the modeling has been done in the frequency domain, although the capability exists to create time domain traces in the same way we modeled the seismic excitation.

We broke up the design in two pieces: the differential mode servos and the common mode servos. We assume that the stability properties of the two servo "blocks" are not affected by each other, which is a valid assumption if the drives can be done to the differential and common lengths without cross couplings.

	dS_{AQ}(Volts)	dS_{PQ}(Volts)	dS_{PI}(Volts)	dS_{RI}(Volts)
dL_- (m)	$\frac{-9.6\times10^{11}}{1+s/\omega_c}$	4.72×10^{5}	0	0
dl_- (m)	$\frac{-7.3\times10^{9}}{1+s/\omega_c}$	6.20×10^{7}	0	0
dL_+ (m)	0	0	$\frac{-7.82\times10^{10}}{1+s/\omega_{cc}}$	$\frac{2.85\times10^{12}}{1+s/\omega_{cc}}$
dl_+ (m)	0	0	$\frac{-3.14\times10^{8}(1-s/\omega_p)}{1+s/\omega_{cc}}$	$\frac{-2.95\times10^{10}(1+s/\omega_r)}{1+s/\omega_{cc}}$
$d\nu_l$ (Hz)	$\frac{4.54\times10^{-12}}{1+s/\omega_c}$	0	$-\frac{1.11}{1+s/\omega_{cc}}$	$-\frac{82.8}{1+s/\omega_{cc}}$

Table 8: Interferometer Optical Plant

The block diagram for the differential block is shown in Figure 11. We use the optical plant described in the previous section. The pendulum blocks are pendulum transfer functions, where

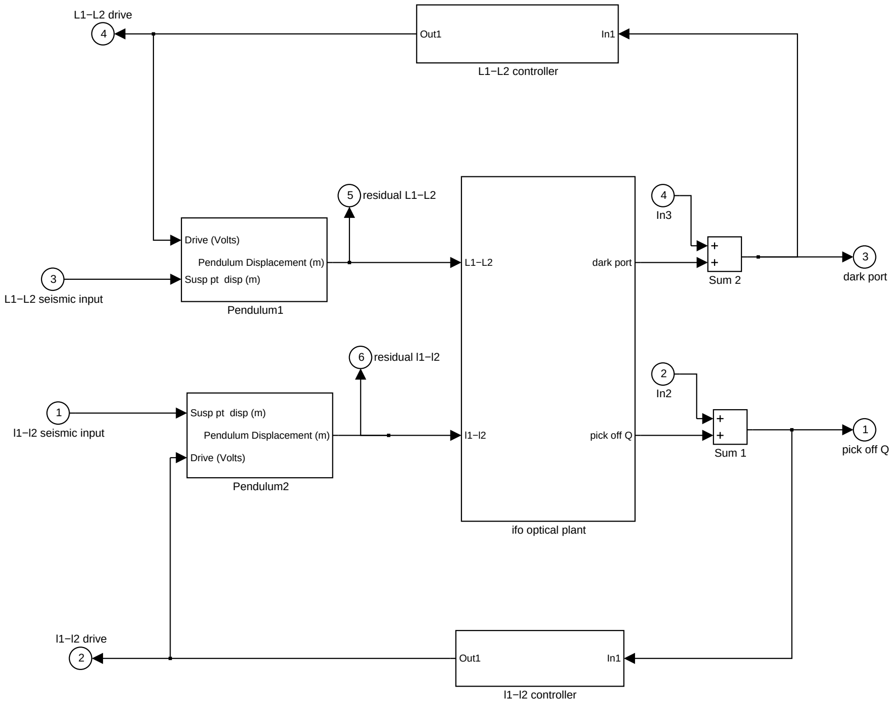

Figure 11: Block diagram for the differential loops.

the seismic input in meters is added to the coil drive in Volts, times the DC gain in meters/Volts, as shown in Figure 12.

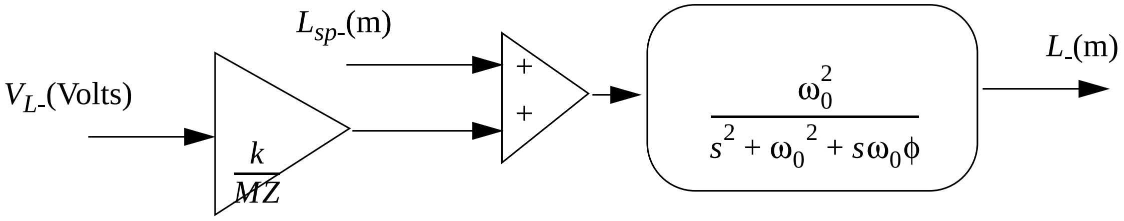

Figure 12: Block diagram of pendulum block (for L_-)

The parameters used in the pendulum block are the pendulum frequency $\omega_0 = 2\pi \times 0.74$ Hz, the inverse of the pendulum quality factor $\phi = 10^{-5}$, the coil-magnet force constant $k = 0.03$ N/Amp, the coil drive impedance (for all four coils in parallel) $Z = 1\mathrm{k}\Omega$ and the mirror mass M=10.7 kg.

The controllers have dimensionless gains in Volts from the mixer to Volts driving the mirror coil series impedance. The block diagrams for the controllers are shown in Figure 13. The Chebyshev filters are used to reduce the gain at the 9.5 kHz mirror resonance. A less aggressive filter could be used in the l_- loop, but we preferred to use the same filter so that we could relocate them downstream to place them within the individual mirror drives (if necessary). We used a Matlab program that calculated the MIMO gain matrix for some range of frequencies and then inverted it to obtain the desired transfer functions. The open loop gains are obtained inverting the closed loop gain as measured in an additive buffer in each path (in2-out1 for l_- loop and in4-out3 for L_- loop in the

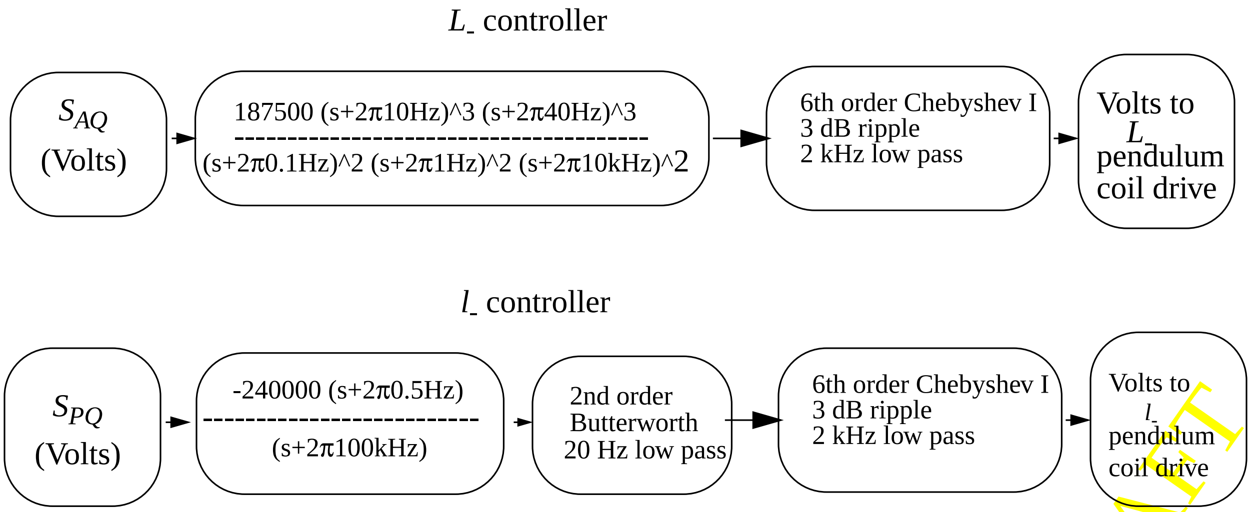

Figure 13: Controllers in the differential loops.

Simulink block diagram), with both loops closed. The vital statistics for the loops are shown in Table 9 .

	L_- loop	l_- loop
unity gain frequency	99 Hz	14 Hz
phase margin	40 deg	26 deg
gain margin	-7dB @ 51 Hz	5 dB @ 19 Hz
gain at 9.5 kHz	4.3×10^{-8}	2.8×10^{-14}
residual rms	$S_{AQ} = 3.4\times10^{-14}\mathrm{m}$	$S_{PQ} = 4.0\times10^{-10}\mathrm{m}$

Table 9: Differential loop gains and residuals.

We assume the shot noise has a white spectral density equal to $11\mathrm{nV}/\sqrt{\mathrm{Hz}}$ added to S_{PQ} and $23\mathrm{nV}/\sqrt{\mathrm{Hz}}$ added to S_{AQ}. These values are equivalent to the ones in LIGO-T960042-00-D, times the photodiode transimpedance of 81 Ohms. We calculate the contribution of the shot noise to the gw signal multiplying the spectral density by the calculated transfer function (with both loops closed) between the corresponding output port and the L_- input to the optical plant, divided by 4km. This value for the shot noise and the assumed plant transfer functions pose the following constraint on the l_- loop gain G_{l-}:

$$\left|\frac{G_{l_-}}{1-G_{l_-}}\right| \le \frac{\mathrm{SRD/10}}{1.69\times10^{-22}/\sqrt{\mathrm{Hz}}}$$

The quantity on the right hand side of the equation is equal to one at ~30 Hz, and it is 0.1 at 47 Hz. This is why the l_- loop has such a low bandwidth (14 Hz) and small phase margin (because of the filter at 20 Hz). However, with the assumed inputs for the seismic inputs, this loop satisfies all requirements. We may want to lock the interferometer with a higher bandwidth loop, and then with the actual information on hand about shot noise and seismic excitation, reduce the gain and add the filters to satisfy the signal to noise requirements.

Figure 14 presents the shot noise contributions to the gravitational wave signal. For reference, we also plot the contribution of seismic noise as modeled for this document, the SRD curve and the SRD/10 curve.

Bode plots for the loops are shown in Figure 15 and Figure 16. We also show in Figure 17 and Figure 18 the contributions of the different seismic inputs to the signals at the dark port and at the recycling cavity pick off (the lower spectrum is the off-diagonal contributions, the smooth curves are integrated rms amplitudes).

Another point of concern in the design is dynamic range considerations. We show in Figure 20 the spectral densities of the signals at the ports, in Volts: these are the inputs to the digital controllers that then determine their noise requirements. We show in Figure 19 the output of the controllers in

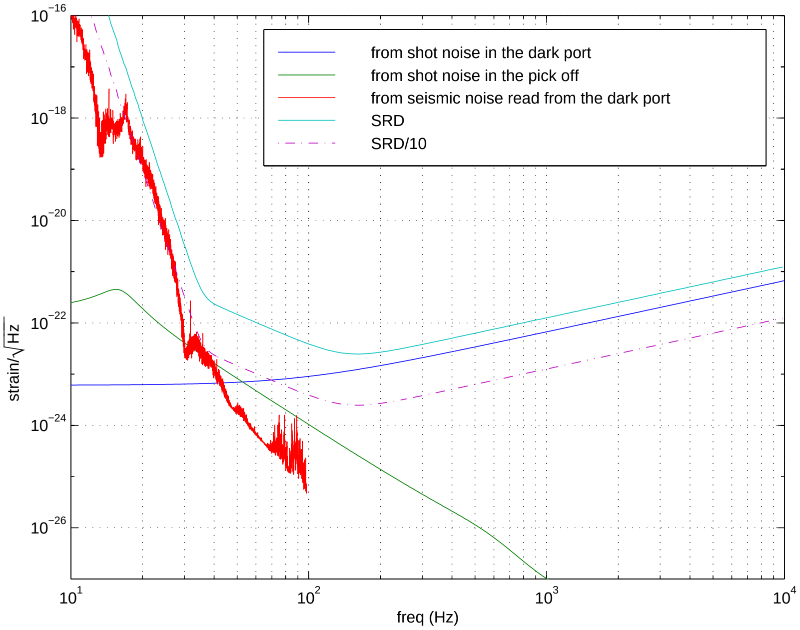

Figure 14: contributions from the differential loops to the gravitational wave signal.

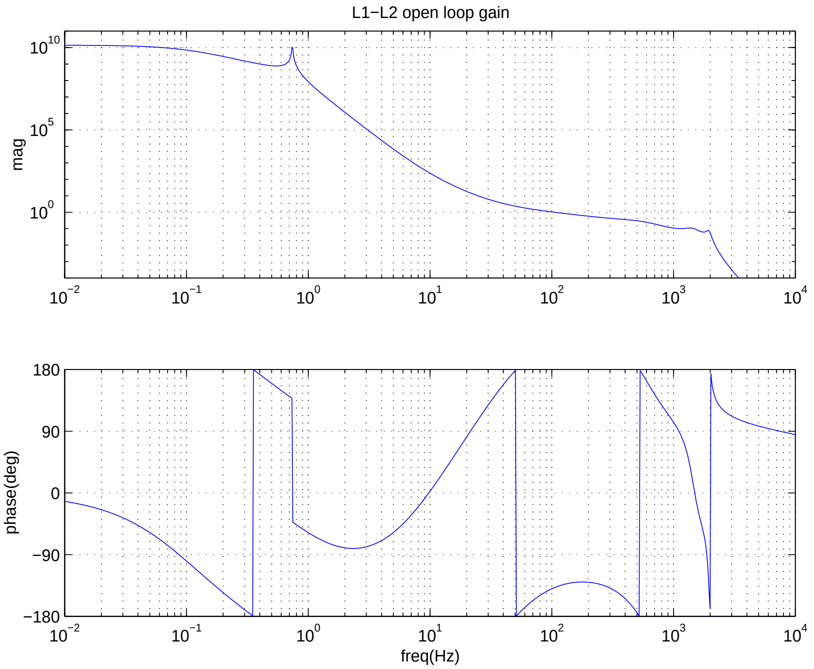

Figure 15: Open loop gain for L_- loop.

Amps (current in the coil drivers): this what is then required from the SUS controllers and the driver electronic stage.

Limitations to achieving $L\_ = 10^{-13}$ m. The residual deviation requirement of **$L\_ = 10^{-13}$ m** (in fact the simulation achieves a value 3 times smaller), is smaller than has been typically achieved

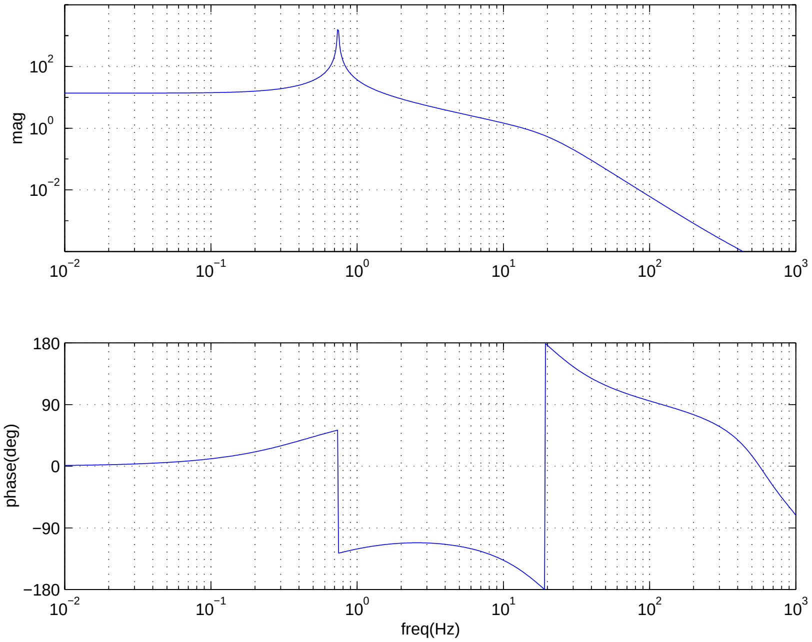

Figure 16: Open loop gain for l_- loop.

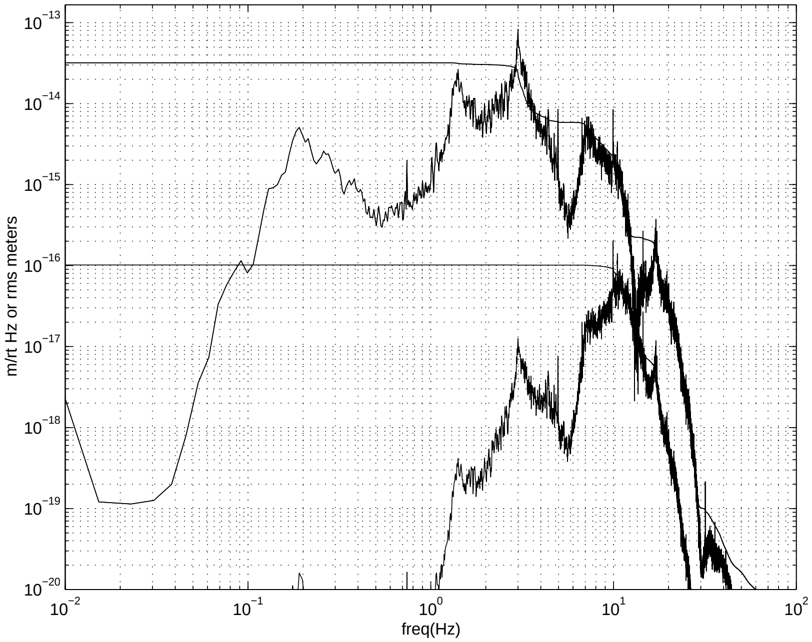

Figure 17: Residual S_{AQ} in L_- meters.

with the prototypes (10^{-11} – 10^{-12} m is achieved in the 40m). The simulations show that the loop gain is sufficient to achieve this level, but it is worth considering some sources of offsets that in practice could lead to a false zero in the error signal (they could be compensated for if they are stable, but it is preferable that they be insignificant to begin with).

- **RF pickup in the detectors.** Because of the very large optical gain in the system, this

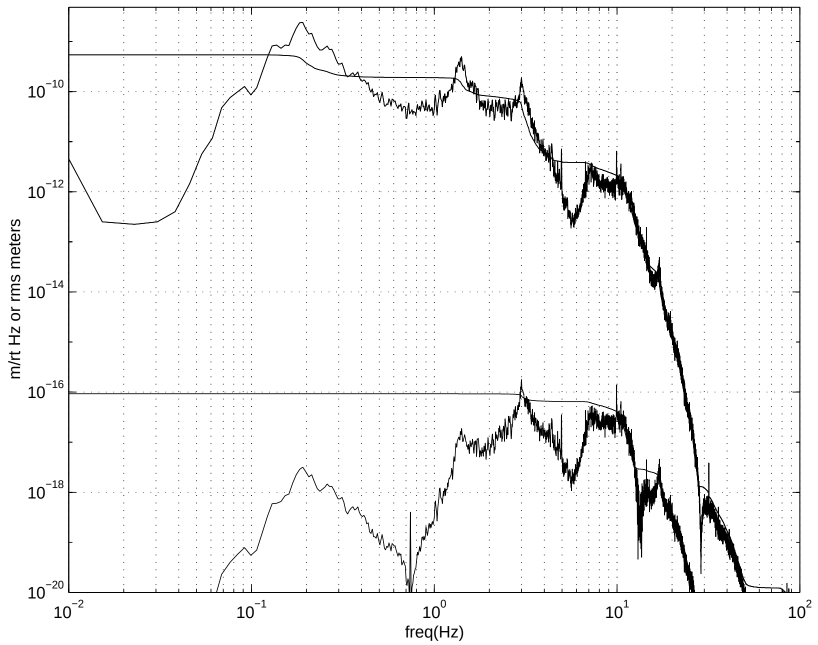

Figure 18: Residual S_{PQ} in l_- meters.

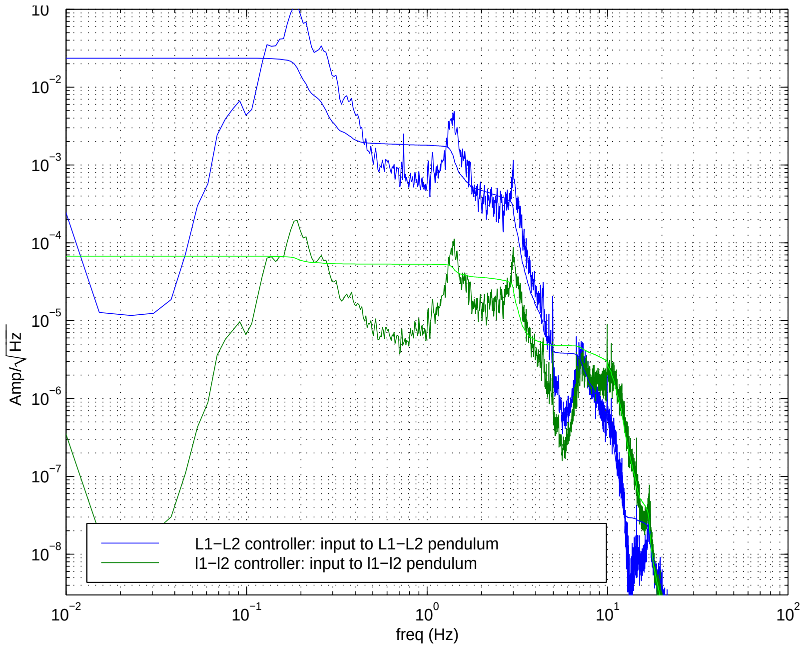

Figure 19: Output of the controllers in the differential mode loops.

should not be a problem. The sensitivity at the anti-symmetric port in RF photocurrent is 2.5×10^{10} A/m. The residual length of 10^{-13} m then produces an RF current of 2.5 mA_{rms}. RF-pickup in the sensors is expected to remain below the μA level, so RFI-induced offsets will be completely negligible.

- **Voltage offsets.** Assuming four photodetectors at the anti-symmetric port that are inde-

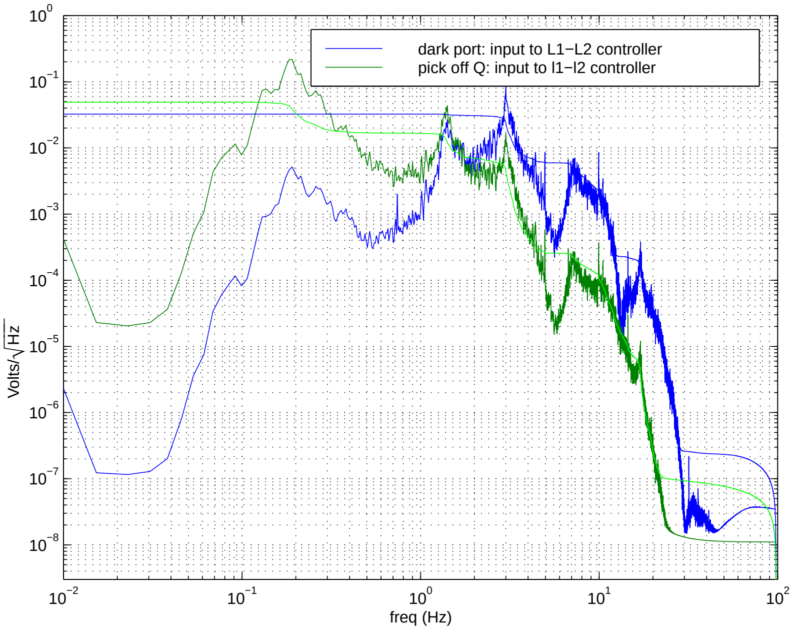

Figure 20: Input to the controllers in the differential mode loops.

pendently demodulated, the rms voltage at the output of each demodulator due to a deviation of 10^{-13} m is 25 mV_{rms} (assuming no additional RF gain; an additional RF gain of 5-10 will probably be included, increasing this voltage by that factor). Demodulator and preamp voltage offsets can typically be controlled to the ~1 mV level or better, thus this source of offset should be insignificant.

- **Residual amplitude modulation on the light.** The phase modulator will produce also some level of amplitude modulation of the light. This can produce a DC signal at the anti-symmetric port in the presence of a carrier TEM_{00} contrast defect. From LIGO-T97--84-00-D, the ratio of the signal produced by this AM to the signal produced by an arm length difference is:

$$\frac{\left(\frac{\Delta A}{A}\right)\delta r_c}{4 J_0(\Gamma) J_1(\Gamma) r_c' k \, \delta L_-}$$

where ($\Delta A/A$) is the fractional field amplitude modulation, δr_c is the imbalance in the arm cavities reflectivity (the cause of the contrast defect), r_c' (=130) is the derivative of the arm cavity reflectivity w.r.t. the round trip phase, and $k = 2\pi/\lambda$. We have previously an upper limit on the imbalance of $\delta r_c = 0.5\%$. A residual *intensity* modulation ($2\Delta A/A$) of 0.5% would then produce a signal equal in amplitude to that produced by $\delta L_- = 10^{-13}$ m. If we require a residual intensity modulation of 10^{-3}, this offset will be small enough.

4.4.1. Control design & projected performance: common mode loops

The Simulink block diagram for the common mode loops is shown in Figure 21. The system has three inputs: seismic inputs for the L_+ and l_+ pendulums, and frequency noise input. We assume the frequency noise input is given by the required frequency noise level at the output of the IOO; this level is given in the SYS DRD to be $v_{IOO}(f) = 10^{-4}\sqrt{100\mathrm{Hz}/f}\ \mathrm{Hz}/\sqrt{\mathrm{Hz}}$ above 100 Hz.

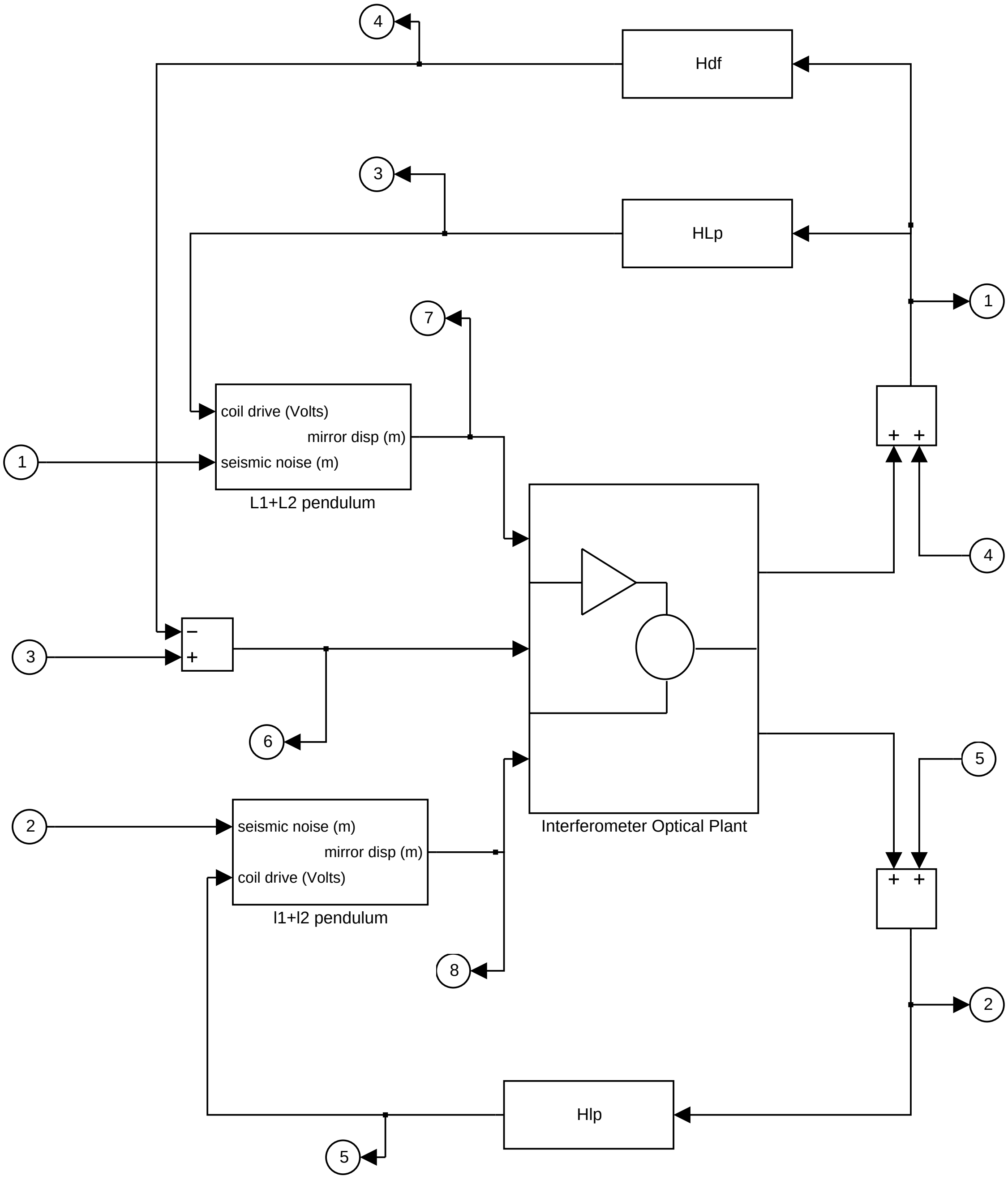

Figure 21: Simulink block diagram for the common mode loops.

Both signals, S_{RI} and S_{PI} are mostly sensitive to the arm cavities' phase noise. We take the signal from the reflected port and send it both to the L_+ pendulum at low frequencies and to the laser at high frequencies. We assume for this model that the laser frequency path acts on an ideal actuator, i.e., that the laser frequency perfectly follows this control signal. The actual laser frequency control signal will act on both the mode cleaner length and on the mode cleaner servo's additive offset input. The signal division and crossover design for these specific control paths will be done in the final design phase.

The trade off between the gains in the test mass and laser frequency paths is given by two competing requirements. On the one hand, the mirrors must follow the laser at low frequencies to reduce the rms phase noise in the arm cavities. Since the signal at both ports is also proportional to the phase noise in the recycling cavity, we cannot use those signals to drive the laser and reduce the rms in the arm cavities by more than the ratio between the ports' sensitivity to arm cavities phase and recycling cavity phase noise, or about ~130. This is not enough: to satisfy the requirement of <10 μrad rms, we need gains of $\sim 10^5$ at frequencies near the stack resonances (~3 Hz). Thus, we need to drive the L_+ pendulum with high gain to reduce the rms phase noise in the arm cavities.

On the other hand, we need to reduce the frequency noise so that it doesn't contribute more than 1/10 the SRD at the dark port. To achieve this, we make the laser follow the average length of the arm cavities, which is a more stable reference than the mode cleaner for frequencies greater than ~10-20 Hz. At 40 Hz, the requirement on the frequency noise is $10^{-6}\mathrm{Hz}/\sqrt{\mathrm{Hz}}$ and the IOO frequency noise is $\sim 6\times 10^{-4}\mathrm{Hz}/\sqrt{\mathrm{Hz}}$: so we need a gain ratio of 600 at 40 Hz to satisfy this requirement. This trade off has been solved using controllers so that the open loop gains cross at ~20 Hz, and then using a low pass filter in the mirror controller and a high pass filter in the laser controller. This makes the range for the gains ratio very narrow, which we may not be want to do before knowing better. So, again as in the differential mode, there is a design that satisfies the requirements given the modeled inputs and optical plant, but we may want to lock the interferometer without the filters (and thus having a somewhat larger RFAM and frequency noise coupling than required), and then switch on the filters at a later stage.

The controllers are shown in Figure 22. The loops' data are found in Table 10 .

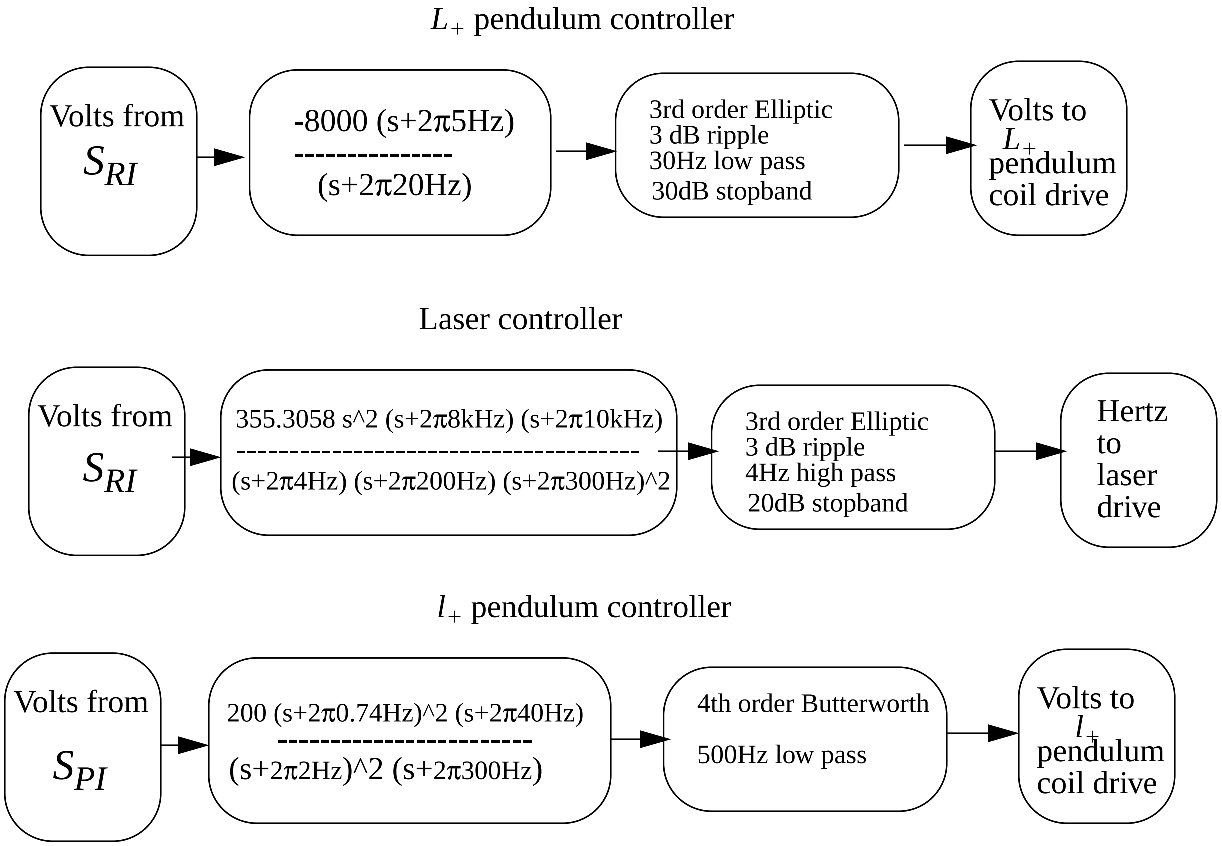

Figure 22: controllers in the common mode loops.

	L_+ /laser loop	l_+ loop
unity gain frequency	26 kHz	47 Hz
phase margin	53 deg	30 deg
gain margin	-16dB @ 8 kHz	14 dB @ 161 Hz
gain at 9.5 kHz	2.8×10^{-7}	7.0×10^{-10}
residual rms phase noise	$\Phi_+ = 3.2\times10^{-6}$rad	$\phi_+ = 1.5\times10^{-4}$rad

Table 10: Common mode loop gains and residuals.

The open loop gains were calculated using the Simulink linear model of the block diagram, with all the loops closed, and calculating Bode functions between input and outputs of buffers in each path for the closed loop gains. The Bode plots are shown in Figure 23 and Figure 24. The residual

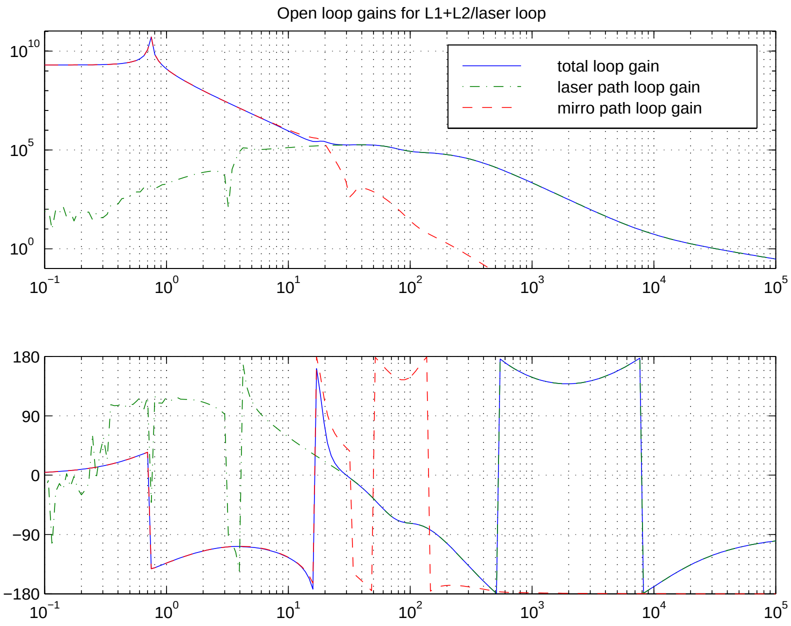

Figure 23: Open loop gains for the arm common mode and laser frequency control paths.

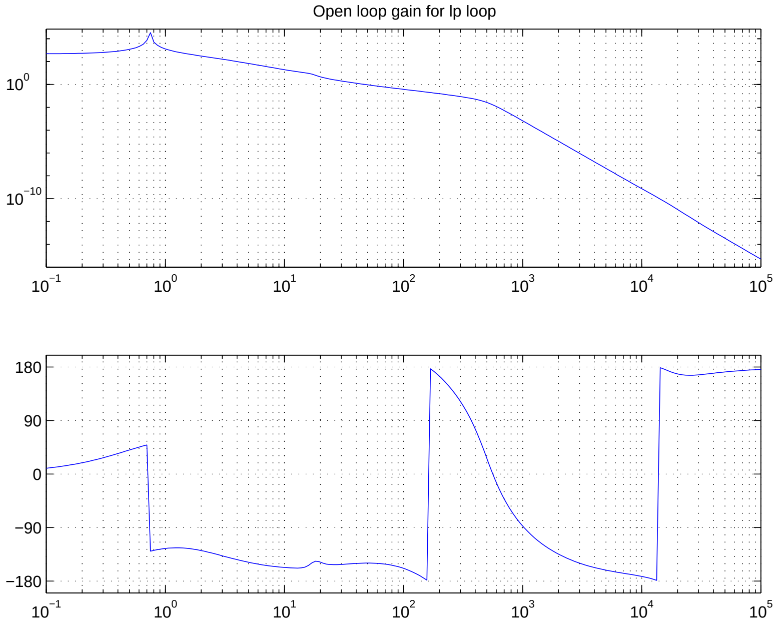

Figure 24: Open loop gain for the recycling cavity length control path.

phase noise in the arms cavities is shown in Figure 25 and the residual phase noise in the recycling cavity is shown in Figure 26. The residual frequency noise, compared with its requirement and the different contributions to it, is shown in Figure 27. Notice that the shot noise at S_{PI} is the main contributor to the residual frequency noise in the critical frequency band between 60 Hz and

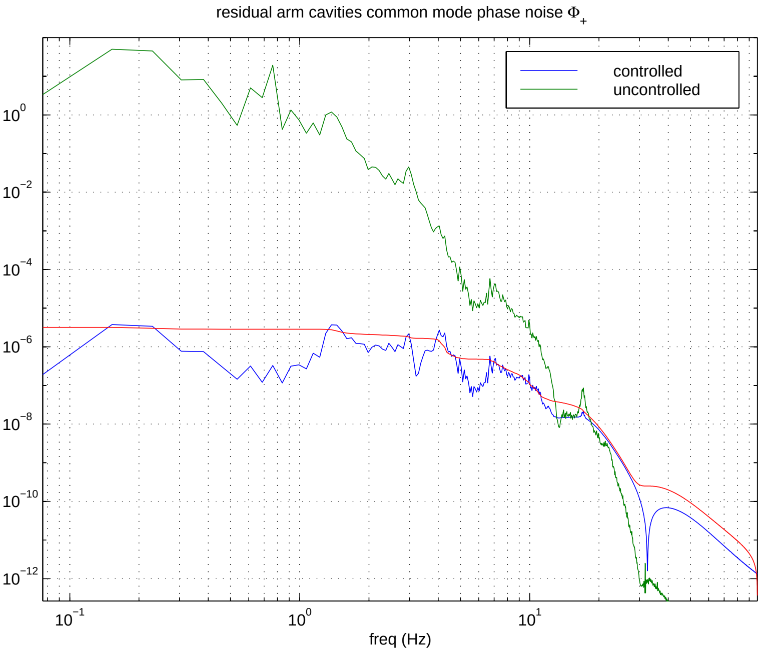

Figure 25: Residual deviation in the arm common mode phase. The requirement is that this must be lower than 9×10^{-6} rad.

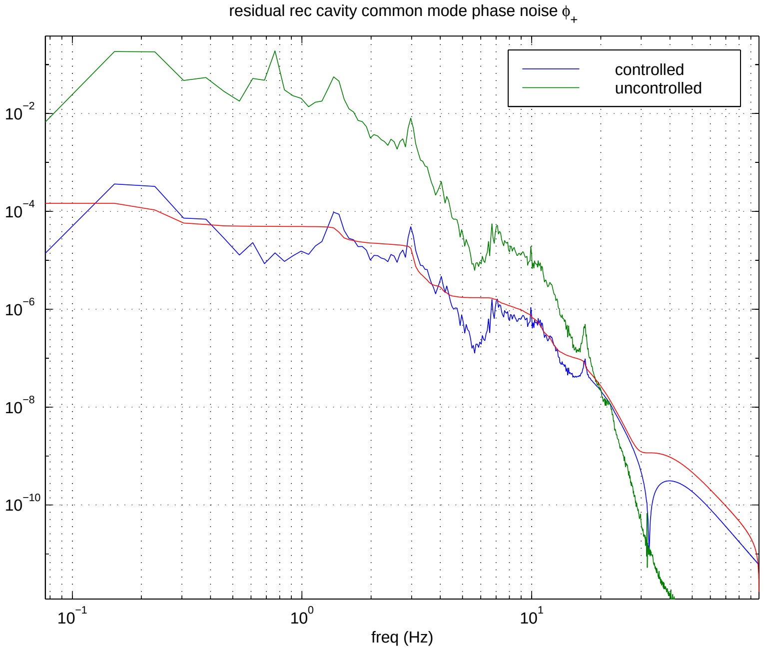

Figure 26: Residual deviation in the recycling cavity phase. The requirement is that this must be lower than 7×10^{-4} rad.

300 Hz (when the requirement is very strict); this limits the gain in the l_+ loop at those frequencies.

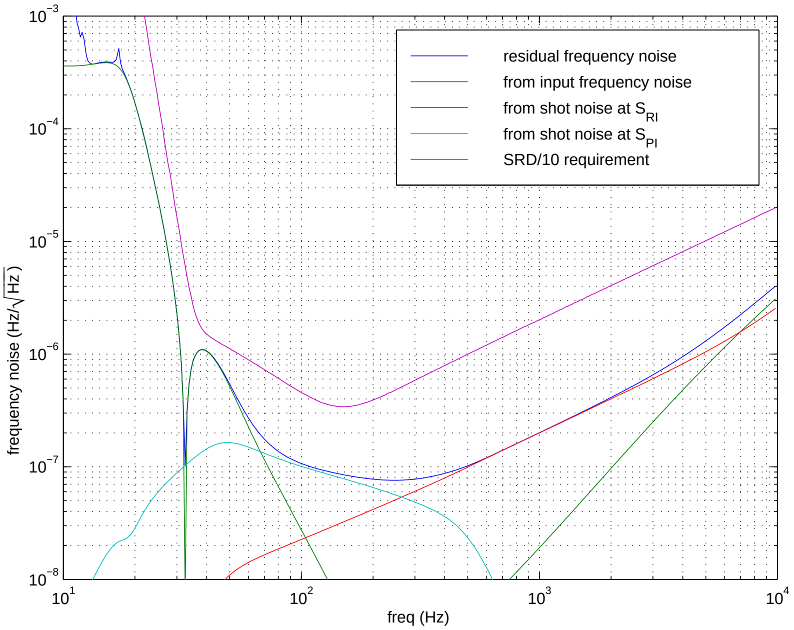

Figure 27: Residual frequency noise.

The signals at both ports are shown in Figure 28 and Figure 29. Finally, the spectral density and rms amplitude of the frequency correction that is applied to the laser with the laser controller, in Hz, is shown in Figure 30.

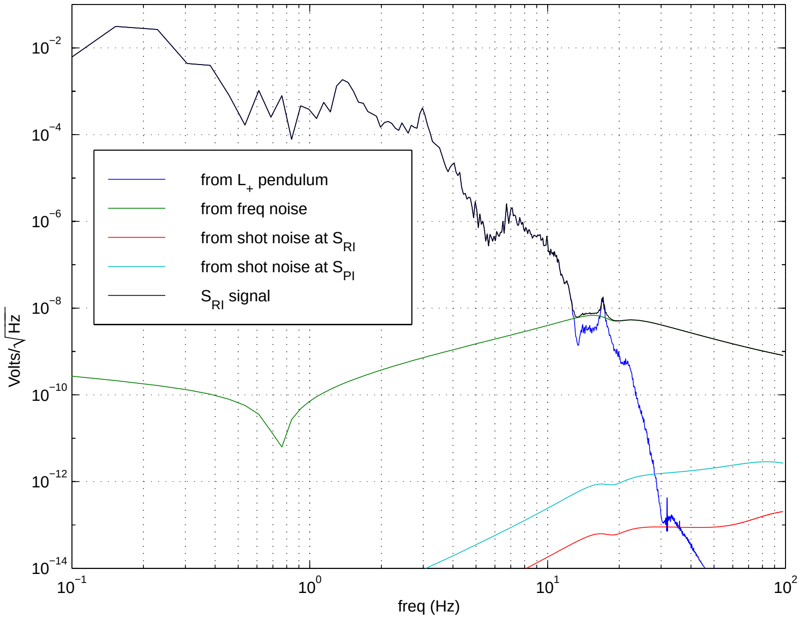

Figure 28: Signal in Volts at the reflected port S_{RI}.

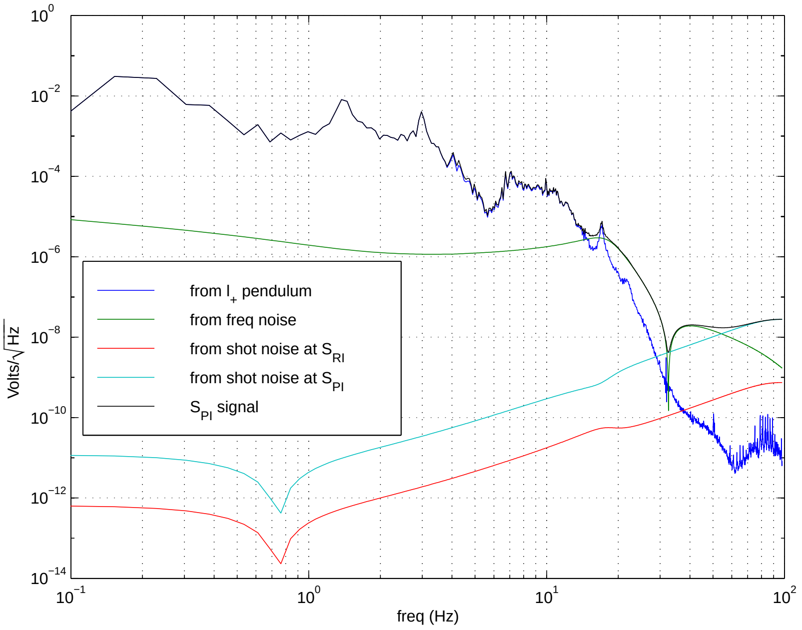

Figure 29: Signal in Volts at the pick off port S_{PI}.

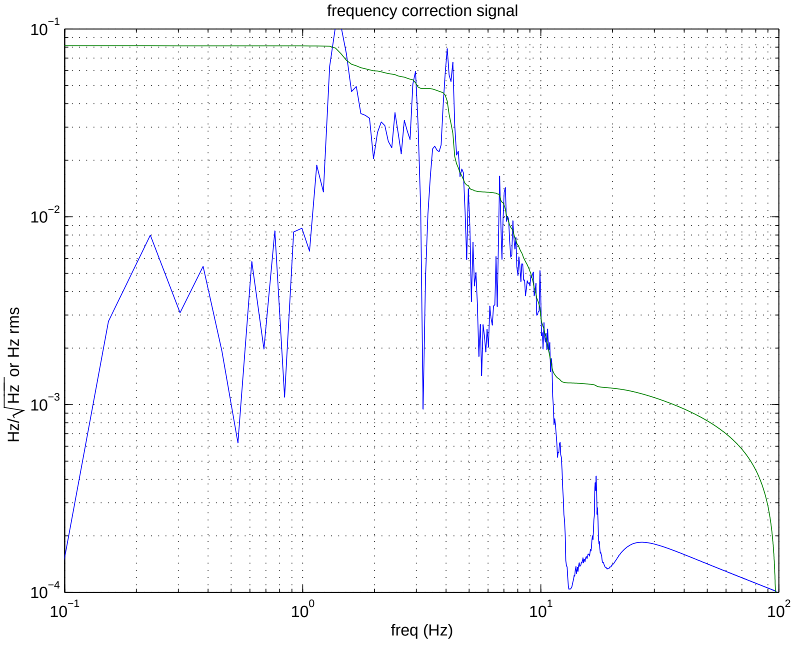

Figure 30: Frequency correction applied by the common mode loop.

4.5. Design work ahead

The following aspects of the servo design will be investigated during the final design phase.

- **Michelson servo.** Though the Michelson servo presented here has an uncomfortably low bandwidth (14 Hz), it does meet the requirements for residual deviation and noise. However it is possible that the length disturbance model for this d.o.f. is overly optimistic, or that for some other reason it will be necessary to increase the bandwidth of this loop. In any case, we would like to be able to increase the bandwidth of this loop without introducing noise into the gravity wave channel. The additional feedback path to the end test masses would allow us to do this. We will investigate how much can be gained by incorporating this path into the model.

- **Test Mass crossovers.** For the Michelson and recycling cavity loops, the split feedback paths between the test masses (at low frequency) and the beamsplitter and recycling mirror (at high frequency) will be included in the model. The crossovers must be designed to have very small loop gain in the test mass paths at frequencies above 40 Hz. The crossovers are expected to be similar to the arm common/laser frequency crossover presented here, and we don't anticipate any difficulties with the design.
- **Mirror resonances.** The limitations to servo bandwidth imposed by the internal resonances of the optics will be further investigated. We expect that taking account of the true transfer function between actuator drive and optical phase response (which must always be smaller than the upper limit assumed in this design), combined with unconditional phase stabilization of certain resonances and the use of tuned notch filters, will relieve high frequency gain constraints imposed here by at least two orders of magnitude.
- **Phase margins.** While all of the current loop designs are stable, most of them have phase margins that are smaller than desirable (as small as 26° for the l_- loop). In practice there will be additional phase shifts due to time delays not included in the current model. In addition, with such small phase margins, small changes in the gain result in large changes in the loop response near the unity gain frequency. The final design will iterate the current loop shapes in order to increase the phase margins, taking the requirement of achieving at least 45° of phase margin for all loops. In order to do this we will have to incorporate the additional feedback path for the Michelson servo, and to treat the mirror resonances in a more sophisticated way as mentioned above.
- **Laser frequency control.** The controller design for the laser frequency path will incorporate the real actuators that will be used – the mode cleaner length control input and the MC servo additive offset.

4.6. Summary

We have shown a preliminary design for the control of the interferometer four degrees of freedoms. The design satisfies all requirements, although we need to tailor the loop gains mostly due to the SRD-to-noise requirements in the gw signal. These requirements are achieved with modular filters in the loop gains in most cases and low gains in other loops. We may find necessary an intermediate step between acquisition mode and detection mode where we check on actual signal levels and noise performance, and then switch on the filters and lower gains as necessary to tune the noise spectrum in the gw band.

We have used a simplified model for the mechanical plant of the interferometer. This should be a good model provided we can make “pure” drives (this being limited by imbalances in the mirror drives), and provided we have identical stacks. These conditions are not strictly true, but we do not anticipate qualitative changes when taking them into account, as we will soon do.

5. LOCK ACQUISITION

5.1. Acquisition Mode Overview

Acquisition mode refers to the state in which the interferometer cavity lengths transition from an uncontrolled state to a state where the cavity lengths are controlled with a high degree of precision. The fundamental requirement driving the design of this control system is the time it takes to acquire lock.

A design approach taken in choosing the servo feedback configuration and design was to make it as similar as possible to the Detection Mode servo system with the hopes of simplifying the overall control topology. Some deviations from this philosophy were required, however; these are highlighted in 5.6. below.

5.2. Servo Configuration

Figure 31 and Figure 32 show the servo configurations for the Common Mode and the Differential Mode feedback paths, respectively. The differences in the servo configuration between Detection Mode and Acquisition Mode are discussed below.

Figure 31: Acquisition mode feedback configuration for common mode lengths (*L*+ and *l*+)

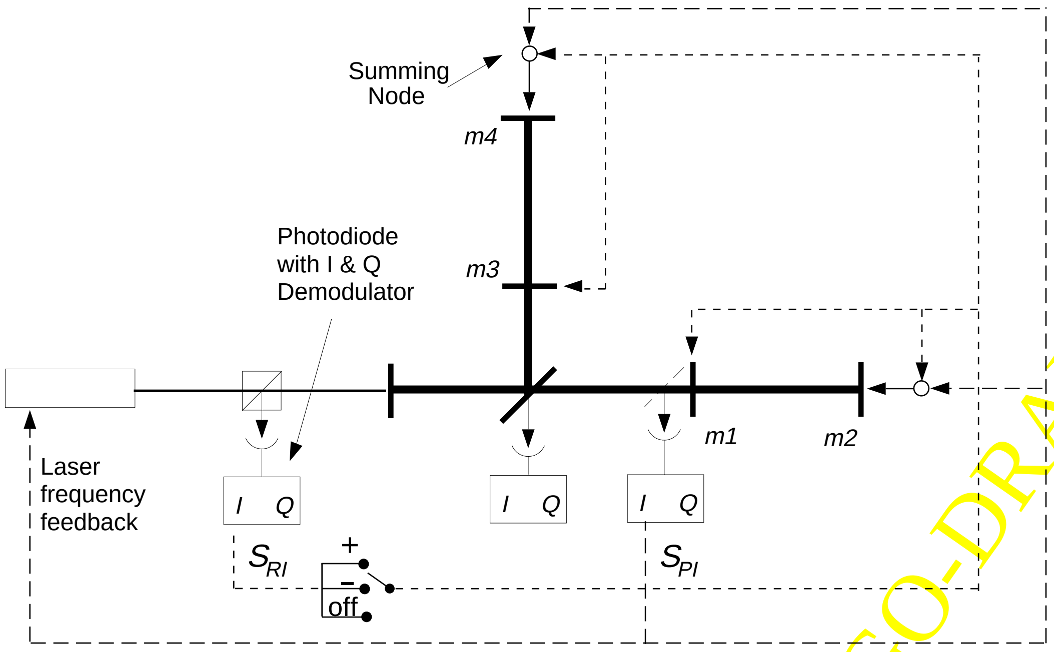

Figure 32: Acquisition mode feedback configuration for differential mode lengths (*L*- and *l*-)

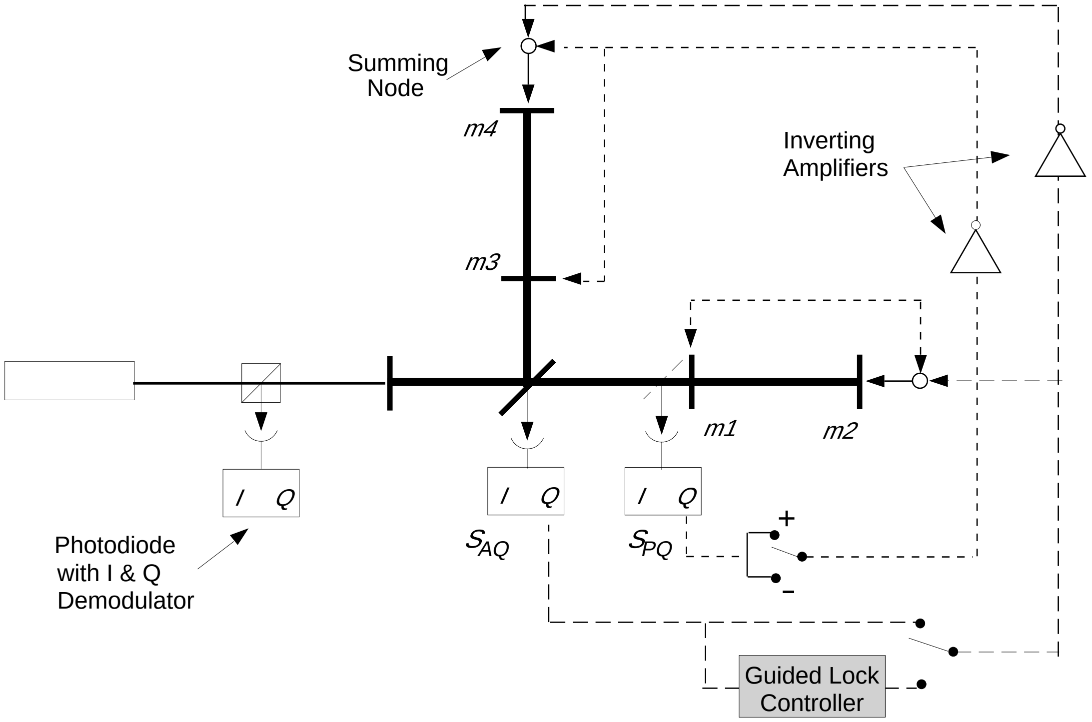

In Detection Mode it is necessary to feed back the S_{RI} signal to the laser (i.e high bandwidth $L+$ actuator) in order to meet signal to noise requirements in the Gravity Wave signal, but the interferometer can't acquire lock due to an instability in the acquisition process for this configuration. Consequently the roles of the S_{RI} and S_{PI} loops are swapped when the interferometer goes from Acquisition Mode to Detection Mode.

During the Acquisition process, the stable feedback signs of the S_{RI} and S_{PQ} loops change as the interferometer transitions from the unlocked state to the state where all the cavity lengths are controlled. This necessitates polarity switches in both of these loops that are triggered during the Acquisition process; no switching occurs during Detection Mode.

The remaining difference between servo configurations is that during Acquisition, a nonlinear controller is switched in and out of the S_{AQ} loop. The function of the Guided Lock controller is to increase the speed of acquiring the *L*- degree of freedom; it does this by interpreting the complex transient signals appearing as the mirrors traverse resonant conditions, deconvolving a best fit to the individual mirror velocities from this, and applying damping forces to each mirror to reduce its velocity below the acquisition threshold.

5.3. Acquisition Sequencing

On starting up, there is in general no information about the individual mirror positions with respect to the desired resonant operating state. It is therefore necessary to lock subsets of the interferometer in a sequential fashion, one after another. The order in which the cavities lock is dependent on the servo configuration chosen. As the sequencing occurs, optical gains and phases of the servo loops change due to the build-up of circulating power in various portions of the interferometer. Although it would be preferable to arrange a control design in which a single set of controllers remains stable, independent of the state of the interferometer, the sensitivity of optical plant transfer functions to the balance of circulating power in different subcavities forces us to adapt the controller as the sequence progresses.

Figure 33: Stable Locking Sequence

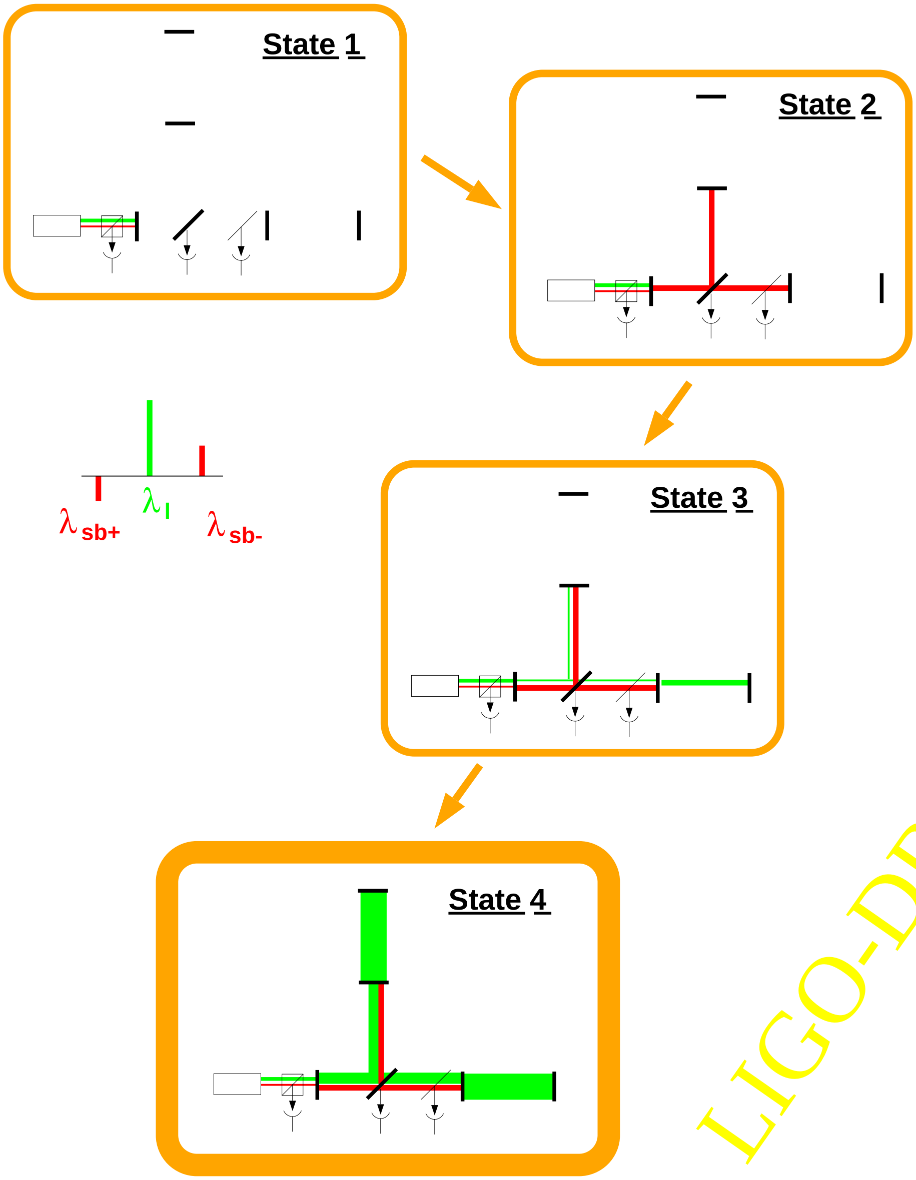

Figure 33 shows the locking sequence that we have developed for LIGO, and defines intermediate stable states in which partial resonance conditions apply. Briefly, we define State 1 as the state in which all interferometer lengths are uncontrolled. In State 2, both sidebands lock in the power recycled Michelson, thus putting both the $l+$ and $l-$ degrees of freedom under control. The carrier starts resonating in one of the arms and simultaneously builds up in the power recycled Michelson in State 3, thus putting the $L+$ degree of freedom under control; in this State, the anti-symmetric (‘dark’) port for normal operation becomes the bright port for the carrier. In State 4, the carrier becomes resonant in the entire interferometer so all degrees of freedom are now under control. The anti-symmetric port of the beam splitter turns into the dark port as the interferometer transitions into State 4.

With this sequence it is possible to design a single set of servos that is stable in each state, given that there is a polarity switch on the S_{RI} and S_{PQ} loops that trigger when the interferometer transitions between State 3 and State 4. This will be discussed in more detail in Section 5.5..

5.4. Pseudo-States of the Interferometer During Acquisition

The carrier and upper and lower resonant sidebands injected into the interferometer are not constrained to resonate only in the states shown in Figure 33. As the mirrors translate during the acquisition process the lengths of the cavities also go through “pseudo-states”. These are unstable states characterized by one of the sidebands accidentally resonating in an arm cavity. The two possible pseudo-states, State 2sb and State 3sb, are shown in Figure 34. Closed-loop simulations using the 40 m interferometer parameters have shown that the pseudo- states do not disturb the locking process in this case. Unfortunately, a set of closed loop simulations using LIGO-like parameters showed that when the interferometer goes through a pseudo-state, the $l+$ loop is kicked out of lock. The differences in the way the pseudo-states behave are not understood completely, and this issue is a high priority for the final design phase. If accidental transition through pseudo-states is indeed found to cause the locking sequence to abort on a significant fraction of attempts, and if the resulting “time to acquire” is deemed excessive, it may be necessary to detect the onset of sideband resonance (using triggers based on the main RF and cavity transmission photodetectors) and temporarily disable or modify the control characteristic.

Figure 34: Pseudo-States 2sb and 3sb During Acquisition

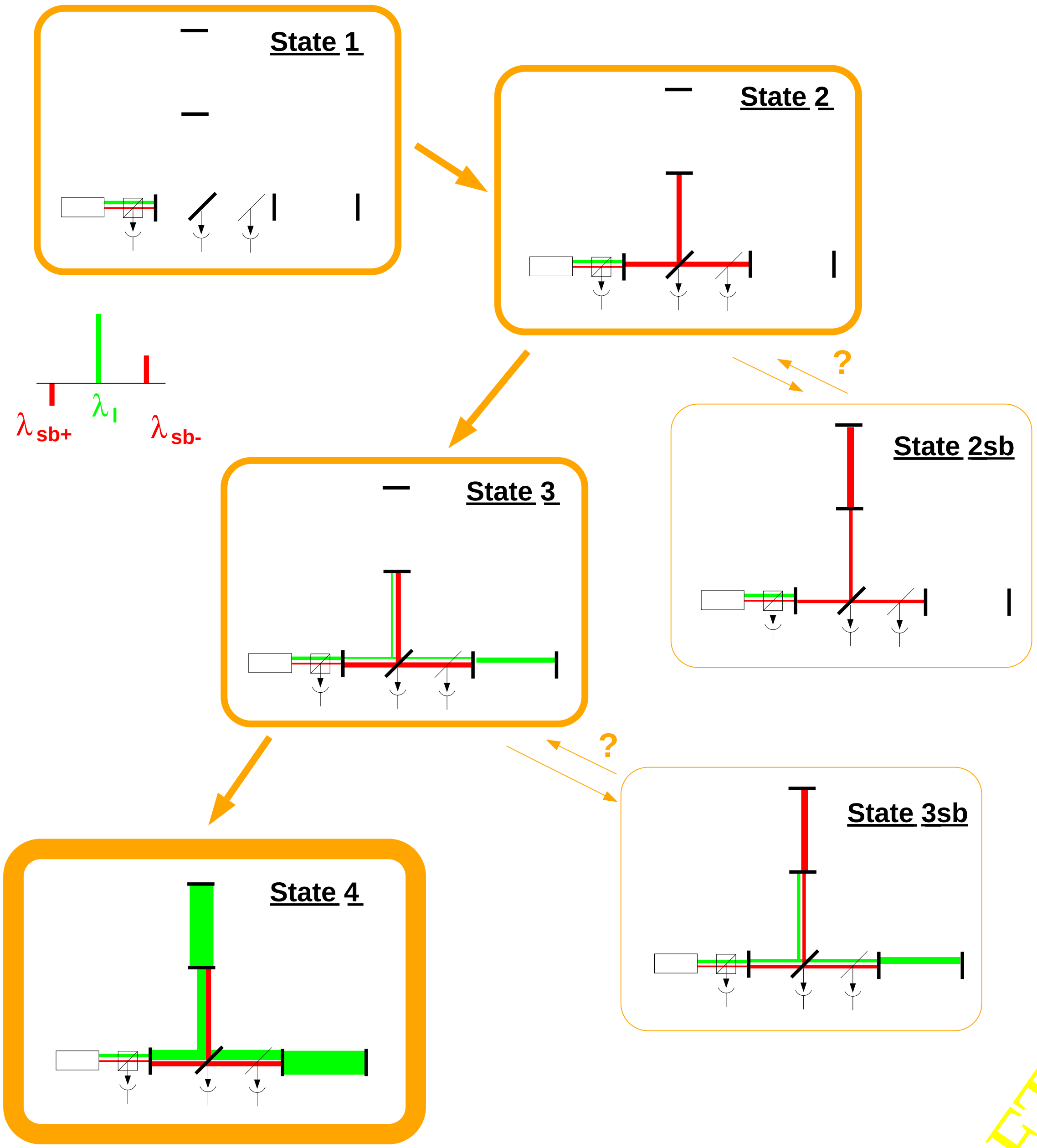

5.5. Control design strategy

5.5.1. Constraints on Loop Shapes

One major design constraint on the loop gain of the detection mode cavity length servos (i.e. *l*+, *l*-, and *L*-) is that the gain in each of the loops must be less than 10^{-6} at 9.4 kHz in any of the stable states and, in the *l*- loop, less than 10^{-6} at 5.3 kHz. This constraint may also apply during acquisition, although weak violation can probably be tolerated for brief transient periods.

5.5.2. Loop Shape Design

The general philosophy for the loop shape design is to maximize bandwidth in order to increase the threshold velocity at which each of the loops will lock. The threshold velocity is the maximum velocity an interferometer optic can experience as it goes through a fringe and still acquire. The threshold velocity effect was observed and model-validated in experimental tests on a single Fabry-Perot cavity in the 40 m. Maximizing low frequency gain is much less important than maximizing bandwidth to the acquisition process. A procedure developed for designing the loop shapes for Acquisition Mode is outlined in Table 11 .

Table 11: Steps For Designing Acquisition Servo System

Step 1	State 4 optical transfer functions are generated for the *L*+, *L*-, *l*+, and *l*- loops using either Twiddle[a] or SMAC[b].
Step 2	Stable servos for all loops are designed using above optical transfer functions. The starting point for the design of each servo is its Detection Mode equivalent. The Detection Mode servos are modified so as to be unconditionally stable and the bandwidths may be increased to maximize the threshold velocity effect.
Step 3	State 3 optical transfer functions are generated for the *L*+, *l*+, and *l*- loops using either Twiddle or SMAC.
Step 4	The optical transfer function of the *L*+ loop in State 3 is very different than the one generated for State 4. The DC gain is reduced significantly and the general loop shape has changed. The initial State 4 servo design is iterated to develop an L+ servo that is both stable in State 3 and State 4. A similar procedure is used for iterating the designs of the *l*+ and *l*- loops. The bandwidths of the *l*+ and *l*- loops are limited to 150 Hz.
NOTE: State 2 optical transfer functions for the *l*+ and *l*- loops are essentially the same as in State 3, thus no redesign of these loops is necessary to insure stability. In State 2 the optical gains for the *l*+ and *l*- loops are much higher than for the equivalent State 4 loops. From a design standpoint, this natural gain difference works to our advantage. The higher bandwidth of the State 2 servos result in higher threshold velocities at the time when the *l*+ and *l*- loops are acquiring, while in State 4 the low gains help reduce sensor noise.	

The *L*+ servo is designed with a much higher bandwidth than the *l*+ servo, in order to diagonalize the two degrees of freedom. Given the *L*+ loop has high enough bandwidth, successful loop shape can be achieved by assuming that the 4 degrees of freedom are completely uncoupled. The uncoupled assumption can then be verified when the servos are tested in closed loop simulation.

---

[a] Interferometer steady-state transfer function code developed by M. Regehr and extended by H. Yamamoto; see LIGO-P940002.

[b] Single Mode Acquisition Code, developed by D. Redding, L. Needels and L. Sievers for LIGO lock acquisition simulation.

5.6. Acquisition Procedure

As the interferometer sequences through the different states, the supervisory control system must monitor the circulating power and alter the controller state as required. The general flow of how this will take place is outlined below.

5.6.1. State 1 initialization

All 6 of the test masses are under the local length damping control provided by SUS. The local alignment system is also activated so that the interferometer is aligned well enough (what “well enough” means is the subject of on-going work) so that length acquisition can proceed. The LSC Acquisition servos are active, but none of the test masses are under length control yet.

5.6.2. Acquiring State 2

The interferometer will sequence into State 2 when the *l*+ and *l*- degrees of freedom are simultaneously locked. Both sidebands become resonant in the recycling cavity while the carrier becomes anti-resonant. The *l*+ and *l*- degrees of freedom should acquire within seconds since the test mass threshold velocity of both of these loops is so high (in the range of 10 microns/sec; well-above the expected background rms velocity). Experience with the Phase Noise Interferometer bears this out.

5.6.3. Acquiring State 3

The interferometer will then transition into State 3. The laser loop controller, which has a high bandwidth, locks onto one of the arm cavities. The lock on the *l*- and *l*+ degrees of freedom is only slightly affected by the arm cavity locking transient. The sidebands remain resonant in the recycling cavity while the carrier becomes resonant in both the recycling cavity and one of the arms. The antisymmetric port of the beam splitter is the bright port for the carrier in this state, so a large fraction of the carrier light is lost out of this port; consequently the buildup of carrier power in the recycling cavity is minimal. The transition time from State 2 to State 3 should take only a few seconds since the threshold velocity is also in the 10 micron/sec range.

5.6.4. Acquiring State 4

Sequencing into State 4 is the most complicated part of the acquisition process. The threshold velocity of the *L*- loop is likely to be well below the expected rms test mass velocity (this will be verified in simulation before the FDR). In order to speed up the locking process due to the threshold velocity affect, a special real-time controller is added to the L- feedback path whose function is to reduce the effective rms velocity of the unlocked arm cavity. The Guided Lock controller is triggered when the transmitted light level of the unlocked arm cavity goes above a certain level as the cavity goes through a fringe. The Guided Lock controller calculates the relative velocity of the test masses from the transient signal, calculates a correction to the momentum and then kicks the end test mass back into the fringe with a reduced velocity. The Guided Lock controller is switched out of the loop and the linear controller is switched back into the loop just before the cavity reenters the fringe.

As the arm cavity enters the fringe and transitions into the locked state, the carrier power levels in the entire interferometer start to build up. As the power build-up occurs, the carrier light reflected from the recycling mirror transitions from an undercoupled state to an overcoupled state. When this transition occurs the $l+$ and $l-$ servos will go unstable unless the polarity of these loops are switched. Consequently, as the transmitted light in either arm goes above a predetermined level, a polarity switch is triggered on both the $l+$ and $l-$ loops. At this point, all length degrees of freedom of the interferometer are under control, although not operating in a low noise condition.

5.6.5. Stable Transition Through Pseudo-States

A possible solution to the $l+$ servo instability as the interferometer transitions through one of the pseudo-states, is to turn the $l+$ servo off for a a few tens of milliseconds. It is believed that the transient effect of the pseudo-state could be minimized this way. The best way of deriving a trigger signal will be investigated through simulation. Mitigation of potential pseudo-state instabilities will be modeled in the final design phase.

5.6.6. Integration Of Alignment/Length Control Acquisition

A plan for integrating the Alignment Acquisition with the Length Acquisition was presented in the Alignment Sensing/Control Preliminary Design (T970060-00-D) in Section 4.3. Briefly, the idea is to in fact misalign the arm end mirrors at the beginning of the process, and align them one at a time for State 3 and 4 acquisition. This strategy may not appreciably affect difficulties with sideband-resonant pseudo states, but may be a way to improve the interferometer’s basic alignment (using subsets of the Wavefront Sensing in State 2) if the lock acquisition alignment tolerance is difficult to meet under local alignment control.

5.6.7. Transition Into Detection Mode

Once the interferometer is locked, and Supervisory Control determines that all transient signals (such as wire resonances) have died down to acceptable levels, several transitions are triggered. First, the full ASC wavefront sensing control system is activated so that the interferometer is aligned properly; this will probably be necessary to bring residual deviations down to a level commensurate with the limited dynamic reserve afforded in Detection mode. The S_{RI} and S_{PI} sensing points are then swapped to allow adequate suppression of laser frequency noise. The Detection mode control characteristics are substituted for Acquisition mode servos, boosting low-frequency gains, lowering unity-gain bandwidths, and increasing stopband attenuations. Depending on implementation details, these transitions may be accomplished by briefly operating both controllers in parallel and adiabatically changing the ratio of their relative contributions to the relevant feedback actuator. Upon verification that all signals are within acceptable linear ranges, supervisory control declares the interferometer to be in Detection mode and signals DAQ that it is ready.

6. CALIBRATION

LSC carries responsibility for calibration of the recorded interferometer strain signal. The task involves two steps; to determine the ratio between the recorded signal S_{AQ} (or one derived from it) and an independent physical measurement of differential mirror motion, and then to maintain or update this ratio throughout interferometer operation as operating conditions vary. An absolute accuracy corresponding to ±5% in strain amplitude over the band spanning $40\ \mathrm{Hz} < f < 10\ \mathrm{kHz}$ and $\pm 50\,\mu\mathrm{s}$ in arrival time (or equivalent waveform phase) must be maintained, without encroaching on the interferometer's scientific availability.

The primary chain of reference for calibrating the interferometer readout will be based on the 1.06 µm wavelength of the Nd:YAG laser, through a procedure described in 6.2. This procedure is used in the suspended LIGO prototypes and has been found to be highly reliable, but nonetheless relies on stability of parameters measured “off-line” (for example, the coil/magnet force per unit current), requires high linearity to extrapolate signal levels over several decades, and shares signal paths and equipment with the operational control system. Due to the fundamental importance of the calibration function to LIGO's scientific mission, even where these potential sources of systematic error can be rigorously evaluated there remains strong motivation to provide an independent and redundant means of verification. Insofar as possible, such a “secondary” calibration standard should be based on a physically distinct mechanism and chain of reference. As a result, we propose to include a redundant, independent force calibrator based on photon recoil pressure, which we describe in 6.3.

Stability of the readout over time will be ensured by:

- choosing readout signals with minimal sensitivity to variable parameters (6.1.)
- periodic high-accuracy transfer function characterization using injected stimuli (6.4.), and
- model-based reconstruction of the transfer function based on the response to continuous low-level stimuli embedded in the data stream (6.5.).

The calibration system will also permit injection of arbitrary test waveforms, which may be used to simulate possible gravitational signals or to diagnostically excite specific response features found in the interferometer. These functions will be provided as a subset of the generic stimulus-response test capabilities provided for LSC and interferometer-wide diagnostics (Section 7).

6.1. Strain readout transfer function and errors

The unity gain frequency of the differential arm length (L_-) control loop lies within the gravitational wave detection band. In principle, to maintain independence from fluctuations in the optical transfer function of the interferometer (including alignment, power and operating point drifts) the gravitational wave signal is best determined from the control signal below the unity gain frequency and from the error signal above the unity gain frequency; a superposition of the two signals thus provides the highest degree of independence from loop gain. For a digital servo implementation (with high internal numerical precision, and thus no additive “electronic” noise) the transfer function between the error signal and the control signal is known to a high precision and, therefore, little additional information is gained by looking at the control signal. However,

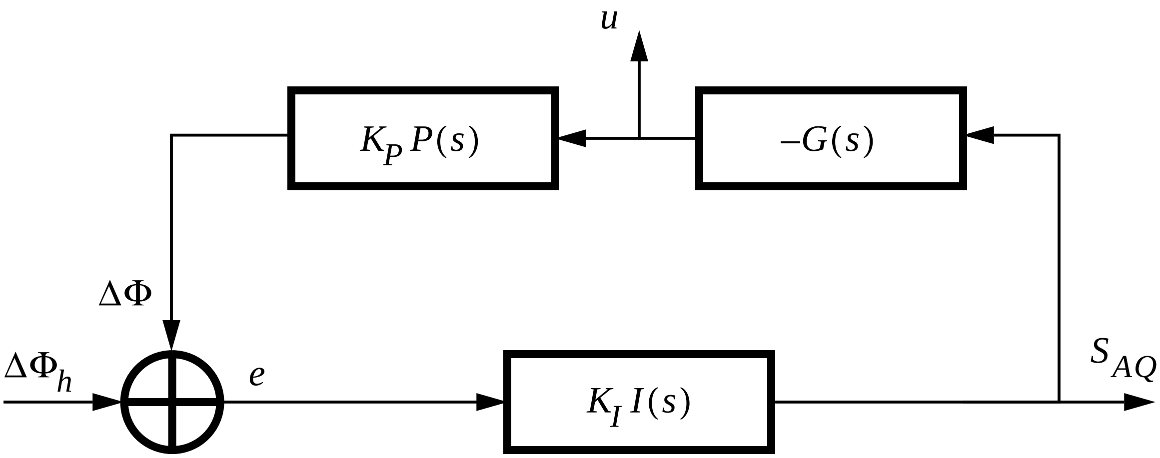

Figure 35: Servo loop model for differential arm length control. The gravitational wave signal $\Delta\Phi_h$ is added to the signal $\Delta\Phi$ coming from the suspended test mass, which has response function $P(s)$, to give error signal e. This error induces the antisymmetric port signal S_{AQ} through the response function of the interferometer $I(s)$. The feedback controller is described by $G(s)$ and produces control signal u. The constants K are multiplicative gain factors introduced to account for gain errors, and are nominally unity. Signals S_{AQ} and u are accessible as readouts and are redundant when $G(s)$ is known.

there may be significant analog components (current sources, unwhitening filters and the DAC itself) which may introduce time-varying errors, making direct monitoring of the current fed to the test mass force actuators desirable.

Since the crosscoupling from control of the Michelson degrees of freedom is small, one can perform the reconstruction of the gravitational wave signal with a one dimensional servo model (see Fig. 35). The closed loop response of the measured antisymmetric port signal S_{AQ} as function of the gravitational wave induced round-trip phase $\Delta\Phi_h$ then becomes

$$S_{AQ} = \frac{K_I I(s)}{1 + K_P K_I P(s) G(s) I(s)} \Delta\Phi_h \equiv GW(s) \Delta\Phi_h \tag{1}$$

Above the unity gain frequency the second term of the denominator in eqn. (1) is small compared to unity and the readout error is mainly given by the uncertainty in the optical/sensing gain K_I;. On the other hand, below the unity gain frequency the denominator is getting large and the readout error is dominated by the uncertainty in the controller gain K_P.

We can estimate the effect of fluctuation in the interferometer plant and controller transfer functions by taking the derivative of eqn. (1) with respect to the optical gain K_I and with respect to the (suspension) controller gain K_P. To further simplify the calculations we assume

$$I(s) = \frac{1}{1 + s/\omega_{cav}}, \quad P(s) = 1 \quad \text{and} \quad G(s) = \frac{\omega_{BW}(1 + s/\omega_{cav})}{s}. \tag{2}$$

where the L_- loop unity gain frequency is at $\omega_{BW}/2\pi$. Using $K_I = K_P = 1$ we then obtain

$$\frac{\Delta GW(s)}{GW(s)} = \frac{s}{\omega_{BW}(1 + s/\omega_{BW})}\Delta K_I - \frac{1}{1 + s/\omega_{BW}}\Delta K_P \tag{3}$$

From the above eqn. one can see that the optical gain error dominates above the unity gain frequency, whereas the controller gain error dominates below the unity gain frequency. Fig. 36 shows the relative contribution of an error in the optical gain and in the controller gain, respectively, to the gain error and timing error of the calibration function.

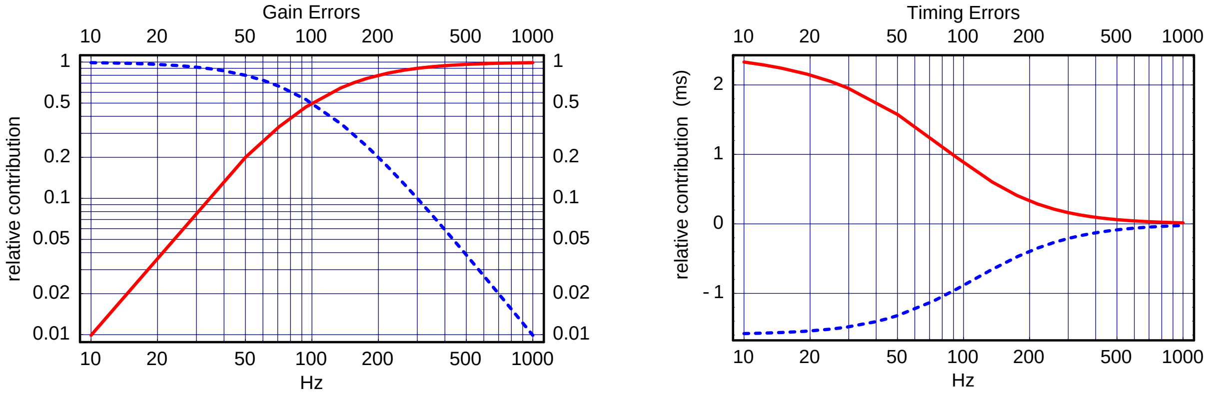

Figure 36: Relative contribution of an error in K_I (solid curve) and K_P to the gain error (left) and to the timing uncertainty. The unity gain frequency was chosen at 100 Hz.

Having established the relation between strain and readout voltage at a particular instant, subsequent fluctuations of the interferometer optical plant transfer function K_I (caused, for example, by misalignment or photodetector quantum efficiency drift) and the suspension controller, actuator and pendulum response K_P (caused, for example, by impedance or coil/magnet geometry changes) will limit accuracy at subsequent times. As shown above, these quantities must either be stabilized or monitored to better than 2.5% precision at all times to maintain the overall calibration accuracy of 5% in gain and 50 µsec in timing.

Figure 36 and Eq. (3) also suggest that continuous monitoring of the frequency response at two or three discrete frequencies should be adequate for reconstruction of the overall frequency response given independent errors in the plant and controls transfer functions. This is discussed further in 6.5.

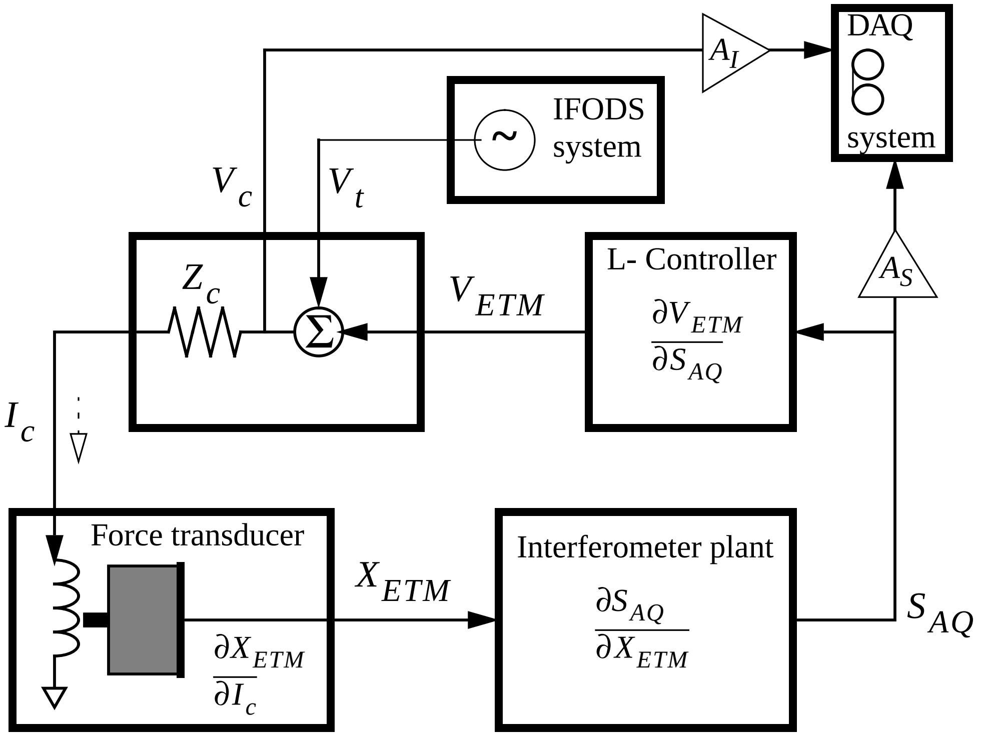

Figure 37: Simplified schematic of primary calibration in operation mode, showing the multiplicative factors subject to initial error or drift.

6.2. Primary calibration

The primary calibration is based on the Nd:YAG laser wavelength. With the recycling mirror and ETM's deliberately misaligned, the single-bounce Michelson interferometer will be driven through a full order using the suspension force actuators on each ITM at low frequencies (10 to 30 Hz). The drive current needed to achieve a full order will be recorded as a function of frequency. Then, the short, unrecycled Michelson will be locked at low gain and the demodulator signal will be monitored as smaller and smaller currents are injected to determine the linearity of the response (which must be corrected for the loop gain of the Michelson control, measured separately).

With the recycling mirror and end test masses realigned, the interferometer is locked and the coil current calibration is transferred to the ETM coil drivers as well, noting the drive current which gives an equivalent readout signal. At this point a detailed transfer function may be taken between the ETM coil drive current readout and the strain signal recorded by DAQ over the observation frequency band.

Analysis of potential errors in this procedure will depend to some degree on details of the electronics implementation, but we can anticipate several contributions which are likely to dominate.

6.2.1. Errors in initialization

To initialize the calibration of test mass suspension force per unit current with respect to the laser wavelength, we will excite the ITM suspension coils with a large[1] current to drive the mirror through one or more full orders. We must choose an excitation frequency which is sufficiently high that seismic noise does not appreciably influence the zero-crossings in the fringe signal, but at the same time must limit the drive current to the minimum practical value to respect the dynamic range available and minimize the degree of extrapolation needed. Since current needed to drive a the mirror through a full order increases as f^2 above the pendulum eigenfrequency and SUS controllers have a restricted output current range, direct comparison at frequencies within the active GW band is probably not feasible. For reference, frequencies of 10 to 20 Hz have been used in the 40m prototype. The primary measurement must therefore be extrapolated in both frequency (from 10 to as high as 10,000 Hz) and in amplitude (from .01 N at 10 Hz for a full order of motion to 4×10^{-11} N for a 0.01 fm test signal at 100 Hz, corresponding to drive currents between 0.5 A and 2 nA). These considerations lead us to anticipate errors of order $\pm 0.5\%$ in establishing the half-wave current in the presence of seismic noise, and comparable errors in transferring the wavelength of the laser to the ITM coil driver current at the operating frequency and amplitude.

6.2.2. Errors due to temporal variation and drift

Once measured and extrapolated to operating conditions, the primary calibration is subject to additional errors due to drift in several multiplicative factors, some of which are shown in Figure 37. Arguably the most variable factor depicted here is $\frac{\partial S_{AQ}}{\partial X_{ETM}}$, the interferometer plant transfer function, which depends on such variables as laser power, alignment, mode matching, detector quantum efficiency, RF tuning and local oscillator phase, and so on. In laboratory prototypes it has proven difficult to maintain better than 10% stability in this quantity over hours (although, with wavefront sensor-stabilized alignment, a major cause of this fluctuation is expected to be substantially reduced). By embedding continuous test signals it is possible to normalize out these variations ‘on the fly’ (along with variations in A_S, the strain readout conversion gain, and $\frac{\partial V_{ETM}}{\partial S_{AQ}}$, the loop controller compensation). As shown in Section 6.1., continuous measurement at two or three discrete frequencies (below, near and above the servo unity-gain point) should be adequate to normalize out fluctuations of these quantities in post-processing.

The transimpedance Z_c of the suspension coil driver current sensing output (including coil and line impedance, if they are not separately normalized) can fluctuate with temperature or component age, as can the conversion gain A_I of the readout, ADC and whitening filter. In principle each of these is externally accessible and might be separately tested, although if done often (more than once per 40 hours) the interruption could impact interferometer availability.

---

[1] by Detection mode standards

The coil/magnet force coefficient $\frac{\partial X_{ETM}}{\partial I_c}$ is difficult to monitor or track without returning to the invasive fringe-interpolation procedure outlined above. Errors in this quantity translate directly into misinterpretation of the amount of calibration force applied to the mirror. Three possible sources of variation in this coefficient are under consideration:

- Temperature or aging variation in the magnetization of the permanent magnet
- Temperature or aging variation in the geometry of the coil
- Spatial variation of the position of the magnet within the coil field

While averaging results of calibrations using the four test mass suspensions may help in reducing errors, it is worth noting that (at least in some scenarios) these systematic effects may be correlated between the different mirrors in an interferometer.

Preliminary estimates for some of the calibration error sources presented above are summarized in Table 12 .

Table 12: Primary calibration error estimates.

Description	variable	init. error	est. drift (1 hr)	est. drift (40 hr)
Coil current readout impedance	Z_C	.05%	.1%	.5%
Coil readout conversion gain	A_I	.05%	.1%	.5%
ETM mass	M	.1%	N/A	N/A
Coil/magnet force coefficient	$\frac{\partial X_{ETM}}{\partial I_c}$	1%	.5%	2%

6.3. Secondary calibration

The secondary calibration system will be based on photon recoil, as shown in Figure 38. The beam from a solid state laser will be directed through a BSC viewport onto the online ETM front surface. This laser will be chosen for high power (approximately 1W), high reflectivity on the ETM coating at the design angle of incidence, power stability, and capability for modulation; spatial and temporal mode quality are not significant factors except insofar as they affect power sta-

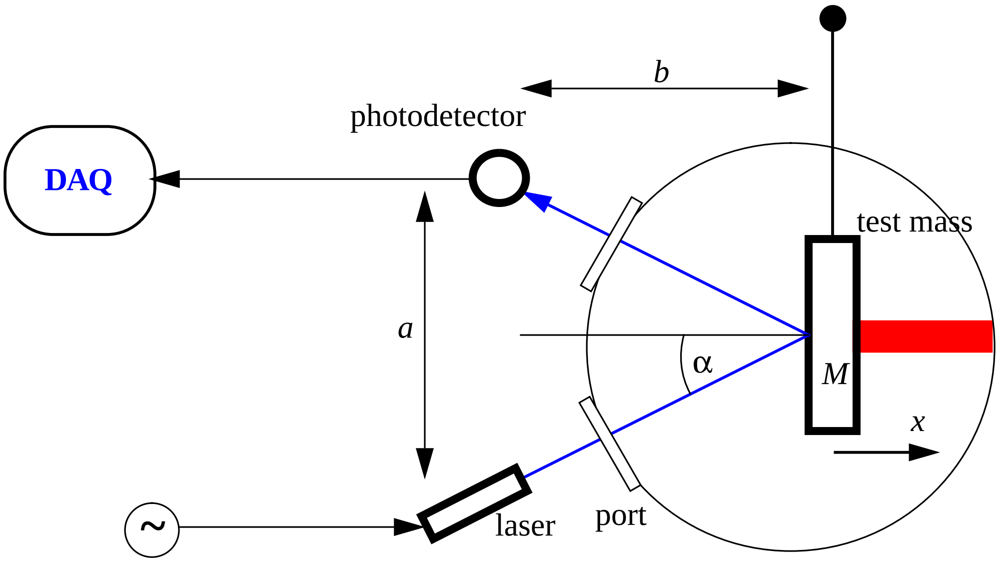

Figure 38: Schematic of a photon-recoil based calibration actuator.

bility. Multimode fiber-coupled diode laser modules (typically used in electronic fabrication and surgical applications) are strong candidates.

The laser power is modulated by a user-specified waveform. The incident power (and/or reflected power, if collected) will be monitored by an independent photodetector, whose output is initially (and at intervals) compared with the direct optical power reflected by the ETM. This calibration will normalize factors like the transmission of the vacuum viewport, reflectivity of the ETM, and beam sampler and attenuator transmissions. In this way the photodetector output voltage will be referenced to a calibrated optical power meter, which (in turn) will have NIST-traceable certification at the design wavelength. The error of this power meter's calibration and the stability of the photodetector's quantum efficiency over time are likely to be the dominant factors in the overall error budget.

The recoil of the photons bounced off the mirror surface imparts momentum. If the incident angle is α the applied force is

$$F = 2\cos\alpha\frac{h\nu}{c}\dot{N}_{\gamma} \tag{4}$$

where $\dot{N}_{\gamma}$ is the number of photons hitting the mirror per time. Expressing the photon rate in units of the light power P yields

$$\dot{N}_{\gamma} = \frac{P}{h\nu} \quad \Rightarrow \quad F = 2\cos\alpha\frac{P}{c} \tag{5}$$

Treating the test mass as a simple pendulum and writing the light power as

$$P(t) = P_0 + P\cos\omega_c t \tag{6}$$

the displacement amplitude of test mass can be written as

$$x_c(\omega_c) = 2\cos\alpha\,\frac{P}{cM}\,\frac{1}{\omega_p^2 - \omega_c^2 + i\omega_p\omega_c/Q} \approx -2\frac{\cos\alpha\,P}{cM\omega_c^2} \quad \text{for} \quad \omega_c \gg \omega_p \tag{7}$$

where ω_p and Q are the angular frequency and Q of the pendulum. As an example we take a laser with power $P \approx 100\,\text{mW}$, an incident angle close to normal and a test mass of $M \approx 10\,\text{kg}$; the displacement amplitude at $100\,\text{Hz}$ is then $x_c \approx 1.7\times10^{-16}\,\text{m}$.

The uncertainties of a photon actuator can be directly derived from eqn. (7); an estimate is presented in Table 13 . The largest uncertainty will be in the measurement of the absolute laser power. This expected error is dominated by the specified accuracy of commercially available power meters used to calibrate the monitor photodetector, and may be improved substantially by use of more specialized detectors (for example, photodiodes exceeding 99% quantum efficiency are available for some laser wavelengths).

Table 13: Photon recoil calibrator error estimates.

Description	variable	nom. value	est. error + drift	unit
Laser power	P	1 – 100	2%	mW
Laser wavelength	λ	980	0.5%	nm
ETM mass	M	10.70	0.1%[a]	kg
Incident angle cosine	$\cos\alpha$	.7	0.1%	~
Vacuum viewport transmission	T	.99	0.2%	
Monitor photodiode responsivity	R	100	0.2%	V/W

[a] Air buoyancy correction is of order 8 g.

6.4. Wideband frequency response characterization

During operation, the frequency response of the interferometer and its readout system is measured periodically by exciting either the photon recoil calibrator or ETM suspension test inputs with a swept sine, broadband pseudorandom sequence, or other waveform[1]. The transfer functions between injected suspension coil current, or modulated laser sample power, and readout signals are measured and converted into units of equivalent displacement using the previously measured calibration factor. This transfer function is stored with the interferometer data and used in data

---

[1] For example, a test waveform tailored to the measured spectral density of the interferometer noise will permit higher overall measurement accuracy with less injected energy and/or less downtime per measurement.

analysis to deconvolve the response function, converting the recorded signal time series into a representation of astrophysical strain (or other convenient basis).

Transfer function measurements will be invasive and detract from interferometer availability, so it is desirable to minimize the frequency and duration. It is also necessary to balance dynamic range against accuracy and dwell time per test. For example, in a standard “swept sine” frequency response test, the fractional precision in the transfer function $K(f)$ in a given frequency bin f_0 is limited by the random interferometer noise background with power spectral density $S_v(f_0)$ to

$$\frac{\delta K}{K_0}(f_0) \geq \frac{1}{V_t(f_0)}\sqrt{\frac{S_v(f_0)}{\tau}}$$

where $V_t(f_0)$ is the readout voltage resulting from the test signal and τ is the measurement dwell time. To achieve 1% fractional accuracy with a dwell time of 1 second per bin (17 minutes for a 1024-point sweep) requires an injected signal amplitude which exceeds the local background noise in a 1 Hz bandwidth by a factor of 100 (10^4 in power). Even if the dynamic reserve of the data acquisition (DAQ) system is deemed adequate, it is possible for this signal size to exceed the dynamic reserve limits of the LSC detection mode controls themselves at certain frequencies. Using a pseudorandom excitation to address multiple bins simultaneously will correspondingly increase the total energy added by the excitation, or take the same time for a fixed total added energy, to achieve a given total accuracy. As a result, it is desirable to minimize the frequency of detailed all-frequency transfer-function measurements.

6.5. CW sine calibration

As a result we propose to maintain three continuous sinusoidal test signals at different frequencies throughout operation. The frequencies will be chosen below, near and above the unity-gain frequency of the L_- control loop (approximately 50 Hz, 150 Hz and 800 Hz TBR), and simultaneously monitor the coil current at each frequency along with the response in the strain signal. Post-recording (or online) data processing will include a procedure to evaluate the transfer function between coil current monitor and strain readout S_{AQ} at each probe frequency, and use the result to update the form of the most recent swept-sine transfer function measurement according to the parametric formulation discussed above.

The amplitudes of these CW calibration tones will add insignificant signal power compared to, for example, thermally driven suspension wire resonances. As an illustrative example, coherent integration of a test probe signal whose power just equals the broadband noise power in the interferometer noise background in the adjacent 100 Hz bandwidth will yield a 1% measurement of the transfer function in 100 seconds, which we expect to be much shorter than the time over which readout parameters vary significantly. The actual level, and thus convergence time to the specified accuracy, will be adjusted to accommodate the observed rate and magnitude of change in the interferometer transfer function.

7 DIAGNOSTICS

7.1. Requirements

The requirements are divided into sections covering the digital part of the LSC system (loop transfer functions and data transfer), the low frequency analog part (front-end and back-end electronics), the RF part (photodetector, demodulator and rf source) and the video cameras (beam monitoring).

7.1.1. Digital part

The primary requirements for the digital part of the LSC system are as follows:

- The LSC diagnostics subsystem must be able to extract and display any (digital) LSC signal, including internal servo signals.
- It must be able to add a stimulus to every LSC error and/or control signal using predefined waveforms (in band and out of band, up to several kHz).
- It has the ability to store all important LSC signals plus a number of auxiliary signals simultaneously on disk for time intervals up to 1h.
- It is able to correlate the LSC diagnostics read-outs with PEM signals (off-line).

Deduced from the primary requirements are some secondary requirements which should make performing the diagnostics procedure more convenient:

- A high bandwidth digital link is necessary between LSC and diagnostics.
- The storage hardware of the diagnostics system has to be able to sustain this data rate for about 1h.
- To support the PEM cross correlation the ISC sampling frequencies are integer multiples (or integer fractions) of the basic DAQ rate of 16384Hz.
- Timing accuracy of the data written by the diagnostics systems is half a DAQ tick, i.e. ~30µs.
- The data formats of DAQ and diagnostics are identical, i.e. the FRAME format is also used for the diagnostics data stream.

7.1.2. Low frequency analog part

- Crucial LSC signals which exist in analog form only (a candidate is the laser loop feedback) have to be digitized for the diagnostics system.
- The remaining analog circuits (mainly amplifiers and filters) do not have be tested on the system level, nor have the tests to be computer controlled. For instance, anti-aliasing filters can be tested channel by channel by applying a test signal at the input and watching the output.

7.1.3. RF part

- The rf signals of each LSC length sensor signal can be monitored by taking snapshots (scope function).
- To be able to reconstruct the full information carried by the modulation signal the down-conversion is performed in both phases.

- The rf phase of the down-converted length signals can be adjusted remotely.
- It can be verified that the RF sources supplies a local oscillator signal of the desired frequency and amplitude
- Special purpose RF test equipment (e.g., spectrum and network analyzers TBD) can be interfaced, controlled as part of test procedures, and have their data integrated with other diagnostic information..

7.1.4. Optical Spectrum Analyzers and Video cameras (owned by ASC)

- At each port the intensity ratio between carrier and sidebands can be determined by a spectrum analyzer.
- Video cameras monitor the beam at each port and can be used to as visual ‘lock’ indicators.
- Single images of the beam can be stored for off-line analysis to investigate the higher order mode contents.

7.2. General description and overview

A diagnostics system has to be implemented for both LSC and ASC. To simplify the design work we propose an ISC diagnostics concept which should allow to diagnose and test LSC and ASC in an unified way. However, we include the ASC system only in the overview and do not work out the details of its implementation in this document.

7.2.1. Design overview

Because of the different nature and the different requirements we make a clear conceptual distinction between the on-line and the off-line diagnostics system. Even so, in reality both system may rely on the same sensing hardware and/or data transfer mechanisms. The ISC on-line diagnostics system will use the infrastructure provided by the LIGO diagnostics system (LIGO-T970078-00) for collecting and displaying data in real-time. On the other hand, the ISC off-line diagnostics system will be responsible for collecting complete data sets describing the state of the interferometer and storing them on disk for later use. It will use storage hardware similar to the one developed for the DAQ system (LIGO-T960010-00).

Figure 39 shows the typical information flow in the LSC system. Sensor signals describing the four length error signals is digitized at the front-end, sent to a servo controller which implements the digital network and finally sent to the back-end controller where the signal is transformed into an analog control signal again. Since all information necessary to describe the (LSC) state of the interferometer is available in digital form at the servo controller, both on-line and off-line diagnostics systems will need to communicate with the LSC servo controller through a digital link. This will provide all the necessary data for the off-line system. For the on-line system additional input channels are foreseen. High frequency digitizers will provide snapshots of the measured RF signals and the local oscillator signals supplied by the RF source. Video cameras will take pictures of beam profiles and directly sent them to the operator screen. A layout overview is shown in Fig. 40.

To perform LSC stimulus-response diagnostics tests one has to be able to add arbitrary waveforms to servo signals anywhere in the LSC compensation network. Since all these signal injection points are available in digital form at the LSC servo, the method of choice is to generated the stimulus directly in digital form and add them to the servo signals digitally. Because the waveforms are known beforehand, the LSC servo should be able to produce these signals from look-up tables which are stored internally. To be able to reconstruct the stimulus off-line, the stimulus signals are read-back by the ISC diagnostics network and stored on disk together with all the other information.

To simplify the diagnostics supervisory control all diagnostics information including the read-backs of the stimuli are permanently and immediately (~ 1/10 sec) available on the ISC diagnostics network. The supervisory control is then responsible to load new stimuli waveforms into the servo controller, to switch the stimuli on and off and to start and stop the storage process. On user demand the on-line diagnostics software can select one or more data channels, scope traces or camera images and display them in real-time; basic analysis tools are available (see LIGO-T970078-00).

7.2.2. Interfaces

The interfaces between the ISC diagnostics subsystem and the LIGO diagnostics system are standard CDS; they are described in LIGO-T960108-00.

- ISC diagnostics network: reflected memory modules
- Fast digitizers: reflected memory modules or standard computer network (GPIB, TCP/IP)
- Spectrum Analyzers: reflected memory modules or standard computer network
- Video cameras: standard computer network (TCP/IP)
- ISC diagnostics supervisory control: EPICS

7.2.3. Functions

7.2.3.1 Passive monitoring of internal signals

The diagnostics system has to be fully operational during detection mode. Of course, it can not be expected that gravitational wave data is still valid when a stimulus is added to the system. Thus, the preferred diagnostics function during data taking is the passive monitoring. Diagnostics channels can be monitored by an operator with the on-line diagnostics system in real-time. This data can then be analyzed visually or with some basic analysis tools. These functions are provided

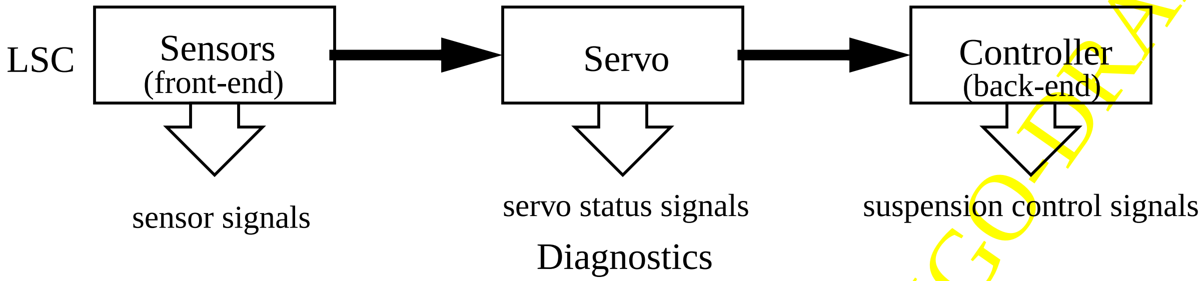

Figure 39: Typical information flow in the LSC system.

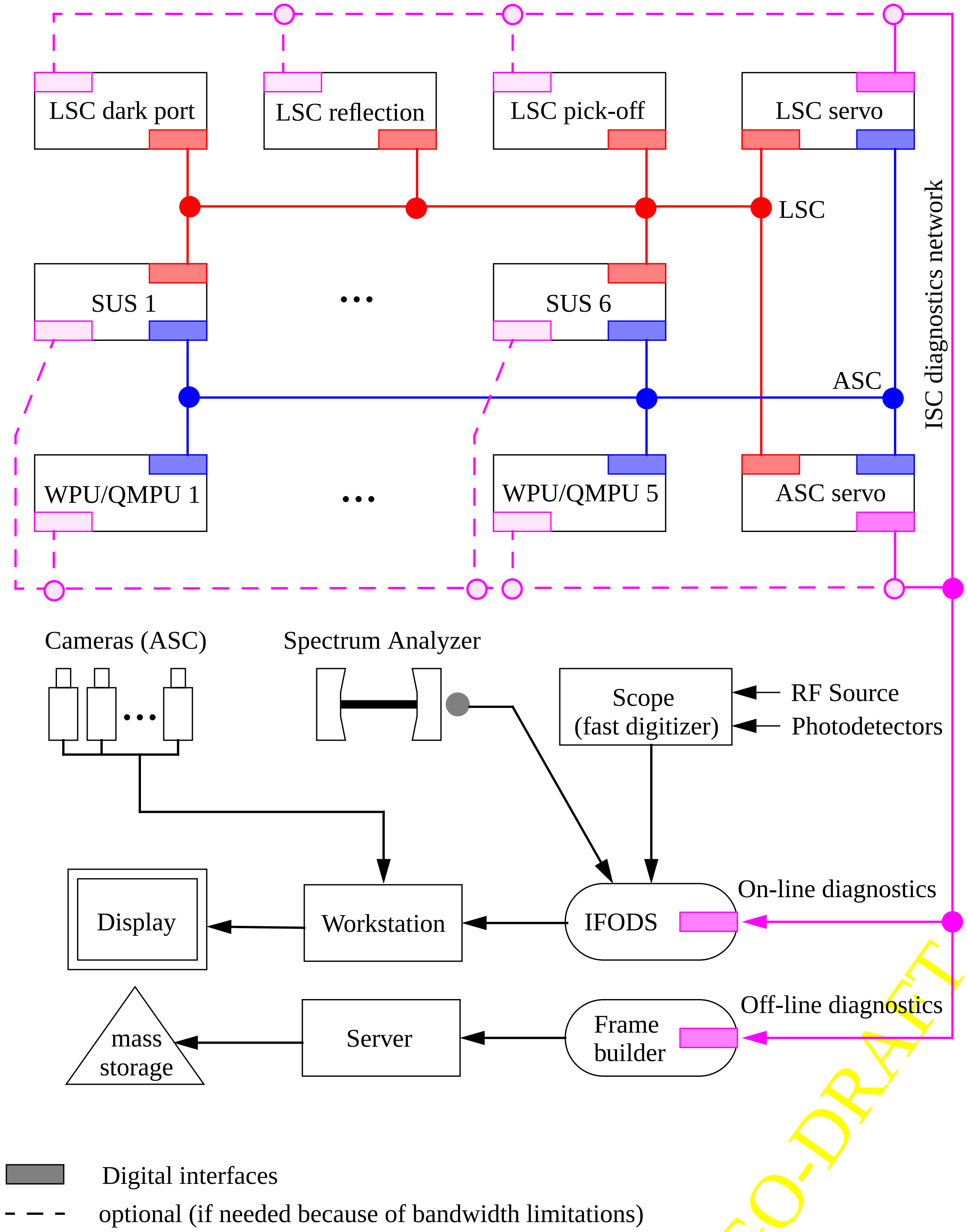

Figure 40: ISC diagnostics subsystem overview. Shown are the inter-connections between ISC and the LIGO diagnostics system.

by the LIGO on-line diagnostics system and are not part of the ISC diagnostics subsystem (LIGO-T970078-00). An other way to monitor the system is to invoke the off-line diagnostics system and store diagnostics data in parallel to the DAQ data stream on file. A data subset generator will then take both data streams and combine them into a new frame-formatted file which will contain all data necessary to make cross-correlations between the LSC channels and, e.g., the PEM channels.

The passive monitoring of internal signals will also play an important role during the time when the lock acquisition algorithm is put into operation. The implementation of the lock acquisition algorithm will generate special (diagnostics) status signals which will describe its exact internal state. Together with the interferometer state information provided by the ISC sensors this will be a powerful tool to diagnose and debug the transition schedule of the lock acquisition.

7.2.3.2 Stimulus-response diagnostics

Stimulus-response diagnostic testing must be available for all control states (i.e. transition to this diagnostic mode must be directly accessible from Acquisition and Detection operating modes, as well as from other Diagnostic modes). In this mode a test signal is directed to an injection test point or points, and system outputs are monitored to determine the transfer function, response linearity, time delay and other characteristics. The amount of test signal power required for accurate measurements, and the presence of the additional waveform source and readout connections, will generally limit the usefulness of strain data recorded during these tests. The calibration procedure described above, which gives the overall frequency response between gravitational wave strain and readout voltage, is one instance in this class of tests. Other tests in this category involve simultaneously adding a DC offset or out-of-band signal (such as bandlimited random noise) to another test point, to determine parametric sensitivities (e.g. to laser intensity noise).

Other interferometer subsystems and the interferometer as a whole will also be subjected to stimulus-response tests. LSC-response readout of test signals injected throughout the interferometer will be a principal means to gauge other subsystems' performance and interactions. Tests in this category are discussed further in LIGO-T960031-00-E, “CDS On-line Diagnostic and Readout Functions.”

7.2.3.3 Variations in control topology

To isolate control path interactions and noise sources it will be necessary to disable or disturb one or more feedback paths while leaving other paths operational. For example, the common-mode L_+ loop could be operated with feedback to the SEI/SUS actuators disabled or attenuated, or with feedback to the PSL disabled or attenuated. Each of these conditions would temporarily compromise sensitivity, but would enable effective separation of laser frequency, seismic and electronic noise effects, as well as permit effective characterization of the “disabled” feedback path's transfer function. However, reallocation of loop gain or dynamic range may be necessary to accomplish this. Other examples of diagnostics involving control topology variation may include:

- removal of DM (or CM) length control signals from ITM (or ETM) drive paths
- disabling SEI drift/tidal motion feedback for one or more optics
- radical alteration of l_- loop gain (to probe relationship between auxiliary sensor shot noise, residual fringe error, and intensity noise, for example.).

7.2.3.4 Variations in optical topology

To successfully commission the LIGO detector, verify operation of its component subsystems, and determine its parameters for subsequent optimization, it is necessary to operate subsets of its optical system. LSC controls will support the following “reduced” interferometer optical configurations:

- recycled singlebounce Michelson interferometer (ETM’s blocked or grossly misaligned).
- simple Michelson interferometer (RM removed, ETM’s blocked or grossly misaligned)
- coupled cavity (BS removed, or high reflector substituted)
- unrecycled FP michelson (RM removed)
- single, uncoupled Fabry-Perot cavity (RM removed, one cavity blocked or misaligned)

With the possible exception of the first (recycled Michelson), each of these involves radical alteration of the in-vacuum optics, so use of these modes after commissioning is expected to be infrequent. The design optimization will favor solutions which provide these capabilities automatically as subsets of the normal control modes, to minimize the additional investment of dedicated hardware and software in these applications.

7.2.3.5 The 37 kHz option

Since the displacement sensitivity at the FSR of the arm cavities is as good as at 150 Hz, it can be an interesting region to do some diagnostics tests and compare their result with the values obtained at the gravitational-wave band. A special diagnostics option may allow to sample and store data in a 10 kHz band around this frequency (either by having a high enough sampling rate or by down-conversion).

7.2.4. Displays

The ISC on-line diagnostics display is part of the LIGO diagnostics display (LIGO-T970078-00). Since the main LIGO diagnostics display is located in the control room, a remotely logged-in laptop computer will allow to read these displays at location.

7.2.5. Channel count

A list of LSC diagnostics channels is presented in Table 14. The number of channels is between 74 and 146. Using a sampling rate of 16384 kHz the data rate becomes of order several MB/s.

Table 14: LSC diagnostics channel count.

Name	*Description*	*signal*	*mul.*
Sensor signals			
S_{AQ}	dark port signal	numerical	8[a]
S_{RI}	reflection signal	numerical	8[a]
S_{PQ}^{x}	pick-off x differential signal	numerical	8[a]
S_{PI}^{x}	pick-off x common signal	numerical	8[a]
S_{PQ}^{y}	pick-off y differential signal	numerical	8[a]
S_{PI}^{y}	pick-off y common signal	numerical	8[a]
S_{AI}	dark port orthogonal signal	numerical	8[a]
S_{RQ}	reflection orthogonal signal	numerical	8[a]
P	beam power monitoring	numerical	6
S_{DC}	photodiode DC signals	numerical	4×8[b]
S_{RF}	RF photocurrent	RF	4×8[b]
f_M	modulation frequency (RF source)	RF	2
video	beam profiles	TV (ASC)	6
spectrum analyzer	carrier - sideband intensity ratio	TBD	3
Controller signals			
G_A	differential arm cavity length	numerical	1
G_{l_-}	Michelson length	numerical	2
G_{l_+}	recycling cavity length	numerical	2
G_{ν_l}	laser frequency	numerical	1
G_{L_+}	common arm length	numerical	1
G_M	suspension length control signals	numerical	6
G_{kick}	guided lock acquisition signals	numerical	4[c]
I_{coil}	SUS coil driver read-back	numerical (DAQ)	24
Status signals			
	length servo status	numerical	
	lock acquisition status	numerical	
Stimulus read-back signals			
S_{stim}	error signal offset	numerical	4
G_{stim}	control signal offset	numerical	13
P_{stim}	photon actuator power read-back	numerical (DAQ)	2
Reserved			
	future use	numerical	10

[a] Maximum multiplicity in case each photodiode is sampled individually.
[b] Assuming 8 photodiodes are used per photodetector assembly.
[c] Assuming guided lock acquisition is implemented.

7.3. Diagnostic Procedures

Some of the diagnostics procedures describe in this section are also part of the LIGO diagnostics tests (LIGO-T970078-00) and are more completely documented there.

7.3.1. Plant sensitivity

The dc response of the interferometer is measured by applying in-band dither signals of different frequency simultaneously to all length error signals. The plant matrix can then be deduced from the ratio of the measured photocurrents over the applied displacement signals.

To determine the frequency dependence of the plant matrix its frequency response is measured for each loop individually. In band the dither signal is added to the error signal, whereas out of band the dither signal is added to the corresponding control signals.

7.3.2. Interferometer noise floor

The noise floor of the light incident to the photodetectors is measured by taking long time series of the error signals and making a Fourier analysis. By knowing the plant sensitivity the noise levels can be transformed into displacement sensitivities.

7.3.3. Laser noise coupling

Laser noise can either be frequency noise or amplitude noise. The laser frequency noise coupling into the length sensing system is measured by applying a dither signal to the error signal of the frequency stabilization loop. The laser amplitude noise is either measured by varying the laser output power (function provided by PSL) or by dithering the length of the mode cleaner (function provided by IOO).

7.3.4. Oscillator noise coupling

For measuring their coupling coefficients into the length system oscillator phase noise and oscillator amplitude noise can be simulated by dithering the frequency and the amplitude of the modulation signal at the output of the RF source. Since the present RF source does not provide these capabilities at the necessary level, the RF source has to be replaced by a frequency synthesizer to perform these measurements.

7.3.5. Beam jitter coupling

Beam jitter coupling is measured by applying a dither signal to one (or both) of the mode matching telescope mirrors (function provided by IOO) and measuring the resulting length signal at the dark port. Because one does not expect this coupling to be have a frequency dependence, making the measurement at one frequency is enough. On the other hand, the angular dither frequency should be chosen as high as possible, since the antisymmetric port length sensitivity is best at about 150 Hz.

7.3.6. Alignment coupling

To determine the coupling of angular degrees-of-freedom into the length sensing system, angular dither signals of different frequencies are applied to all of the interferometer mirrors (function provided by ASC) and the resulting signals of the length sensors are measured. Because one does not expect this coupling to be have a frequency dependence, one frequency per angular degree-of-freedom is enough. On the other hand, the angular dither frequencies should be chosen as high as possible, since the length sensitivity is best above the ‘seismic wall’.

An other effect is the reduction of displacement sensitivity when the interferometer is misaligned. This is measured by monitoring the amplitude of a (differential arm cavity) length dither and the corresponding noise floor on the light as a function of a slowly varying alignment state (function provided by ASC).

7.3.7. Sensor response and noise

The sensor response, i.e. the transimpedance and the responsitivity of the photodetectors, are best measured off-line on the bench. The RF transfer function can be measured with the help of an RF network analyzer and an AM laser source, whereas the absolute sensitivity can be determined from the shot noise induced by an (unmodulated) YAG laser source. Overall electronic noise is best measured by putting the photodiodes into the dark and determine its noise floor.

7.3.8. Actuator response and noise

The actuator response is measured off-line by applying a dither signal at the LSC input of the suspension controller and by reading back the actual coil driver currents. To obtain a physical displacement one will have to rely on the calculated value between magnetic force and coil current and on the pendulum transfer function.

7.3.9. Servo loop performance

The open-loop gain of an LSC servo loop can be measured by adding a dither signal to the length error signal and determining the gain suppression from the sum signal. Repeating this measurement for different frequencies will allow to determine the open-loop transfer function.

The closed-loop transfer function is determined by applying the same dither signals, but looking at the controller signals. If the servo loop has a crossover, shape and frequency of the crossover can be determined from the ratio of the two involved control signals.

An alternative method to determine the bandwidth of the servo system is the step response. Adding a low frequency square wave signal to the length error signal will force the system to react as fast as it can. The phase margin of the servo loop can then be easily deduced from the measured over-shoot.

7.3.10. Mode matching

The mode matching into the interferometer is done by minimizing the power reflected from the interferometer. The mode matching telescope is used to change in input beam size and divergence, either by stepping through a larger range of beam parameters or by a small-amplitude dithering which is then extrapolate to the minimum.

7.3.11. Intensity ratio between carrier and sidebands

The intensity ratio between carrier and sidebands can be determined by spectrum analyzer which are placed at the extraction ports. By sweeping the length of the analyzer cavity and looking at the light in its transmission the different frequency components on the light can be separated. A peak height analysis will then directly yield the power ratios.

7.3.12. Intermodulation products due to offsets

These type of measurement are performed to determine the linearity of the system. Typically, one of the above measurements is done in the presence of an offset which is added to one of the servo loop error signals. For more details see LIGO-T970078-00.

7.3.13. Two-tone intermodulation tests

This kind of tests is similar to the ones above except that the offset which is added to one of the servo loop error signal is not static, but a sinusoidal signal of a chosen frequency (which in general is different from the frequency of the test stimulus). The measurement then looks at intermodulation products occurring at the sum and difference of the two stimulus frequencies.

7.3.14. Internal test mass resonances, wire resonances and pendulum Qs

In principle, LSC has no responsibility to determine test mass resonances, wire resonances or pendulum Qs. However, SUS may want to use the LSC/ASC capability to apply arbitrary waveform signals to the inputs of the suspension controllers.

7.3.15. Cavity storage times

The arm cavity storage time can be either deduced from a ring-down measurement or from a measurement of the cavity pole frequency. The ring-down measurement is performed by a step modulation of the laser intensity when only one arm cavity is locked. The ring-down or decay time is then a measure for the storage time. The measurement of the arm cavity pole frequency can be done when the whole interferometer is locked by measuring the optical transfer function at the antisymmetric port.

On the other hand, the determination of the pole frequency in reflection is a measure of the double resonance storage time. There is no good way to determine the storage time of the recycling cavity alone. But, this is also of smaller interest, since the sidebands which are the only frequencies simply resonating in the recycling cavity do see so much additional loss through the dark port that it significantly alters their storage time.

7.3.16. Mirror losses

When the input mirror transmission coefficients are known and when the light coupling into the interferometer is understood, the cavity losses can be calculated from the missing power in reflection. This method works for both the power missing in reflection of the arm cavities and the power missing in reflection of the recycling cavity. The best way to measure the missing power is to drive slowly over the resonance and measure directly the ‘dip in reflection’.

7.3.17. Higher order modes contamination

One can obtain an idea of how much power is stored in higher order modes by looking at the beam profiles which are measured by the video cameras and determine the overlap with a pure TEM_{00} mode.

7.3.18. External influences

External influences are, among others, the seismic excitations, the tides, the acoustic noise and the earth magnetic field. The coupling of these effects into the gravitational wave readout is determined by cross-correlating the antisymmetric port signal with the corresponding PEM channels (measured by the DAQ system). In reality, the correlation may be weak due to effort which went into the isolation systems and, therefore, the coupling coefficients hard to determine. Sometimes, it is possible to enhance the strength of the external influences by using shakers, loudspeakers, strong magnets, etc.

7.3.19. Electronics self-tests

A self-test procedure will allow to verify that all important LSC components are operational and that the necessary software is running correctly. This self-test entirely relays on built-in features and no additional hardware is foreseen.

7.4. Plant subset operational modes

To help the commissioning of the LIGO interferometer LSC has to be able to change its control topology, so that it can support several operational modes which include only a subset of the full interferometer optics (see Section 7.2.3.4). Some of these subsets demand the removal of an optical component, whereas others can be achieved by misaligning not involved optical components. It is clear that the removal of a large interferometer mirror is a major disturbance to the system and can conveniently be done only during initial setup and commissioning. Later on, these configurations will be set together very infrequently (if at all). This section will concentrate on subsets which can be obtained by misalignment of optical components only, i.e. none of them has to be removed. Generally, this means that these configurations have to work with a reduced light power on the beamsplitter and in most cases with largely reduced length sensitivity.

7.4.1. Short Michelson

One can obtain a simple Michelson interferometer by misaligning both ETMs and the RM. The power on the beamsplitter is then about 3 orders of magnitude smaller than during normal detection mode. Furthermore, the sidebands are not optimally coupled to the antisymmetric port and, thus, further reducing the dark port signal. Only the signal at the antisymmetric port will be needed to control and align this configuration. Of course, the signal slope will also be smaller, since there is no enhancement from the recycling cavity anymore. However, this should be not so critical, because larger r.m.s. length fluctuations are allowed in this mode.

7.4.2. Recycled short Michelson

This configuration is obtained by turning away both ETMs. However, in contrast to the LIGO configuration the sidebands will not be resonant in the recycling cavity anymore. Hence, the signal at the antisymmetric port and at the pick-off will have further reduced sensitivity. To control this configuration the signals in reflection and at the antisymmetric port will be needed. Since the recycling cavity will be degenerate, angular alignment requirements will be as high as during detection mode. But, this configuration can be used to test some aspects of the frequency stabilization servo loop.

7.4.3. Linear RM/ITM cavity

A short cavity can be formed by misaligning both ETMs and one of the ITMs. Since the beamsplitter will take away 50% of the light power with each pass, the finesse of the cavity will be marginal. This configuration can be controlled from the signal in reflection. However, it is likely that this configuration will have little importance.

7.4.4. Single arm cavity

By misaligning the RM and one of the ITMs a configuration consisting of a single arm cavity can be formed. The input power to the arm cavity would be about 3 to 4 orders of magnitudes lower than during normal detection mode. The best place to measure the error signal would be at the antisymmetric port. An interesting possibility of this subset the ability for angular alignment of the ETMs using the WFS at the antisymmetric port and in reflection. However, the alignment signals will be rather small due to the low power incident on the quadrant photodetectors.

7.5. Analysis tools

7.5.1. On-line

The on-line analysis tools are provided by the LIGO diagnostics system (LIGO-T960031-00).

7.5.2. Off-line

To read and preprocess the diagnostics data stored on file the off-line diagnostics analysis will relay on software tools developed for the data analysis. Most of the remaining analysis is numerically not very demanding and can be done with standard commercial packages (such as Mathematica or Matlab). For each standardized diagnostics procedure there will be designated (macro) program which will allow for a fully automatic analysis.

8. PLANNED PROTOTYPE TESTS FOR FINAL DESIGN PHASE

8.1. 40-meter Recycling program

The objective of the 40m recycling program is to demonstrate and investigate lock acquisition. The acquisition sequence that has been developed with modeling will be tested, and we expect that the results will provide valuable input to the further definition of the lock acquisition procedure for LIGO as well as validation of SMAC and other design tools.

8.2. Phase Noise experiment

The primary objective of the Phase Noise experiment, in its reincarnation at 1064 nm, is to demonstrate the phase sensitivity of LIGO, at the level of 7×10^{-11} rad/√Hz. This objective does not feed directly into any particular design aspect of the LSC, but it provides assurance that the LIGO shot noise sensitivity can be attained, and may provide valuable information on familiar and unforeseen noise sources.

The PNI will also be implementing photodetector hardware that is very similar to that being designed for LIGO. The anti-symmtetric port output will be detected with a 2 mm Hamamatsu InGaAs photodiode, and the preamplifier being used is a prototype for the LIGO preamp. One important difference between the conditions under which the diodes have been tested to date and the conditions at the anti-symmetric port of an interferometer is that in the latter case a large fraction of the total power is modulated at twice the modulation frequency. There is some concern over whether this will change the response of the detector, and the PNI will experience will be valuable in that it does provide realistic spectral content in the signal. We also intend to use the actual LIGO prototype photodetector (descirbed below) on the PNI, after it has gone through bench testing.

Finally, we have a goal of testing a digital servo loop on the PNI differential degree-of-freedom. This would use prototype hardware developed by CDS (see the LSC signal processing bench prototype section below). However this possibility is threatened by the time constraint on the PNI, due to its forced shutdown in early 1998 for the lab relocation.

8.3. Photodetector testing & prototype development

Several additional tests on the photodiodes are planned for the near future, and in parallel the design of the prototype detector assembly will be started.

Additional Device Tests:

- Photodiode backscattering. We intend to measure the backscattering from the 2 mm InGaAs photodiode in order to assess how we can make the design meet the backscattering requirement.
- High Power Transient behavior. The reponse of the diodes to high power transients will be tested. This requires acquiring a suitable high power laser source.
- Harmonic distortion and Non-linearity. Tests will be devised and performed to look at

non-linearities in the devices, possibly including applying a realistic AM waveform on the light (a model of the expected AM signal at the interferometer's anti-symmetric port).

In addition we will investigate the possibility of creating a suppressed carrier test setup in order to test the devices with a more realistic incident light power.

Prototype Detector Assembly:

- Opto-mechanical design of the housing and focusing & splitting optics
- Electronics design: preamplifier, bias source
- Assembly of PD assembly; establishing alignment procedure
- Testing; modifications for final design

8.4. LSC signal processing bench prototype

Digital control systems are not commonplace in the LIGO labs, and thus there is not a lot of experience with this technology as it applies to our control problems. We intend to conduct extensive prototype tests of the signal processing aspects of the LSC system in order to build up the final hardware and software design. This tests are broken up into three parts: a single channel, open loop setup; a single channel closed loop setup; and a multiple channel testing phase. Also as mentioned above, the single channel hardware and software may be implemented on the PNI if the schedule permits.

8.4.1. Single channel, open loop tests

The first suite of tests will focus on issues of noise, dynamic range and gaining experience with specific ADC, DAC, and CPU hardware & software. The setup for these tests is shown in Figure 41; it will be used to:

- measure ADC (quantization) noise as a function of the sampling frequency
- measure ADC noise as a function of clock jitter
- measure dynamic range limits
- measure DAC output noise
- measure other specs of the ADC & DAC
- investigate time delays & latencies in the ADC/DSP/DAC chain
- test the coding of the DSP for the desired transfer functions
- test writing to reflective memory

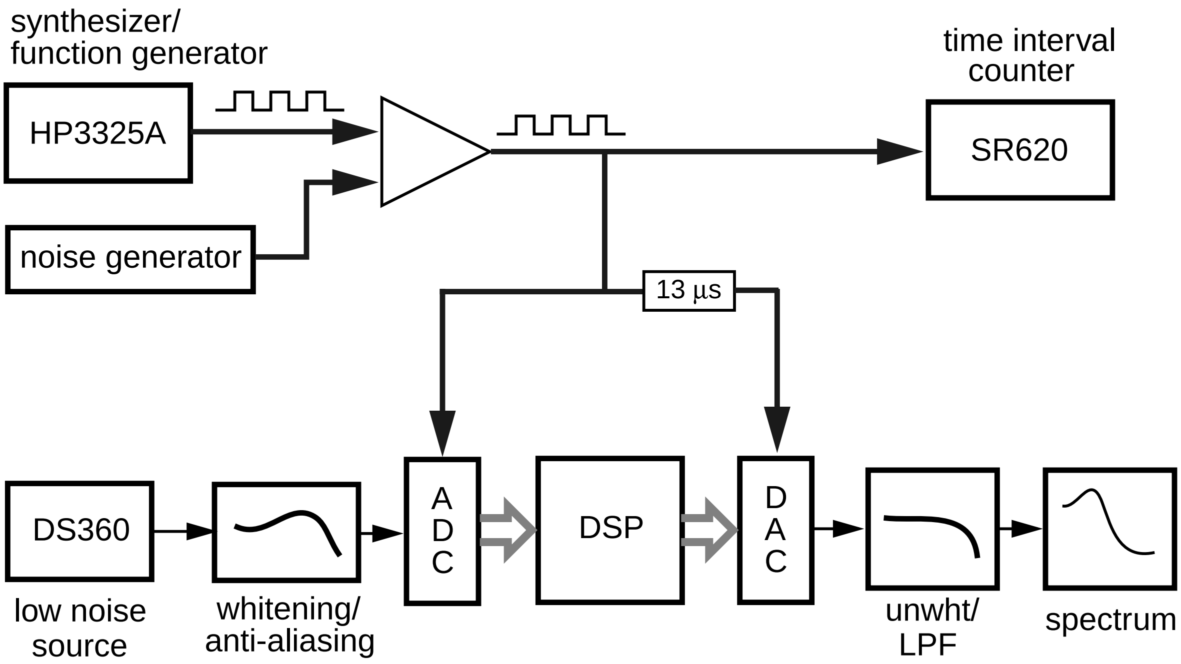

Figure 41: Setup for the initial phase of the LSC signal processing bench prototype. The noise generator is for adding clock jitter. The 13 µs delay in the DAC clock simulates the arm travel time delay.

8.4.2. Closed loop, single channel tests

The next phase will be to close a loop using the above processing hardware and software. The details of what will be included in the loop are yet to be worked out (such as whether to include a real or simulated pendulum; whether to include a real suspension driver; what the input excitation will be; whether to include a photodetector at the input). The goals of these tests are;

- verify stable operation of the loop
- perform diagnostic functions to exercise the diagnostic methods outlined in **Section 7-Diagnostics**
  - closed loop transfer functions
  - step response

8.4.3. Multiple channel tests

Another series of tests will focus on the implementation of all four signal channels of the LSC. The principal issues are the interfacing of the individual sensor channels via reflective memory, and the processing requirements and software development for implementing the complete control system.

These tests will follow the final selection of the ADCs and DACs. We expect to replicate the signal chain shown in Figure 41, and to include reflective memory modules and networking in the setup. An additional goal would be to implement a prototype of the ISC diagnostics network, as described in **Section 7.** This will most likely be an open-loop setup.

A. SUPPORTING CALCULATIONS

A.1. Baseline interferometer plant sensitivity matrix

Expressions for the response of the resonant interferometer to changes in length are derived in **LIGO-T970084-00-D.** The length sensitivity matrix L is defined such that

$$S_i(t, \delta l) = 2J_0(\Gamma)J_1(\Gamma)P_i\sum_j L_{ij}\delta l_j \cos(\Omega t + \phi_{ij}) \quad (1)$$

where S_i is the amplitude modulated signal on the i-th photodetector; δl_j is the deviation from resonance of the j-th degree of freedom; L_{ij} is the length sensitivity matrix; ϕ_{ij} is an intrinsic RF phase; P_i is the power on the i-th detector; and Ω and Γ are the RF modulation frequency and depth, respectively. The DC plant matrix, expressed in units of the laser wavelength, for the interferometer parameters listed in Table 1 is as follows.

Signal port	ϕ_{RF}	L_+	l_+	L_-	l_-
Reflection	I	–62000	–560	0	0
Recycling cavity	I	5200000	17000	0	0
Anti-symmetric	Q	0	0	23000	180
Reflection	Q	0	0	0	19
Recycling cavity	Q	160	0	0	4900

Table 15: Baseline DC plant matrix in units of wavelength.

A.2. Plant matrix variation over interferometer parameter ranges

The plant matrix can vary considerably as a function of the optical parameters of the interferometer, particularly mirror reflectivities and losses. The magnitudes of the error signals depend on the cavity build-up factors for the carrier and sidebands. The precise recycling mirror transmission for maximum carrier recycling gain, for example, will best be determined once the carrier losses in the arm cavities are well-known. The asymmetry for optimal GW sensitivity, will, in turn, depend on the recycling mirror transmission. Currently, the greatest uncertainty lies in the exact losses associated with each mirror surface. While the proposed interferometer sensing matrix is fairly insensitive to small perturbations in the interferometer configuration, the overall optimization can impact it by a factor of a few. To address the uncertainty in mirror losses, both in the mirror fabrication process and loss accumulation due to mirror contamination, we explore changes in the optical sensing plant over the anticipated range of mirror losses. In Table 16 we provide the DC plant for two potentially extreme cases where interferometer losses per mirror surface are 10 ppm and 100 ppm, respectively. It is sufficient to limit our study to the DC response of the interferometer since the expected deviation of the losses from their design value have negligible impact on the cavity storage times.

Signal port	ϕ_{RF}	L_+	l_+	L_-	l_-
Reflection	I	–110000 – 36000	–1100 – 230	0 0	0 0
Recycling cavity	I	9400000 300000	42000 5800	0 0	0 0
Anti-symmetric	Q	0 0	0 0	31000 17000	240 130
Reflection	Q	0 –2	0 0	0 0	61 –10
Recycling cavity	Q	344 70	0 0	0 0	6600 3700

Table 16: DC plant matrix for 10 ppm (upper numbers) and 100 ppm (lower number) loss per mirror surface. The interferometer is optimally configured for 50 ppm loss per surface.

The dependence of matrix elements on mirror losses is summarized in Table 17, where we list the fractional change in the non-zero elements of the plant matrix (relative to the baseline matrix) as a function of mirror losses. It must be noted that a negative fractional change represents a sign reversal in the sensor signal as the interferometer losses increase, a situation we avoid by judicious choice of sensing ports, as described in Section 2.1.3. Furthermore, we note that the sensor gains are within a factor of 2 or 3 of the design value for most sensors and a factor of 10 in the worst case (recycling cavity *I*-phase signal for l_+ detection). Gain changes at this level are easily accommodated in the servo electronics design.

Loss (ppm)	**SrefI/ L_+**	*SrefI/ l_+*	*SrecI/ L_+*	**SrecI/ l_+**	**SantiQ /L_-**	*SantiQ /l_-*	*SrefQ/ l_-*	**SrecQ/ l_-**
10	**1.8**	2.0	1.8	**2.5**	**1.3**	1.3	3.2	**1.3**
100	**0.6**	0.4	0.6	**0.3**	**0.7**	0.7	–0.5	**0.8**
200	**0.3**	–0.1	0.3	**0.1**	**0.5**	0.5	–2.1	**0.5**

Table 17: Fractional change in dominant elements of the DC plant matrix scaled to a baseline plant matrix optimized for 50 ppm loss per mirror surface. The primary detection signal for a given degree of freedom is highlighted.

B. PHOTODIODE CALCULATIONS, TESTS AND PRELIMINARY RESULTS

B.1. Photodetector Assembly Signal-to-Noise Calculations

The shot noise in the detected antisymmetric port photocurrent is required to be 10 times greater than the total electronic noise of the photodiode assembly, which includes both thermal (Johnson) noise and amplifier noise contributions. For an individual photodiode, coupled to an amplifier, we may write:

$$V_{SN} = Z_D\sqrt{2e(I_{DC}/N)}\sqrt{\frac{3+P_C/P_{SB}}{2+P_C/P_{SB}}} \geq 10V_{EL} \tag{2}$$

where

V_{SN} is the shot noise voltage equivalent in one PD

Z_D is the equivalent resistance of the individual PD circuit at resonance

e is the electron charge

I_{DC} is the **total** DC current in all the PD at a given light intensity

P_C is the carrier power

P_{SB} is the side band power. (For our calculations, $P_c/P_{SB} = 1/2$)

N is the number of channels (PD)

V_{EL} is the electrical noise of each channel. Its consists of the quadratic sum of the equivalent thermal noise of the PD impedance Z_D and the amplifier noise V_{AMP} (max 2mV):

$$V_{EL}^2 = \sqrt{4k_BTZ_D}^2 + (V_{AMP})^2 \tag{3}$$

where k_B is the Boltzman constant, T is the temperature in degree Kelvin. For tuned circuits, for a PD with R_D serial resistance and C_D equivalent capacity, at resonant angular frequency ω_0 (25MHz in our case), the equivalent impedance at the amplifier input is (see Section B.2.2., Figure 43):

$$Z_D = \frac{1}{R_D(\omega_0 C_D)^2} \tag{4}$$

As an example, the value for the 2mm Hamamatsu PD is 81Ω.

B.2. Device testing results and calculations

In the following sections we present the most significant results obtained mainly with our baseline candidate device, the 2mm Hamamatsu PD.

B.2.1. Optical Test Bench

Figure 42 presents the optical setup used for our PD evaluations. The laser is a Lightwave 126 laser, with maximum power of about 800mW.

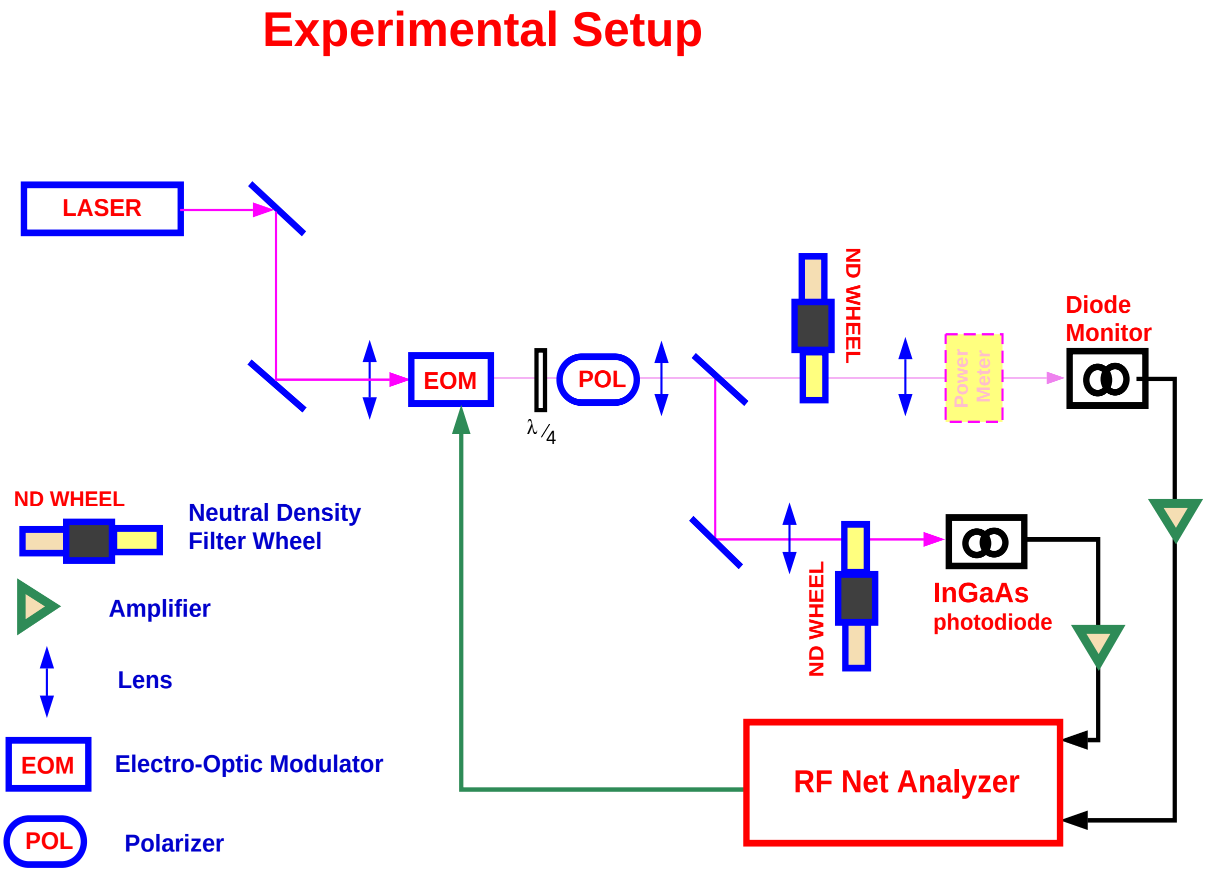

Figure 42: Experimental setup for PD evaluation

B.2.2. Photodetector selection

The quantum efficiency requirement narrowed the candidates for the LIGO PD to InGaAs diodes available only from few manufacturers. The relatively high power at the dark port necessitates the use of high power and high area PDs.All the InGaAs PDs have relatively high capacitance. In addition, our preliminary studies indicate that the increased light power levels lead to increased capacitance (which is in part due to temperature effects).

Figure 43 shows the equivalent electrical circuit of the PD.

The above requirements and considerations quickly narrowed the PD choices to the Hamamatsu InGaAs PDs. In this decision, we also took into consideration the VIRGO experience and tests made on various types of PDs. In Table 18 we present few typical characteristics of the Hamamatsu InGaAs PD as measured.

From the characteristics described here, the choices are dictated by the equivalent PD impedance, which count for the tuned amplifier design, and the PD area. In order to have reasonable power

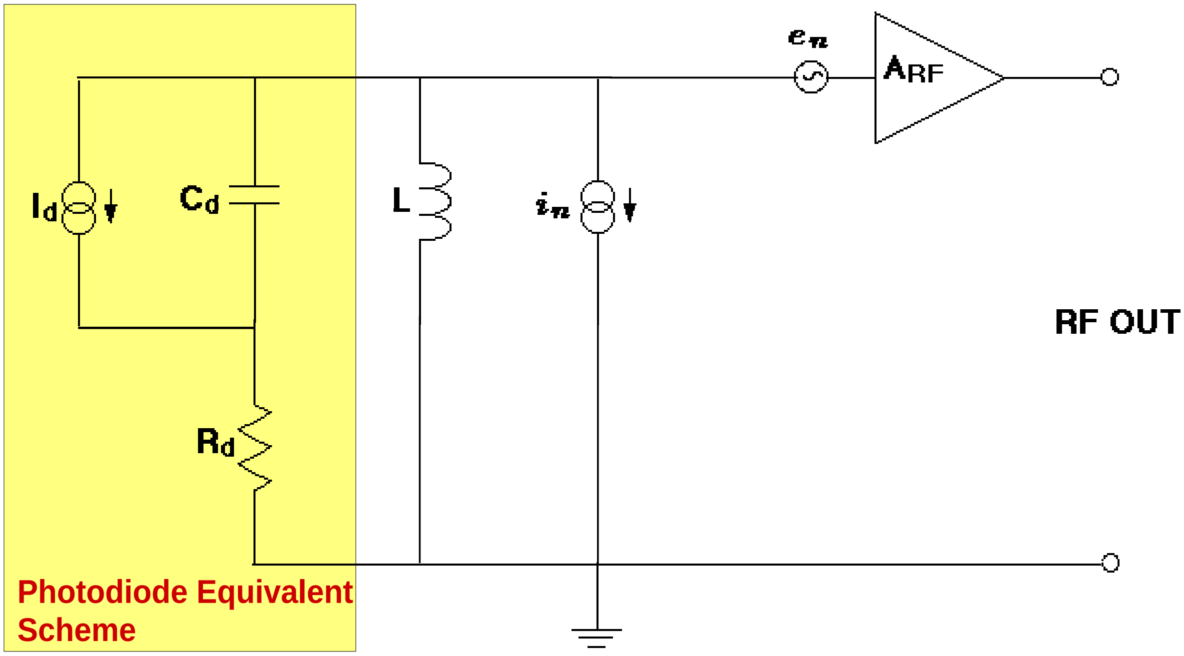

Figure 43: PD Equivalent RF Circuit. i_n and e_n are the amplifier equivalent current and voltage noise generators

Table 18: Standard Hamamatsu PD: Typical Capacitance and Serial Resistance at 10V reverse Bias Voltage

PD Diameter	*Capacitance (Cd)*	*Serial Resistance(Rd)*
G5832-1 (1mm)	68pF	12.8 ohm
G5832-2 (2mm)	250pF	8 ohm
G5832-3 (3mm)	500pF	8.8 ohm
G5114-3 (VIRGO 3mm)	330pF	12 ohm

density, the trend is to consider a larger area PD, but impedance considerations (tuned amplifier characteristics) are in favor of a small area PD. In addition, in the process of the choice of an optimum PD, all the following characteristics are important as well.

B.2.3. Hamamatsu Photodetector Spatial Uniformity

The G5832-2 (2mm) and G5832-3 (3mm) Hamamatsu photodiodes were tested for spatial uniformity. Using the test setup presented in Figure 42, the PD was moved along the beam axis to a point where the beam diameter was approximately $150\mu m$. The measurement were made in a 10 x 10 grid, equally spaced at 0.2mm. The results of these measurements for the 2mm Hamamatsu PD are presented in Figure 44. The two dips are believed to be due to some defects on the PD surfaces, and they are present both in DC and RF plots. Even with these defects, the uniformity of the 2mm Hamamatsu is better than 1.2%.

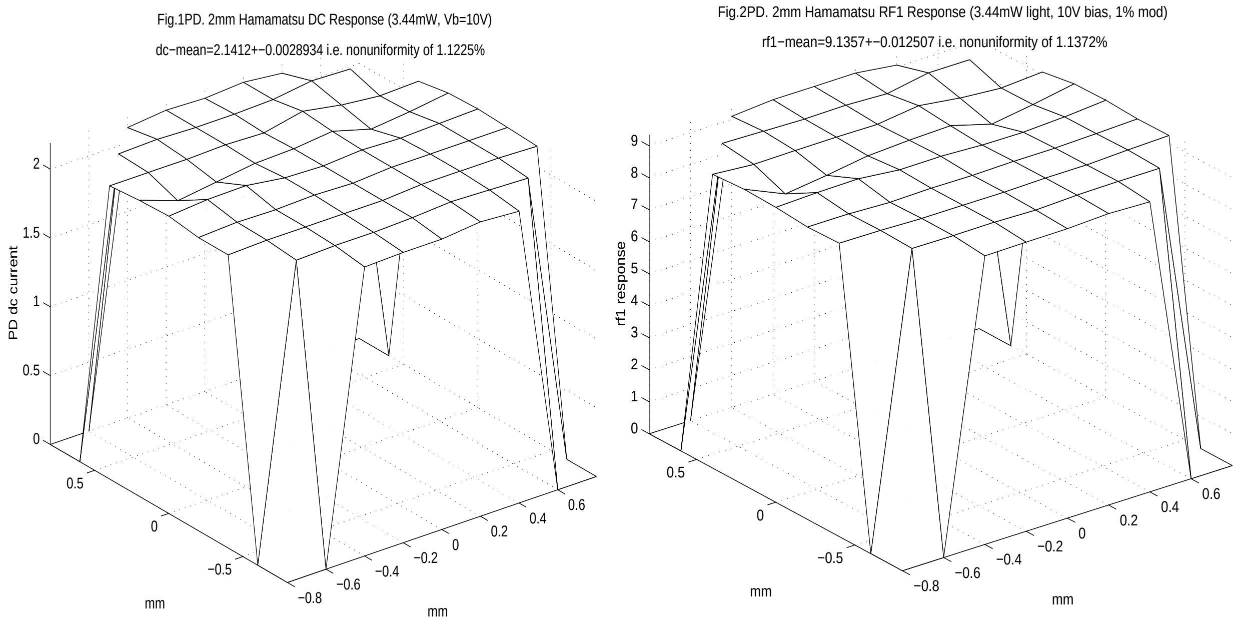

Figure 44: DC(left) and RF(right) spatial uniformity of the G5832-2 PD

The spatial uniformity measurements on the 3mm Hamamatsu PD, indicate an nonuniformity of about 3.2%.

At this point, the best candidate appears to be the 2mm Hamamatsu PD, so the following test procedures were concentrated on this particular product. Most of the following measurements were done using a beam of about 0.95mm diameter; exceptions are noted.

B.2.4. Reverse Bias Voltage

Many of the tests described were performed at various bias voltages. In order to keep the document at a reasonable size, we summarize the conclusions as follows:

- Higher bias voltage increases the linearity at high light power (saturation occurs at higher light level for higher bias voltages);
- PD Capacitance decreases with increasing bias voltage. Typically, the capacitance at 10V reverse bias voltage is half of the capacitance at 1V;
- The serial resistance is constant within 5% in the same bias voltage interval;

See Figure 45 and Figure 46 for examples of the bias voltage dependence of the PD response in DC and RF for 1% modulation depth (measured at the output of an amplifier with gain of 14.3).

B.2.5. Dependence on Modulation Depth

Amplitude modulation depth up to 10% was studied. The equivalent LIGO modulation depth at the main modulation frequency is equivalent to 0.1–0.2% amplitude modulation depth. The saturation of the PD response occurs at lower power levels for higher modulation depth. Significant results will be presented below.

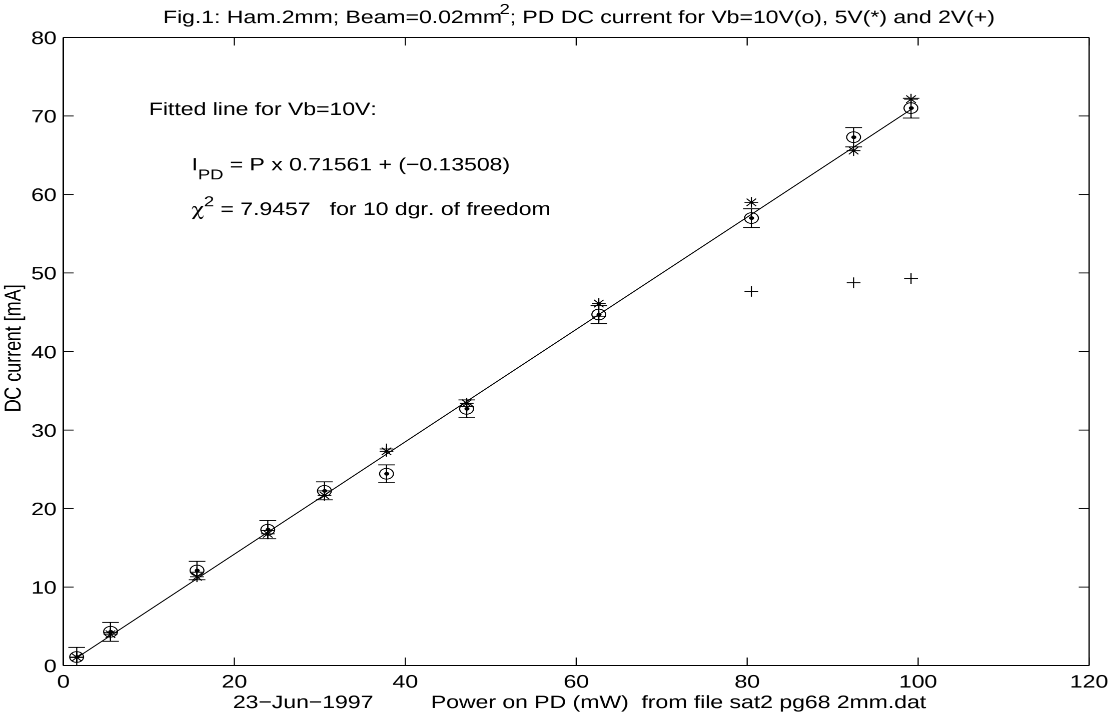

Figure 45: DC response of G5832-2 (2mm) at various bias Voltages

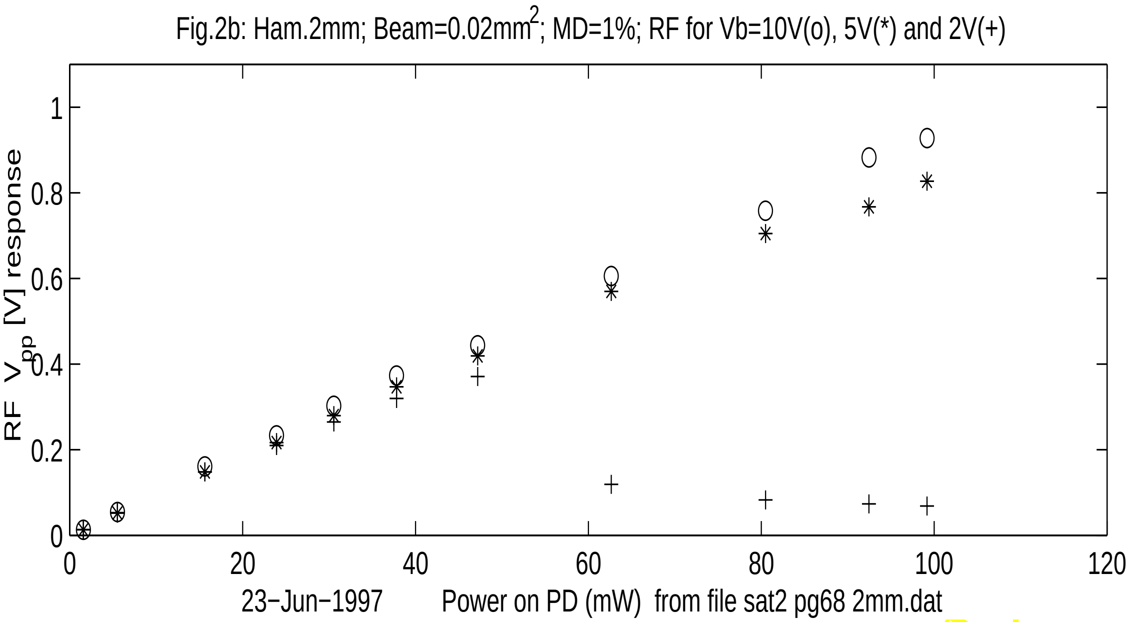

Figure 46: RF response of G5832-2 (2mm) at various bias Voltages

B.2.6. Temperature Dependence and its Effects on Detector Design

We have three experimental results pertaining to the temperature behavior of the 2mm Hamamatsu photodiodes. These are:

- Temperature variation of series resistance and capacitance with no light
- Variation of resistance and capacitance as a function of illumination (without cooling)
- The thermal resistance from junction to case

B.2.6.1 Temperature dependence of RF output

As mentioned earlier, the linearity of the photodetector output is one of the most critical parameters of our system. To illustrate the need to consider temperature effects, examine Figure 47, which shows the output of our tuned amplifier and the temperature of the diode heatsink, both as functions of time after the light was turned on. Since during this measurement we maintained constant bias voltage and illumination, we attribute the declining RF output to temperature effects. The third plot in Figure 47 shows that we have roughly 0.2% RF drop per degree Kelvin.

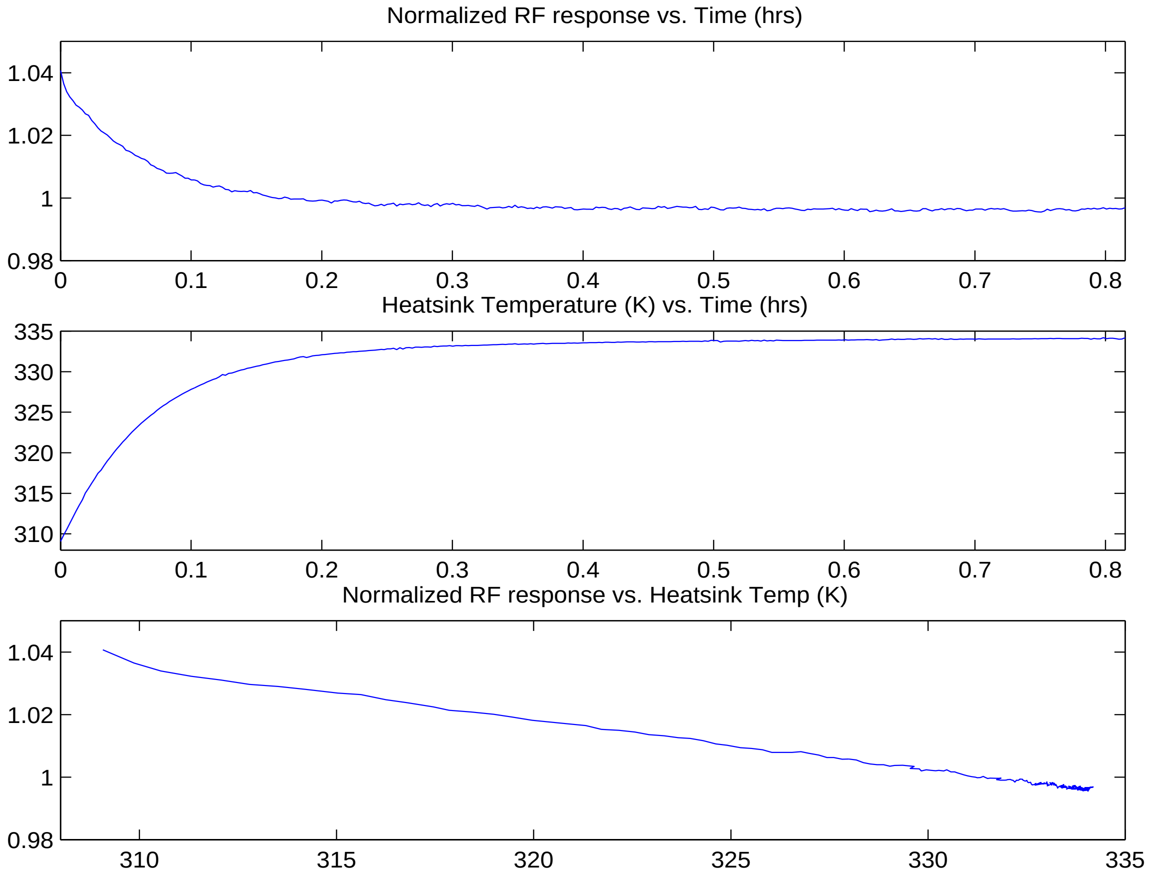

Figure 47: Decline in RF response, likely due to temperature increase. DC levels remained constant to within 0.5% (not

To investigate this effect, we measured the equivalent series resistance and capacitance of two of the diodes as functions of temperature (Figure 48). Variation in these parameters can change the Q and the center frequency of the tuned circuit — either of which could account for the RF output decline with temperature. The measurements were done by placing the diodes on a hot-plate and measuring their impedance with a network analyzer. We draw three conclusions from this result:

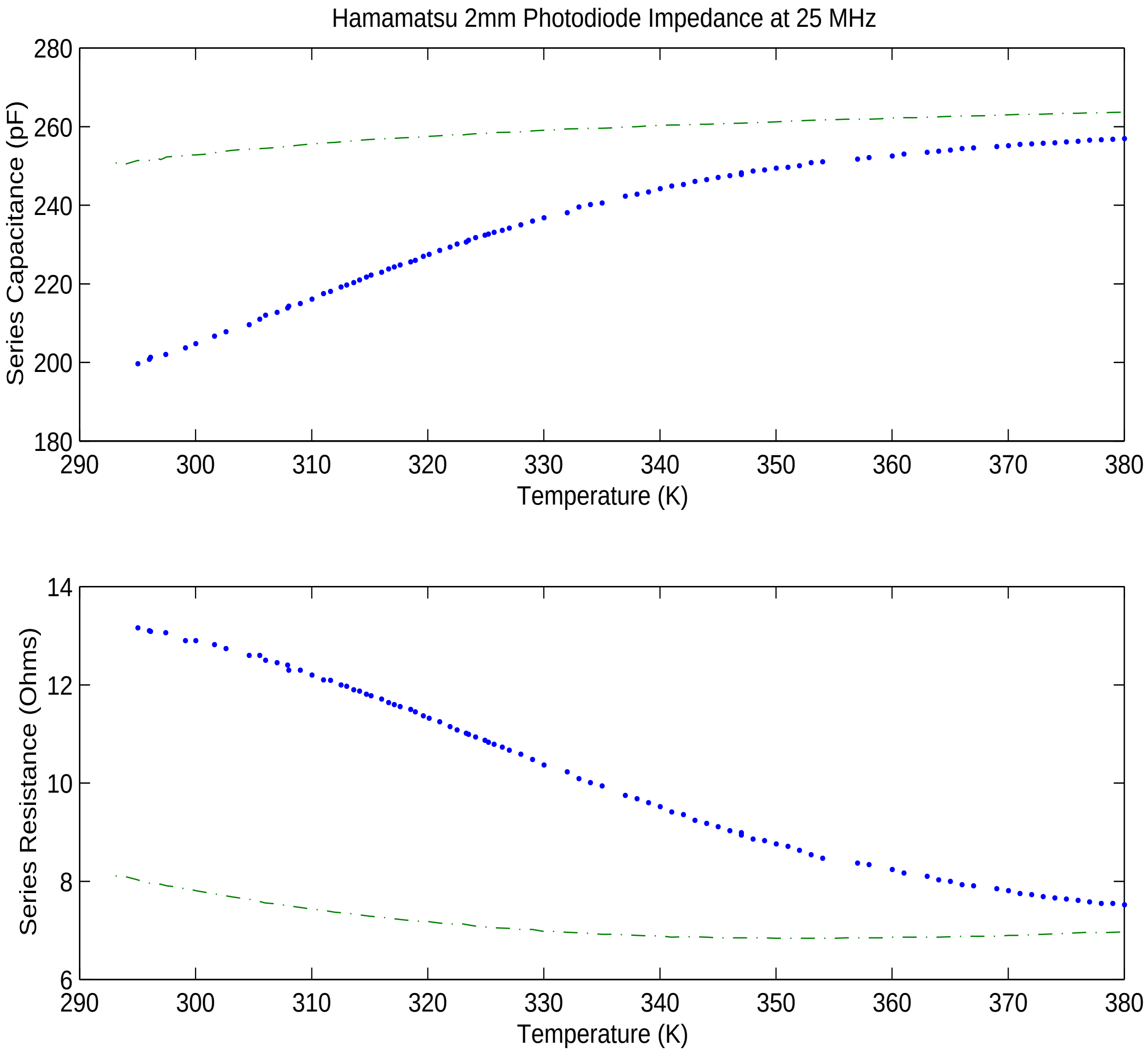

Figure 48: Impedance Measurements for 2 diodes without illumination.

- There is sample-to-sample variability in characteristics
- The high temperature values of the series resistance and capacitance for the different samples tend to converge, making the room temperature variability less important
- Temperature sensitivity of diode resistance and capacitance decreases at higher temperatures

B.2.6.2 Irradiation dependence of RF output

The above described temperature induced effects are overshadowed by the change in effective capacitance and resistance due to illumination. We first noticed this in frequency response tests of the tuned circuit and then direct network analyzer measurements of the diode. Figure 49 presents the results of the latter. Note that the plot includes thermal effects, since the diode was not cooled. Note also, that the rate of change of capacitance with light intensity or, equivalently, with photocurrent, decreases at high temperatures. The same cannot be said for the series resistance with the available data, but with the above mentioned frequency response analysis of the circuit (done by sweeping in frequency the RF modulation of the incident light) we were able to achieve much

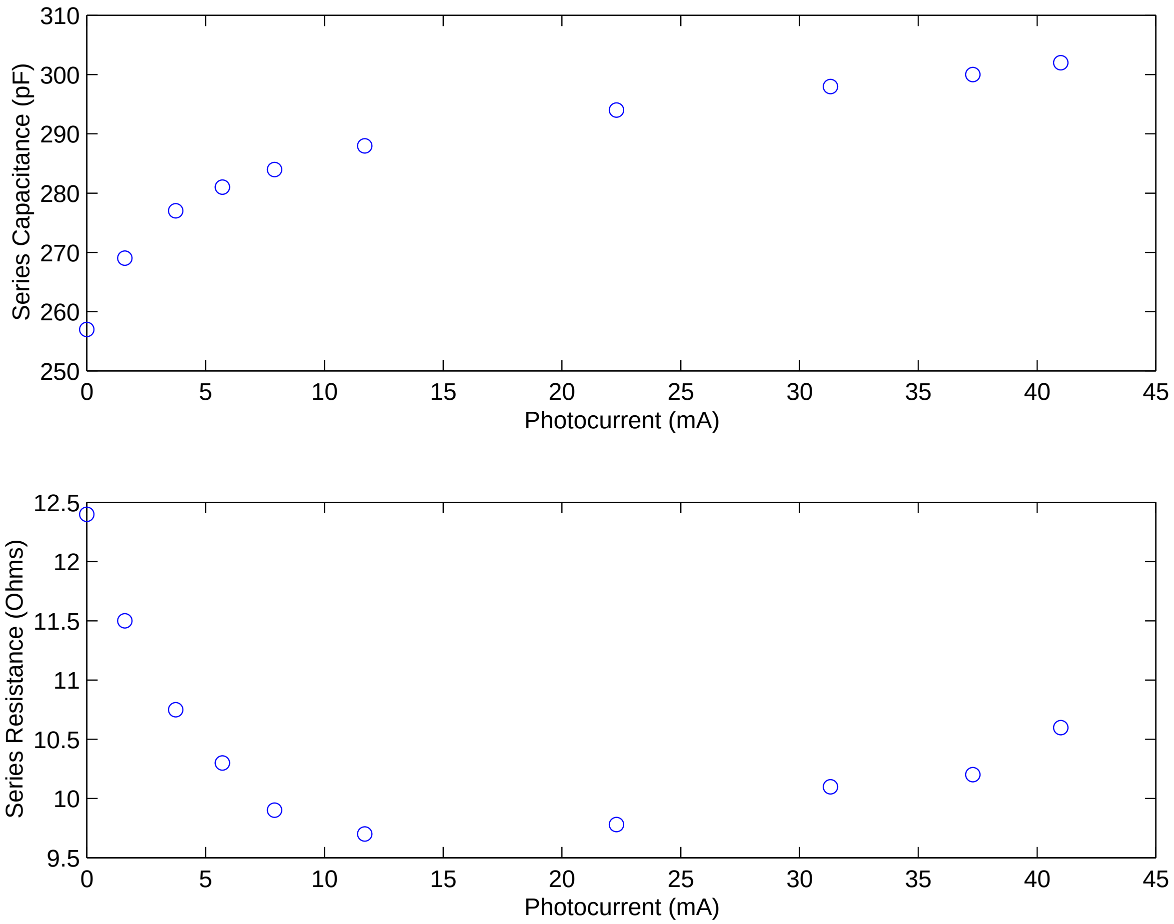

Figure 49: Variation of Diode Impedance with Light Level. (Data were taken after the diode reached maximum temperature.)

higher currents, and noted no apparent change in center frequency and circuit Q (with the current above some minimal value.) We therefore conclude that:

- Circuit parameters are fairly insensitive to light level as long as the photocurrent is above a few tens of mA. This condition is satisfied by the proposed current of 105mA

B.2.6.3 Implications

Under normal operating conditions, it should be a simple matter to keep the diode temperature constant to within one Kelvin, which requires only that the bias voltage, incident light, and heat-sink cooling be constant. This translates to robust circuit behavior and good linearity of response. There is likely to be a ‘ramp-up’ time for the output, probably shorter than shown in Figure 47 if we assuming good heatsinking. Temperature sensors could be used to provide ready status indication.

B.2.6.4 Thermal Resistance

To put to use the above information, we must have an idea of the operating temperature of the diode junction. Figure 50 represents the simplified thermal model we are working with. Power absorbed from the light and generated by electrical dissipation flows from the junction through the case into the air. Under steady-state conditions, temperatures will remain constant. Measurement of the thermal resistance from junction to case was done by measuring the forward voltage drop at a constant current as a function of temperature, and then exposing the diode, reverse biased, to the laser until a steady state is reached. The light was then turned off and forward bias quickly applied. Based on these measurements, we conclude that the thermal impedance is 20±1 K/W. This would necessitate running the diodes hot in spite of a heat sink, but current long-term measurements indicate that diode properties do not change with an electrical dissipation of 1.75W.

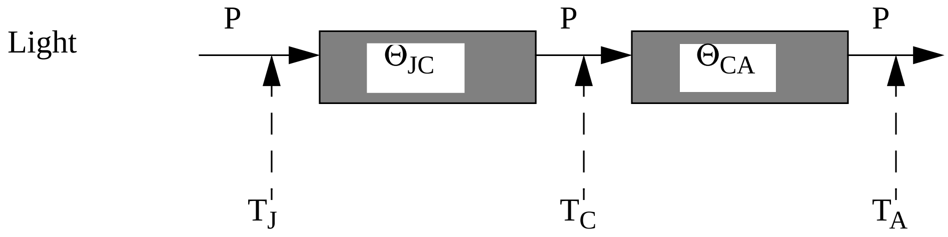

Figure 50: Thermal Model of the Photodiode. P is the power dissipated in the diode, Θ are thermal resistances, T are temperatures, and subscripts J,C,A refer to Junction, Case, and Air.

B.2.7. DC and RF 2mm PD Response at Various Power Levels

The RF response of the PDs to be used at the antisymmetric port is one of the most important parameter tested. The following response dependencies were measured and analyzed. The DC response was measured up to the maximum power available. Due to the high power dissipated into the PD, we suspect it is possible to damage the junction by overheating. During this test (with cooling), we observed that after the exposure at high power, the capacitance and serial resistance were unchanged while the dark current increased by a factor of more than 10.

Because of that, we concluded that a cooling system is necessary if the PD is to be run at high powers. The PD was mounted into a heat sink and cooled using a fan, so that the temperature of the case was kept within the factory specifications. Figure 51 presents the DC response of the HAM 2mm PD up to about 650mW of light power. *The DC response is linear up to about 450mW,* where sign of saturation occurs.

The fit of the same DC data are in Figure 52. as dashed line. This figure also presents both the DC response of another 2mm PD (circles) as well as the its RF response at 0.2% amplitude modulation depth, as measured at the output of an amplifier with gain of 14.3. Within the errors, *the RF response is linear till about 200mW*

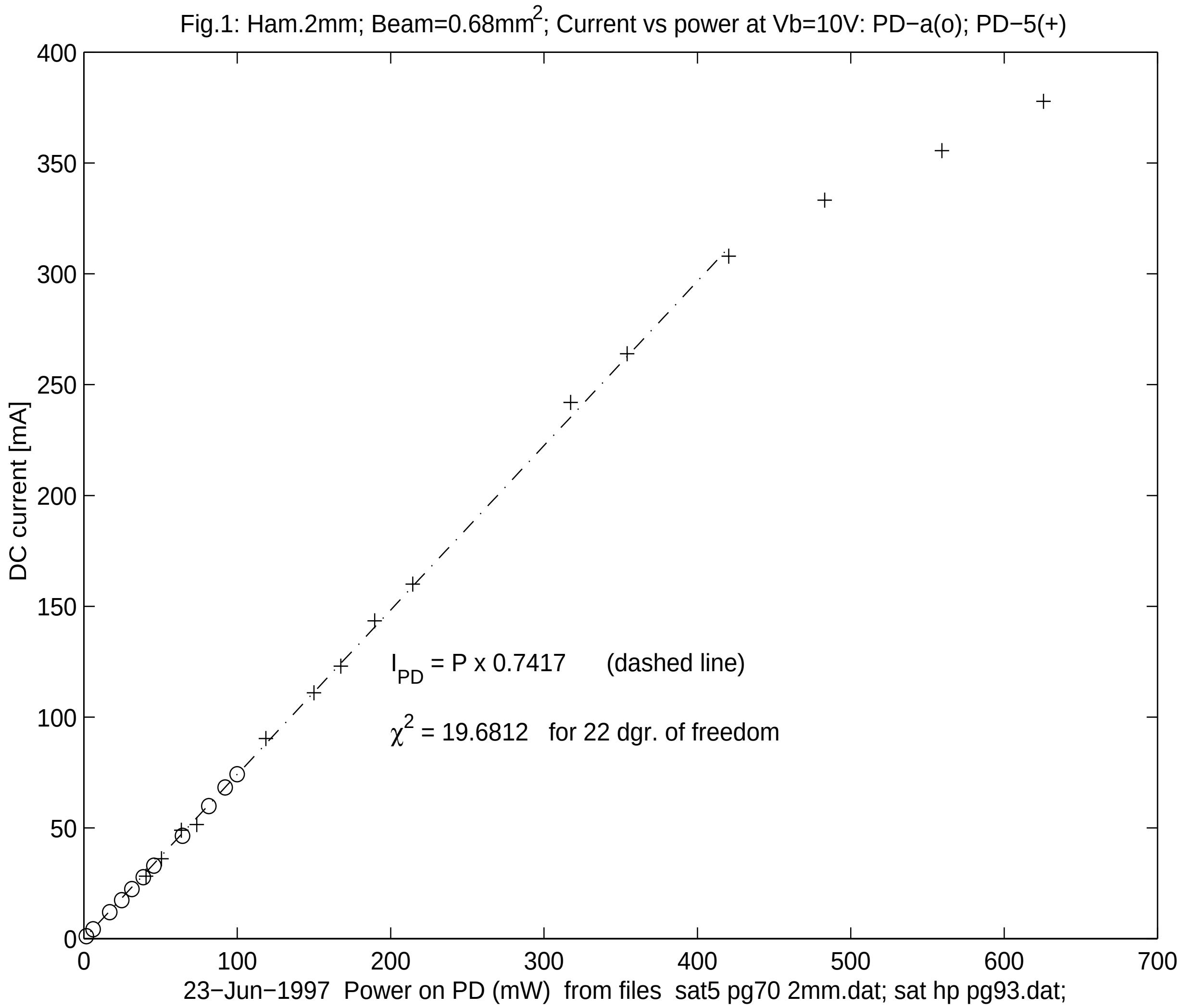

Figure 51: High Power DC Response of the G5832-2 (2mm) PD

B.2.8. Maximum Continuous Power Capability

Two long term exposures were made using the 2mm Hamamatsu PD. A 24 hour run at about 100mW did not show any signs of change in parameters and PD performances. A second long tern exposure at about 270mW of light power (the PD current is about 175mA at 10V bias voltage, which means we have approximately 2W of power dissipated in the PD) was made for a period of 14 days. The experiment is located into a place which does not have a good thermal control system. The PD was continuously cooled using the heat sink and a fan. The following conclusions were obtained:

- The dark current does not change,
- The DC current was constant within 1%
- The RF voltage changed by about 15% due to the temperature fluctuations, which are affecting both the optical characteristics of some of the components (mainly EOM and its mount) as well as the RF response of the PD (see above).

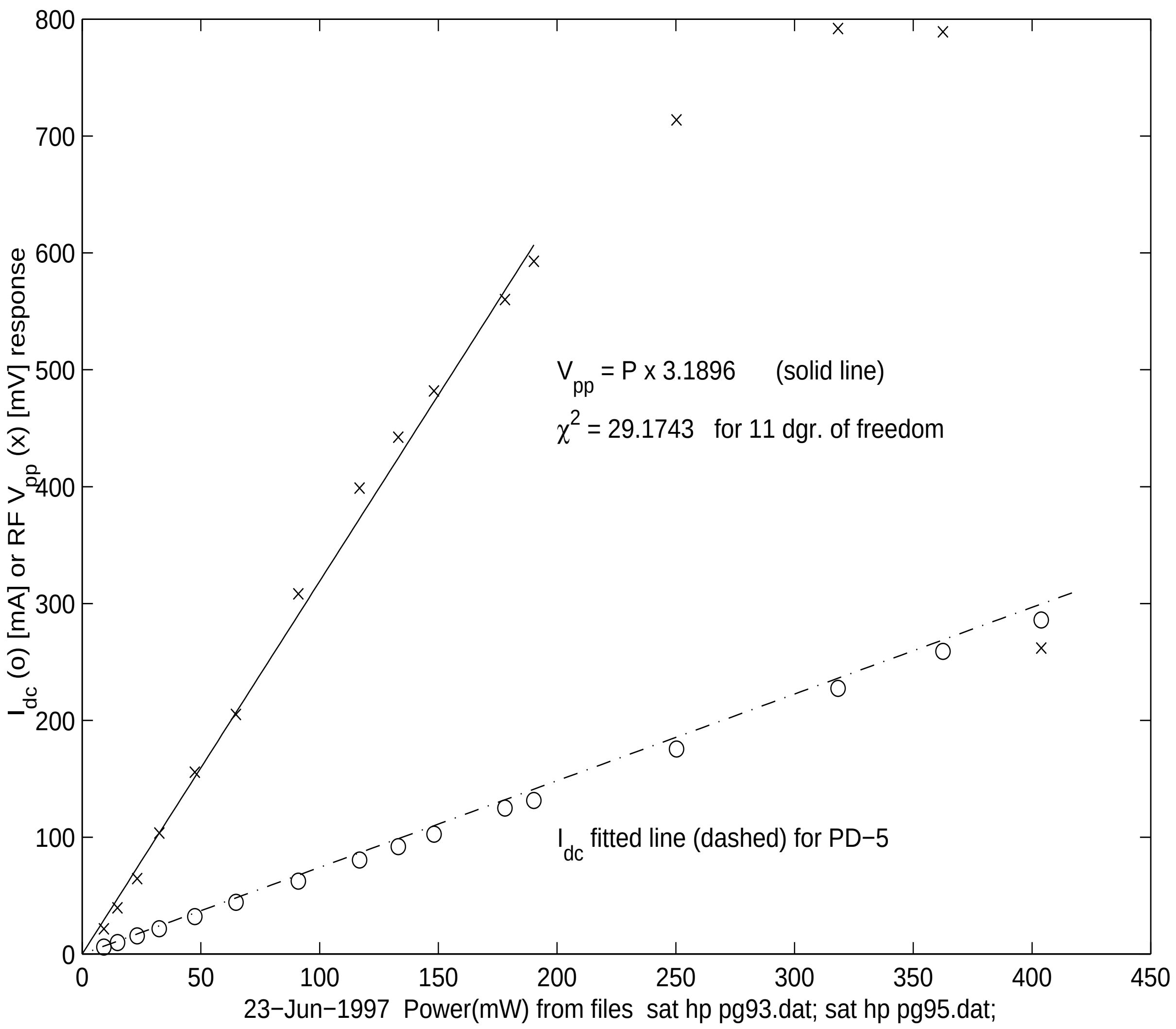

Figure 52: High Power Response of the G5832-2 (2mm) PD.The DC(o) and the RF(x) data are obtained with PD number “a”. The dashed line is the fit of DC data from Figure 51

The data presented in the previous paragraph, as well as the long term tests suggests that the *maximum continuous power acceptable is 200mW.*

As it was shown above, at this power level, *an efficient cooling is required*.

B.2.8.1 Transient Peak Power Capability

Preliminary tests made at the photodiode test bench show that the 2mm Hamamatsu PD may handle about 500mW of light power for short period of time (less than few seconds), even with the bias voltage on, without significant changes in its characteristics. Higher peak power, with bias voltage on, might affect the PD dark current.

B.2.8.2 Photodetector Quantum Efficiency, Reflections and Backscatter

- Photodetector (PD) Quantum Efficiency

The QE is defined as the ratio between the number of photoelectrons created divided by the number of incident photons. In terms of “radiant sensitivity” S (photoelectric current per incident radiant power at a given wavelength $\lambda[nm]$, in units of A/W), we may write:

$$QE = \frac{S \cdot 1240}{\lambda} \times 100\,\% \tag{5}$$

The radiant sensitivity is used also by manufacturers. The advertised S values are for the PD assembly, so values with/without windows are different. Our tests indicated a value of $S = 0.70 \pm 0.02$, in agreement with the factory specifications. We amy estimate that the QE for the windowless PD will be $QE = (82 \pm 2)\%$. Note that this values were calculated from data close to 200mW of light power.

- PD reflections

All the above measurements were performed using commercial PD with windows. Measurement of the reflections from the two window surfaces and the coated InGaAs crystal surface, indicate that approximately 8% of the total incident power is reflected by the window, while less than 1% is reflected by the coated crystal (at small angles). After removing windows, the reflected light from the PD coated surface was measured to be about 0.7% at small angles (below 15^o).

- Backscatter from Individual PD

From the manufacturer information, we know that the crystal surface does not have a special optical polish. Initial measurements done by Rai Weiss, indicate that the backscattering is less than $10^{-3}/(sterad)$. Further tests are necessary.

B.2.9. Optical Component Losses, Reflections and Backscatter

B.2.9.0.1 Losses and Reflections in Beam Splitters

Considering a simple model, in which both beamsplitter surfaces are coated, that they have the same loss due to interface relative reflection, Λ_R, while the relative bulk absorption in the beam splitter is Λ_A. It is trivial to show that the *reflected beam* will have a relative intensity of:

$$\Re = R \times (1 - \Lambda_R) \tag{6}$$

where R is the reflected coefficient of the beam splitter. In order to be exact, we will not use the transmission coefficient as advertised, but the real relative transmission, which is

$$\Upsilon = 1 - R(1 - \Lambda_R) - \Lambda_R - \Lambda_A \tag{7}$$

Those are the relations to be used in calculating the total optical losses and estimation of the maximum admissible reflected and absorbed losses.

B.2.9.0.2 Losses and Reflections in Lenses

The calculation is very similar, taking in account that the only reflected light is Λ_R, while the relative transmitted light is

$$1 - 2\Lambda_R - \Lambda_A \tag{8}$$

B.2.9.0.3 Backscatter from Optical Components

We will assume that the optical components will be of best optical quality, so that the total backscatter light from all the optical components will be negligible.

B.2.9.0.4 Total OPtical Loss for the Proposed PD Assembly

As an exercise, for the PhotoDetector Assembly, as presented in Figure 6, the total relative optical transmission, which includes PDs, beamsplitters and input collimator, is

$$(1 - 2\Lambda_R - \Lambda_A)^4 \tag{9}$$

B.2.10. PD to PD response variation.

Using a very limited sample of 2mm Hamamatsu PDs, we have been able to conclude that the capacitance and resistance values have about 20% variance. For the final design, we will require a minimal spread in capacitance, in order to better match the frequency tuning of the amplifier. For the future orders, the nominal capacitance should be less than 250pF and the resistance of about maximum 8 ohm at room temperature and at 10V bias voltage. A 10% spread limit will be imposed. Further requirements will be established for the nominal values at the working power and temperature. Preliminary, we may require a maximum capacitance of 270pF and 8 ohm serial resistance at 45 degree C. TBD.

C. OPTICAL POWER TRANSIENTS ON LOSS OF LOCK

During locking and unlocking transient events, the expected maximum power level on the gravity wave photodetector is not known. Simulations were run using SMAC in order to get an order of magnitude estimate on what this level might be. After some discussion within the ISC group, it was decided to model the worst case event as the interferometer unlocking due to an impulse in velocity on the beamsplitter. Fig. 53 shows how the carrier intensity changes in the cavities and on the photodetector due to an impulse in velocity of 10 microns/sec on the beamsplitter (simulations assumed 1 watt of input power so the power levels need to be multiplied by 6 to get the levels expected for LIGO). This transient model seems a plausible upper limit, since the average rms velocity during a noisy time at the LA site is around 2 microns/sec while the average at the WA site is around 0.5 microns/sec. The simulation predicted a maximum instantaneous power of 84 watts incident on the gravity wave photodetector.

Figure 53: Power levels (assuming 1 W input) when interferometer unlocks due to an impulse in velocity of 10 microns/sec on the beamsplitter.

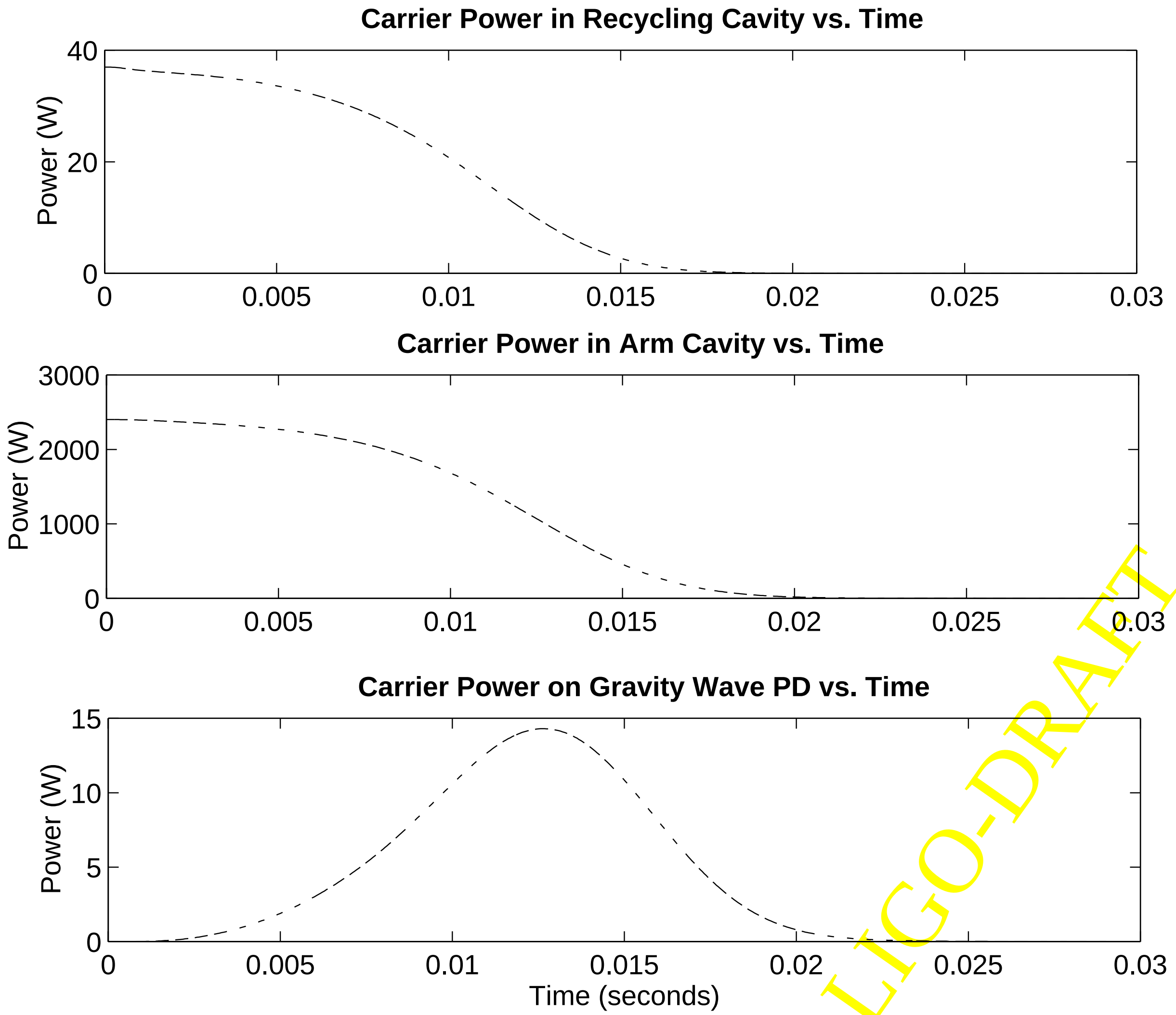

Carrier Power in Recycling Cavity vs. Time

Carrier Power in Arm Cavity vs. Time

Carrier Power on Gravity Wave PD vs. Time

Fig. 54 shows the results of a more conservative model; the transient unlocking event is modeled as an impulse in velocity of 50 microns/sec driving the beamsplitter. The maximum power level on the gravity wave detector for this model is 270 watts. The values plotted in Fig. 53 and Fig. 54 are dependent on controller design, optical parameters, and, most importantly, the model of the disturbing transient. For this reason the data presented here should be viewed only as a first step in the process of determining a requirement on the power handling capability of the gravity wave photodetector.

Figure 54: Power levels when interferometer unlocks due to an imulse in velocity=50 microns/sec on the beamsplitter.

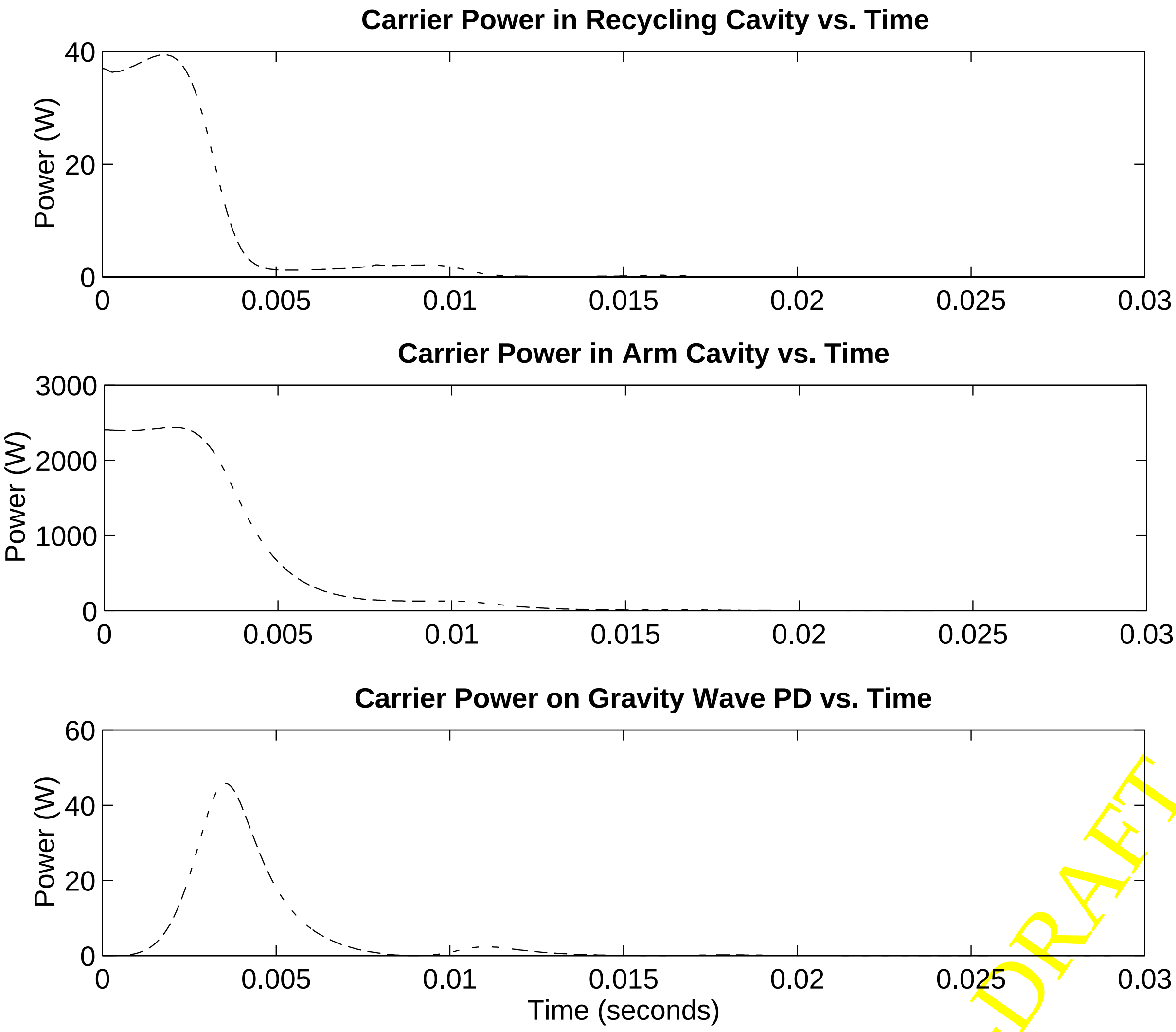

D. REFERENCED DOCUMENTS

D.1. LIGO documents

[1] LIGO-E950018-00-E, *LIGO Science Requirements Document*

[2] LIGO-T960057-00-I, *ISC Inter-Station Signal Transmission*

[3] LIGO-T950065-00-D, *Detector Systems DRD*

[4] LIGO-T960058-00-I, *LSC Design Requirements Document*

[5] LIGO-T960019-00-D, *Frequency, Intensity and Oscillator Noise in the LIGO*

[6] LIGO-T960042-00-D, *Shot noise in the Length Error Signals*

[7] LIGO-T950030-03-D**,** *Prestabilized Laser DRD (B DCC)*

[8] LIGO-E950099-01-D, *Core Optics Components DRD*

[9] LIGO-P940002-00-I, *Ph. D. Dissertation, M. Regehr*

[10] LIGO-T960071, *40-Meter Reference Source System Specification*

[11] LIGO-T950011-06-D, *Suspension DRD*

[12] LIGO-T952109-01-I, *LIGO Length Sensing System: Design Considerations.*

[13] LIGO-T960010-00-D, *(DAQ design document)*

[14] LIGO-T960031-00-E, *CDS Online Diagnostic and Readout Functions*

[15] LIGO-T960057-00-I, *ISC Inter-Station Signal Transmission*

[16] LIGO-T960032-03-I, *Concept for LSC Design During Detection Mode*

[17] LIGO-T960122-00-D, *Proposed Initial Detector MC and RC Baseline Lengths*

[18] LIGO-T970068-00-D, *Recycling Cavity and Mode Cleaner Cavity Baseline Dimensions*

[19] LIGO-L960019-00-F, *(memo on local seismic correlations)*

[20] LIGO-T960038-00-I, *LSC Photodetector Development*

[21] LIGO-T970060-00-D, *Alignment Sensing/Control Preliminary Design*

[22] LIGO-T952007-00-I, *ASC Design Requirements Document*

[23] LIGO-P95xxx-xx-x, *Guided lock acquisition in a suspended Fabry-Perot cavity*

[24] LIGO-T970084-00-D, *Frequency response of the LIGO interferometer*

[25] LIGO-T960112-05-D, *Detector Subsystems Requirements.*

[26] LIGO-T950072-00-R, *Evaluation of proposed changes to the suspension sensor electronics.*

[27] LIGO-T970088-00-D, *Frequency stabilization: Servo configuration and subsystem interface specification*

[28] LIGO-T960085-00-D, *LSC Configuration Issues*

[29] LIGO-T960065-00-D, *Seismic Isolation Design Requirements Document,* section 2.5.5.

[30] LIGO-T960103-00-D, *ASC: Environmental Input to Alignment Noise.*

[31] LIGO-T970071-01-D, *Core Optics Support Design Requirements*

[32] LIGO-P9xxxx-xx-I, *Alignment Issues in Laser Interferometric Gravitational-Wave Detectors (Ph.D. dissertation, N. Mavalvala)*

[33] LIGO-T960065-02-D, *Seismic Isolation Design Requirements Document.*

[34] LIGO-T960728-00-D, *Requirements of the LOS suspension Driver*

[35] LIGO-T970139-00-D, *LSC CDS Conceptual Design*

D.2. Non-LIGO documents

[36] *VIRGO Final Design v. 0.* The VIRGO Collaboration (6/95)

[37] *Diodes selection, the first approach.* VIRGO internal report PJT94-014, by A. Dominjon and M. Yvert (5/94).

[38] *Photodiodes selection for the VIRGO detector the first step*. B. Caron, A. Dominjon, R. Flaminio, R. Hermel, J.C. Lacotte, F. Marion, L. Massonet, R. Morand, B. Mours, D. Verkindt, M. Yvert, **Nucl. Inst. Meth. Phys. Res. A 360** 379 (1995).

[39] *Detection diodes, the second step*. VIRGO internal report NTS95-009, by A. Dominjon, R. Hermel, J.C. Lacotte, L. Massonnet, and M. Yvert (3/95).

[40] Ultrahigh-frequency stabilization of a diode-pumped Nd:YAG laser with a high-power-acceptance photodetector. N. Uehara and K. Ueda, **Opt. Lett. 19** (10), p. 728 (1994).

[41] *1995 Emitters and Detectors catalog*. EG&G Optoelectronics Canada (1995).

[42] *InGaAs-PIN Photodiodes*. Data sheet # KIRD 1002E03, Hamamatsu Corporation (1993).

[43] Drawing **V049-5-001,** *Equipment Arrangement Plan, Corner Station Washington, LIGO Vacuum Equipment.* Process Systems International.